Extraction of the top quark mass from the total top quark pair production cross section in the single lepton channel

D I S S E R T A T I O N

zur Erlangung des akademischen Grades

Dr. rer. nat.
im Fach Physik

eingereicht an der
Mathematisch-Naturwissenschaftlichen Fakultät I
der Humboldt-Universität zu Berlin

von
Valentina Ferrara

Präsident der der Humboldt-Universität zu Berlin:
Prof. Dr. Jan-Hendrik Olbertz

Dekan der Mathematisch-Naturwissenschaftlichen Fakultät I:
Prof. Stefan Hecht, Ph.D.

Gutachter:
1. Prof. Dr. Ulrich Husemann
2. Prof. Dr. Hermann Kolanoski
3. Prof. Dr. Wolfang Lohmann

eingereicht am: 16.08.2012
Tag der mündlichen Prüfung: 19.12.2012

Abstract

A measurement of the total $t\bar{t}$ production cross section in the single lepton channel is presented. The cross section is extracted in a profile likelihood fit of templates constructed from a likelihood classifier using four kinematic variables. For a top quark of mass $m_t = 172.5$ GeV, the measured cross section is 178.9 ± 12 pb. The measurement agrees within one-standard deviation with the latest theoretical predictions. The cross section measurement is repeated for seven other values of the top quark mass ranging from 140 GeV to 200 GeV to obtain the mass dependence of the experimental cross section. By comparing this with the mass dependence of different higher-order predictions, the top quark mass is extracted. This method allows the determination of two different theoretical mass parameters: the top quark mass in the on-shell scheme m_t^{pole} and in the $\overline{MS}$ scheme $\overline{m}_t(\overline{m}_t)$. The most precise measurement obtained is $m_t^{\text{pole}} = 171.2 \pm 4.5$ GeV, obtained when employing the most precise higher-order calculations in the $\overline{MS}$ scheme. This value agrees within one-standard deviation with the latest Tevatron average of the best top quark mass measurements.

Contents

Introduction

At the time of writing this thesis, the ATLAS and the CMS collaborations have announced the discovery of a new particle in the mass region around 126 GeV observed in the proton-proton collisions collected by the experiments in 2011 and 2012 at the center-of-mass energy of 7 TeV and 8 TeV respectively [60]. The result is still preliminary but the current analyses can already establish the consistency of the observation with the Higgs boson, the only particle predicted by the Standard Model not yet observed. After the Large Hadron Collider provides the experiments with more data, the true nature of this new particle will emerge. Whether this really is the Standard Model Higgs boson or one of its more exotic versions, this remains the discovery of the heaviest boson ever found and confirms that the top quark is the heaviest elementary particle in nature known to date.

The history of the top quark starts 20 years before its discovery, when Martin Perl and his team at SLAC found the first evidence of the τ lepton [144], the heavier sibling of the electron and the muon, which established the presence of a third generation of matter. Only two years after, at the Fermilab laboratory near Chicago, a group of physicists led by Leon Lederman discovered the bottom quark in the bottom-antibottom bound state, the Upsilon meson [100]. The Upsilon was found to be about three times as massive as the charm-anticharm meson J/ψ and thus the bottom quark had started the third generation of mass for the quark sector of the Standard Model.

At the beginning of the 1980s it was clear that the electroweak interactions grouped the elementary particles in pairs but the bottom quark was left in isolation. Another 15 years were to pass before the discovery of its electroweak partner, the top quark, in 1995, once more at Fermilab. The reason for this long wait lies in its immense mass: Standard Model fits to electroweak precision data were pointing at a mass greater than an entire atom of gold.

At hadron colliders such as the Tevatron and the Large Hadron Collider, top quarks and antiquarks materialize mostly in pairs. Currently the production rate is predicted by high-order calculations with a precision of about 12%. The experimental measurement of the production cross section of top-quark pairs provides us with a further stringent test of the predictive power and self-consistency of the Standard Model. It is also predicted by the theory that the top quark decays in less than 10^{-24} seconds in a bottom quark via the charged electroweak current. The difference in mass between the top and the bottom quarks is so huge that a real W boson is produced in the decay chains $t \to bW^+$ and $\bar{t} \to \bar{b}W^-$. At the Large Hadron Collider top quark pairs are produced copiously and since their experimental signature is a background for many models which involve new physics, the precise measurement of their production cross section is also important to reduce the uncertainty of new physics searches.

There is at least another reason why the top pair production cross section is a very interesting topic of investigation. Quarks carry color charge and are subject to color confinement: this implies that colored particles bind tightly together into colorless states and do not exist as isolated particles. The consequence of confinement is that we cannot measure the mass of a colored particle directly. So what is the mass of a quark after all? And how can we define it? The concept of quark mass is in fact ambiguous. When many authors realized that the first definition of quark mass employed by theorists was ill-defined, many more mass parameters were introduced, each representing the most advantageous candidate for the characteristic scale of the process considered. Once a particular definition is chosen and used consistently in the calculations, no ambiguity remains and different mass parameters can be converted into one another for numerical comparison. The only known method to extract from experiment a well-defined quark mass parameter is to compare predictions, expressed in the theoretical framework of interest, and observations that depend on the value of the quark mass. The production cross section is the most popular example.
This work presents the measurement of the top-antitop total production cross section and the extraction of two theoretical mass parameters for the top quark. The analysis is based on the proton-proton collisions at a center-of-mass energy of 7 TeV collected by the ATLAS experiment in the first half of 2011. This thesis is organized as follows: Chapter 1 gives an overview on top quark physics, Chapter 2 describes the experimental setup and the reconstruction of the relevant physics objects, Chapter 3 illustrates how the Monte Carlo samples on which the analysis is based are generated, Chapter 4 presents the description of the signal and of the kinematical cuts applied to select the signal as well as the five sources of background considered, Chapter 5 finally describes in detail the measurement of the total production cross section of top-antitop pairs and Chapter 6 develops on the concept of quark mass and presents the extraction of two top quark mass parameters.

1 Introduction to the physics of the top quark

This chapter is an overview of the physics related to the top quark. The first section introduces the basic notions of the very successful model that describes almost all particle physics phenomena observed to date. The second section develops on the top quark, its production mechanisms at hadron colliders and the phenomenology of its decays. The last section of this chapter describes the role assigned to the top quark in some extended models that introduce new physics.

1.1 A brief introduction to the Standard Model

It is a well known fact that the wave function describing two identical particles must be either symmetric or antisymmetric under interchange of the particles. Experiment tells us that all the particles of half integral spin are described by antisymmetric wave functions since the Pauli exclusion principle applies. Such particles are known as *fermions* because they obey *Fermi-Dirac statistics*. By contrast, the Pauli principle does not limit the number of identical particles of integral spin which may enter a given state. This distribution is given by *Einstein-Bose statistics* and the particles obeying it are known collectively as *bosons*.
The Standard Model (SM), the very successful theoretical framework that describes the constituents of matter and their interactions, further subdivides the particles according to the types of interaction in which they participate. The three, out of four, fundamental interactions embedded in the SM [1] are mediated by spin 1 gauge bosons: eight massless gluons (g) mediate the strong force while the massless photon (γ) and the two massive $W^{\pm}$ and Z bosons are the carriers of the electromagnetic and weak force respectively.
The interactions are introduced by requiring invariance of the SM Lagrangian under the gauge group $\mathrm{SU(3)_{QCD}}\times\mathrm{SU(2)_L}\times\mathrm{U(1)_Y}$. The $\mathrm{SU(3)_{QCD}}$ group describes the strong force while the electromagnetic and the weak interactions are unified under the $\mathrm{SU(2)_L}\times\mathrm{U(1)_Y}$ group [96, 162, 149]. The subscript L indicates that only the left-handed fermions are "charged" under the SU(2) weak isospin gauge group. The fermions can thus be naturally grouped into right-handed components that are singlets under $\mathrm{SU(2)_L}$ and the left-handed components that transform like doublets. The hyper-charge Y is defined via the

[1] Attempts are being made to incorporate the fourth force, gravity, into the scheme of unification. As an example, the theory called Supergravity embraces the Einstein gravitational field equations together with the SM strong and electroweak field equations. However, gravitational effects must be taken into account when the energy is of the order of the Planck mass $M_{\mathrm{Planck}} \approx 10^{19}$ GeV and therefore it can safely be neglected in most considerations concerning elementary particles.

weak isospin charge T_3 and the electric charge Q as $Y = 2Q - T_3$.
A remarkable feature of the forces is that their relative strengths are not constant. At high momentum transfer, the screening of the electron charge due to vacuum polarization diminishes resulting in a larger effective charge. The opposite is true for the other two forces: the anti-screening effect due to gluon and weak boson self-coupling gives rise to a phenomenon called asymptotic freedom in which, in contrast to the electromagnetic case, the charges of the strong and weak interactions decrease as they are probed to shorter and shorter distances. In particular, this allows for a perturbative treatment of the strong interaction at high momentum transfers [98, 145].
Elementary particles that do not respond to the strong force are known as *leptons*. Among these are also the neutrinos, which are electrically neutral and are not subject to electromagnetism. All leptons have intrinsic spin $\frac{1}{2}$ and are therefore fermions. Those particles which can participate in the strong interactions are known as *hadrons*. Unlike the leptons, the hadron family contains both fermions and bosons: the hadrons with half-integer spin are known as *baryons* whereas the *mesons* are bosons. Up to the present energy limit experimentally accessible, which leads to a resolution of approximately 10^{-18} m, the leptons appear to be structureless. They are therefore regarded as fundamental particles. The hadrons, on the other hand, are composite objects made up of spin $\frac{1}{2}$ fermions called *quarks* [165, 95]. The baryons are bound states of three quarks whereas the mesons are made up of a quark-antiquark pair [94, 141]. The most significant property of the quarks is that, being the only fermions responding to the strong force, they possess an additional quantum number, the color charge.
There appear to be in total 12 fundamental fermions, six quarks and six leptons. The three generations of increasing mass in which the fundamental fermions can be arranged are shown in Table 1.1. For the left-handed components, each generation is a weak-isospin doublet in which the members can be transformed into its partner via the charged-current weak interaction. In addition, to each one of these particles there exists an antiparticle, a particle sharing opposite electric charge and magnetic moment but otherwise identical.
Even though experimental measurements indicate otherwise, the SM describes massless particles. The presence of mass terms in the SM Lagrangian would in fact violate the gauge invariance of the theory. The mechanism of Spontaneous Symmetry Breaking (SSB) is then introduced to generate in an elegant way the masses of the $W^{\pm}$ and the Z gauge bosons while retaining the gauge invariance of the Lagrangian [101, 83, 99]. In the SM, the SSB is applied to the $SU(2)_L \times U(1)_Y$ electroweak (EW) group to break the electroweak theory and thus reducing it to a $U(1)_{em}$ symmetry. In doing so, a new field, the *Higgs field*, is introduced in the Lagrangian. To finalise the theory, the fermion masses, which are forbidden explicitly, are introduced via gauge invariant interaction terms, called *Yukawa terms*, between the fermions and the Higgs fields. The charged leptons and the quarks couple to the Higgs boson with a strength proportional to their mass. Unfortunately the Higgs boson mass depends on unknown parameters and cannot be predicted by the theory. In December 2011 direct searches from the ATLAS and CMS collaborations restricted its mass range between 115 GeV and 130 GeV [158, 159]. Just a few weeks ago, the observation of a new boson with a mass of 125 GeV has been

Type	Flavor			Q/|e|
leptons	ν_e	ν_μ	ν_τ	0
	e	μ	τ	-1
quarks	u	c	t	$+\frac{2}{3}$
	d	s	b	$-\frac{1}{3}$

Table 1.1: The three generations of fundamental fermions. The left-handed components are arranged in weak isospin doublets.

announced. The particle is consistent with the SM Higgs boson but further studies of its properties are needed before it is possible to claim that it really is it. The publications are still in preparation.
The final piece of the SM that is relevant to top quark physics is related to the mismatch of quark mass and electroweak eigenstates. The quark mass states are not eigenstates of the charged-current weak interaction but mix in a superposition described by a unitary 3×3 matrix called the *Cabibbo-Kobayashi-Maskawa* (CKM) matrix [120]:

$$\begin{pmatrix} |d'\rangle \\ |s'\rangle \\ |b'\rangle \end{pmatrix}_{\mathrm{L}} = \begin{pmatrix} V_{ud} & V_{us} & V_{ub} \\ V_{cd} & V_{cs} & V_{cb} \\ V_{td} & V_{ts} & V_{tb} \end{pmatrix} \begin{pmatrix} |d\rangle \\ |s\rangle \\ |b\rangle \end{pmatrix}_{\mathrm{L}} \tag{1.1}$$

Because this matrix has off-diagonal terms, the W boson mixes the three generations, e.g. the object that couples to the top quark is a linear combination of b, s and d quarks: $|b'\rangle = V_{td}|d\rangle + V_{ts}|s\rangle + V_{tb}|b\rangle$. Out of the nine complex arguments of this matrix, only four parameters are independent: three mixing angles and one phase. The latter is the only measured source of CP violation in the SM.

1.2 The top quark

The top quark resides in the third generation of quarks as the weak-isospin partner of the bottom quark. It was already known in the 1970's that, in order for the SM to be a renormalizable theory, the number of lepton and quark families should be equal. Therefore, the discovery of a third generation of leptons in 1975 [144] called for a third generation of quarks. The indirect evidence for the existence of the top quark became compelling after the discovery of the b-quark [100] and the subsequent need to complete the third weak-isospin quark doublet.
The first direct observation of the top quark occurred at the Tevatron, a proton-anti-proton collider located at the Fermilab laboratory, in 1995 [6, 10]. The latest combination of measurements performed by the Tevatron experiments CDF and DØ placed the mass of the top quark at $m_t = 173.2 \pm 0.9$ GeV [127] and this makes the top quark the heaviest fundamental particle of the SM. Due to this large mass that implies a Yukawa coupling $\lambda_{\mathrm{top}} \approx 1$ to the Higgs boson, the lifetime of the top quark is approximately 10^{-25} s, about two order of magnitude smaller than the characteristic time of the strong force

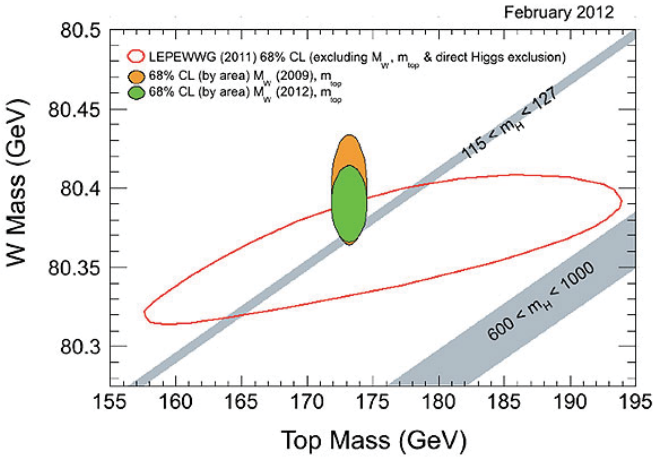

Figure 1.1: The latest result for the W boson mass combined with world's best value for the top quark mass, restricts the Higgs boson mass to the allowed range 115-127 GeV [5].

($\approx 10^{-23}$ s). This implies that the top quark decays before forming hadronic bound states giving us the unprecedented opportunity to study the decay products of a quark unperturbed by hadronization.

The discovery of the top quark was aided by the SM fit to the accurate electroweak measurements performed mainly at LEP that, being quadratically sensitive to the top quark mass and logarithmically sensitive to the Higgs boson mass through radiative corrections to the W-boson mass, successfully cast light on the top quark mass range before its discovery. This successful prediction gave evidence of the predictive power of the SM. More importantly, it gave confidence to exploit the large coupling of the top quark to the Higgs boson and constrain the Higgs boson mass using the SM fit to the electroweak precision data including the direct measurements of the top quark and W-boson mass. The red ellipse in Figure 1.1 shows the 68% CL indirect measurement of m_t and m_W from LEP data. The latest result for the W boson mass combined with world's best value for the top quark mass, restricts the Higgs boson mass to the allowed range 115-127 GeV [5]. As mentioned before, the new boson recently observed at the LHC has a mass of 125 GeV.

1.2.1 Top quark production in the Standard Model

The production of top quarks in hadronic collisions is either mediated by the strong force, a process resulting in a top quark-antiquark pair, or by the electroweak interaction in which case the top quark is produced singly. Due to the large coupling strength of Quantum Chromo Dynamics (QCD), the SM sector describing the strong interaction, the main production mechanism of top quarks at hadron colliders such as the Tevatron and the LHC is by pair production.

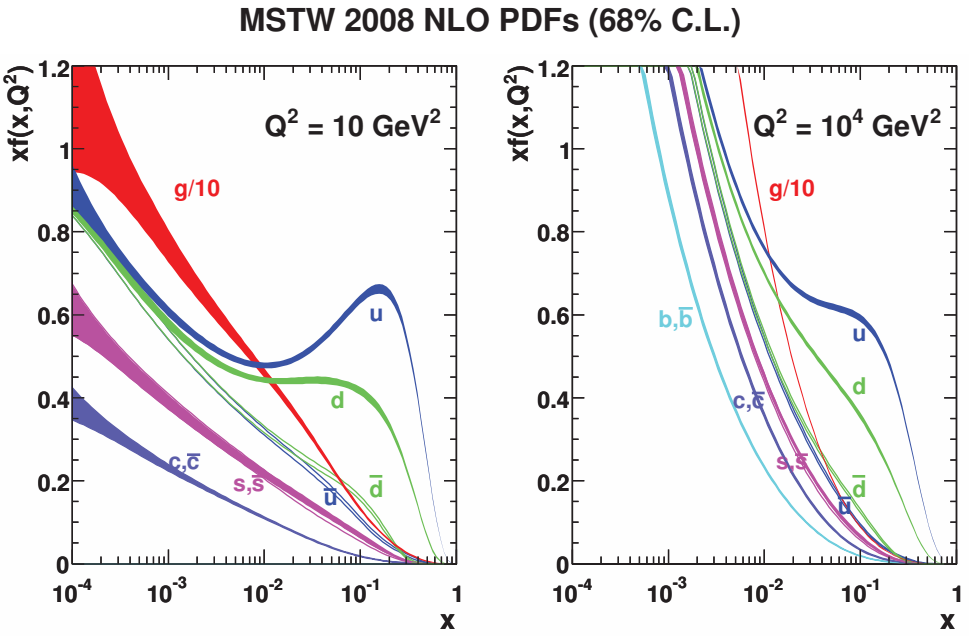

Figure 1.2: The momentum densities of the partons in the proton as a function of the longitudinal proton momentum fraction x at $Q^2 = 10$ GeV^2 (left) and $Q^2 = 10\,000$ GeV^2 (right) for the MSTW collaboration [132].

Top quark pair production

In high-energy hadronic collisions, the scattering process of the incoming particles takes place between the constituents of the hadrons, called *partons*. These are the valence quarks (three in the baryons and two in the mesons), which are responsible for the quantum numbers of the bound state, and a sea of quark-antiquark pairs arising from the conversion of the gluons binding the valence quarks [2].

At high energies, the collision between two hadrons can be factored into a hard-scattering cross section $\hat{\sigma}^{i,j}$ describing the short-distance interaction of two quasi-free partons i and j and long-distance terms describing the distribution of the longitudinal momentum of the colliding hadrons among their partons. These terms are called *Parton Distribution Functions* (PDFs) and are indicated as $f_i(x_i, \mu_F^2)$. They can be interpreted as the probability density to observe a parton i with longitudinal momentum fraction x_i at the scale μ_F^2. The arbitrary scale μ_F^2 is called the *factorization* scale since it sets the scale of this factorization of the total hadron-hadron cross section. The PDFs cannot be calculated a priori and are thus extracted in QCD fits to deep-inelastic scattering and other data. Figure 1.2 shows the parameterization of the proton densities obtained by the MSTW collaboration for two different values of the factorization scale $\mu_F^2 = Q^2$. Following the interpretation of the PDFs, we see that the probability of finding a quark of momentum

[2] The gluons are part of the sea and are commonly regarded as partons as well.

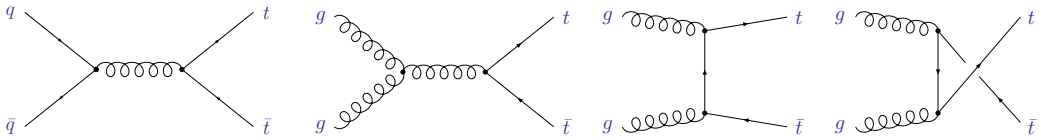

Figure 1.3: Set of leading-order Feynman diagrams contributing to heavy quark pair production in light quark annihilation.

fraction x decreases with increasing x [132].
The total top-quark pair-production cross section for the hard scattering of two colliding hadrons A and B can thus be written as:

$$\sigma(AB \to t\bar{t}) = \sum_{i,j} \int dx_i dx_j \, f_{i,A}(x_i, \mu^2) \, f_{j,B}(x_j, \mu^2) \times \hat{\sigma}^{i,j \to t\bar{t}} \left(\rho, m_t^2, x_i, x_j, \alpha_s(\mu^2), \mu^2\right) \quad (1.2)$$

where the sum runs over all possible pairs of partons, i.e. $q\bar{q}$, gg, qg and $\bar{q}g$ and $\rho = 4\,m_t^2/\sqrt{\hat{s}}$. Here $\hat{s} = x_i\,x_j\,s$ is the effective center-of-mass energy squared for the partonic process which depends on the total energy squared s available in the centre-of-mass of the collision. The hard parton-parton cross section $\sigma^{ij \to t\bar{t}}$ is calculated in perturbative QCD. The leading-order (LO) contributions come from light quark-antiquark annihilation and gluon-gluon fusion. The Feynman diagrams for these processes are depicted in Figure 1.3. The channels qg and $\bar{q}g$ appearing in higher-order calculations contribute only $O(1\%)$. The infinities arising in higher-order calculations are removed by a renormalization procedure which introduces another artificial scale, the renormalizable scale μ_R. It is common to set both μ_F and μ_R to the same value μ. To be consistent, all quantities in Equation 1.2 should be calculated at the same order in perturbation theory and defined in the same renormalization and factorization scheme. The most commonly employed scheme is the modified minimal subtraction scheme $\overline{\text{MS}}$ [22] and its extensions.
When the top quark pair production energy threshold is reached, $\hat{s}$ approaches a value of $4\,m_t^2$. Therefore, in the simplified scenario describing partons with equal momentum fraction, the value of x required to produce top quark pairs can be expressed by $x \approx 2\,m_t/\sqrt{s}$ showing manifestly that the parton momentum fraction decreases with increasing total centre-of-mass energy. By looking at Figure 1.2, it is now possible to see that for relatively large x the valence quark momentum density distributions are much larger than those of the other partons. This explains why at the Tevatron, a proton-antiproton collider, the dominant production mechanism was quark-antiquark annihilation. At the LHC the proton beams are accelerated to higher energies and the parton momentum fractions lie in the region where the gluon momentum densities are larger. This is why gluon-gluon initiated interactions make up about 80% of the total $t\bar{t}$ production at the LHC at 7 TeV despite having two proton beams, i.e. no valence antiquarks.
The next-to-leading order (NLO) quantum corrections to the heavy quark pair production cross section were calculated in Ref. [140] and [26, 27] more than 20 years ago. These results were then refined by resumming large logarithmic corrections of the form

$\log s/m_Q^2$ which originate from soft gluon emission and which, for hadronic production of heavy quarks, become sizable near threshold [153, 55, 56]. In the context of top quark pair production threshold logarithms were investigated and resummed by various groups first at leading logarithmic accuracy (LL) [123, 124, 31, 32, 33, 58, 57] and then also including the next-to-leading logarithms (NLL) [48, 50, 40]. The effect of these corrections was studied at the Tevatron, where the top quark pair production is relatively close to threshold, and at the LHC, where it is farther off. In both experimental setups the cross section is only mildly affected by the NLL corrections resulting in an increase of only a few percent. However, it also shows a more stable behaviour under variations of the factorization and renormalization scales on which the cross section depends [3].

Further studies on threshold logarithms resummation have been performed by Kidonakis et al. in Ref.[117, 116, 118, 112, 119] and Banfi et al. [21]. Moch and Uwer have provided an approximation of the NNLO cross section by performing and including a complete NNLL soft gluon resummation [136]. In Ref. [128] they also study the effect of independent variation of the renormalization and factorization scales. Figure 1.4 shows the contour lines of the total cross section at the LHC and at the Tevatron for different values of μ_R and μ_F. Here, the top quark (pole) mass is set to 173 GeV and the PDF set used is MSTW 2008 at NNLO accuracy and 68% CL. The resulting theory uncertainty is defined in the standard range $\mu_R, \mu_F \in [m_t/2, 2\,m_t]$ as:

$$\min \sigma(\mu_R,\, \mu_F) \leq \sigma(m_t) \leq \max \sigma(\mu_R,\, \mu_F). \tag{1.3}$$

They concluded that the independent variations of μ_R and μ_F does not lead to any significant change in the cross section and that the theory uncertainty is well estimated assuming identical scales $\mu_R = \mu_F$.

In Figure 1.5 the improvement of the approximate NNLO predictions is shown in comparison with the NLO cross section as a function of the top quark mass. For the LHC the predictions are shown at the design center-of-mass energy $\sqrt{s} = 14$ TeV and for the Tevatron $\sqrt{s} = 1.96$ TeV. The band summarizes the uncertainty stemming from the variation of the scales added linearly to the uncertainty of the PDFs, whose weak scale dependence in the standard range has been neglected [128].

Beside the QCD corrections to on-shell top quark production, other sources of corrections have been studied. In [35, 36] the top and anti-top spin degrees of freedom have been taken into account at NLO and these provide azimuthal correlations between the decay products of the top quark. The mixed effects of the QCD and the EW corrections, whose effect on the cross section is negative but small, have been computed by [122] and [37]. Lastly, the non-factorizable QCD corrections between production and decay have been studied in Ref. [25].

[3] Higher order corrections should improve our knowledge of the production cross section and, in particular, reduce its uncertainties related to the renormalization and factorization scale dependence.

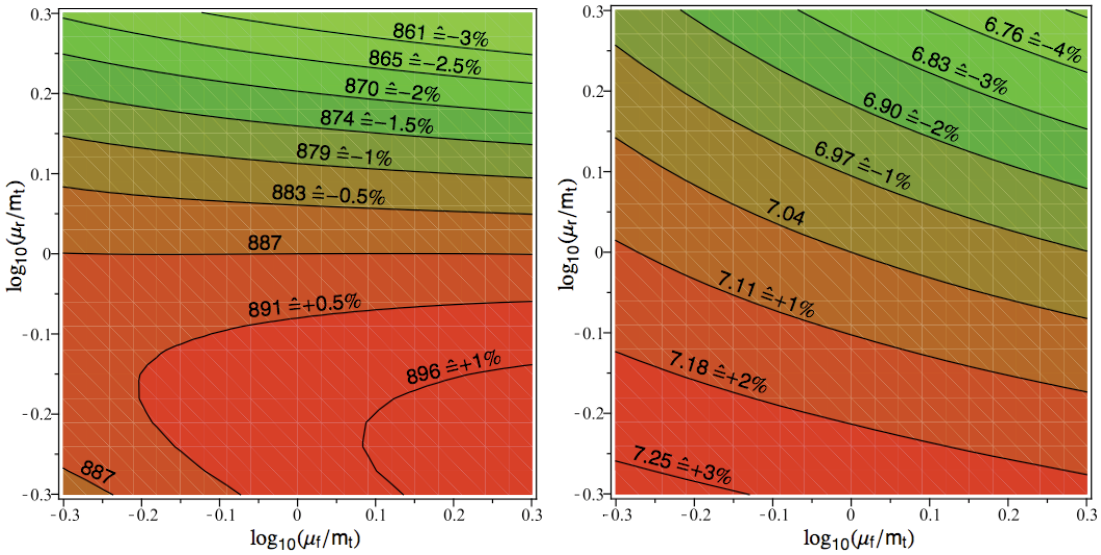

Figure 1.4: Contour lines of the total top quark pair production cross section in the (μ_R, μ_F) plane using MSTW 2008 for the LHC at $\sqrt{s} = 14$ TeV (left) and the Tevatron at $\sqrt{s} = 1.96$ TeV (right). The range shown corresponds to μ_R, $\mu_F \in [m_t/2, 2\,m_t]$ [128].

Single top production

The single production of the top quark has been recently observed for the first time at the Tevatron [4, 9]. The three distinct processes contributing to this production are governed by the charged-current weak interaction as one can see from the leading order Feynman diagrams depicted in Figure 1.6. These channels are proportional to the CKM matrix element $|V_{tb}|^2$ and therefore the cross section measurement of any of these single

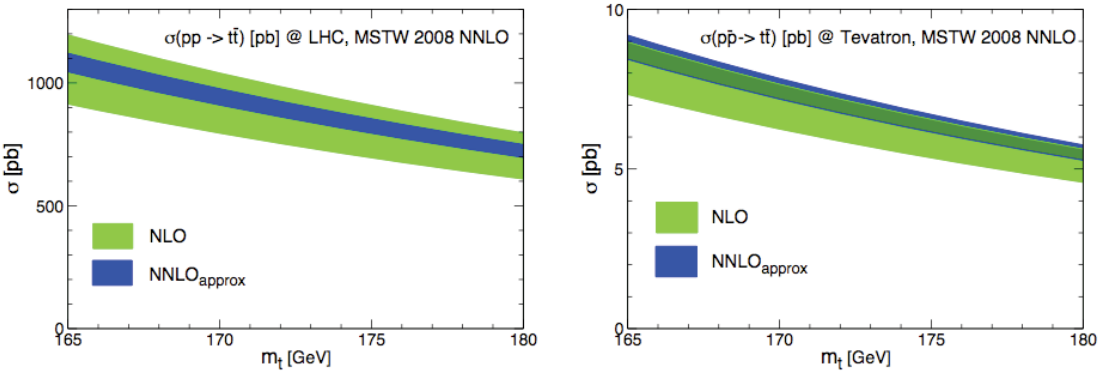

Figure 1.5: The NLO (green) and approximate NNLO (blue) cross section at the LHC (left) and at the Tevatron (right) obtained with the MSTW PDF set. The band denotes the theoretical uncertainty from scale variation ($\mu_F = \mu_R$) and the PDF uncertainty in the range $[m_t/2, 2\,m_t]$ [128].

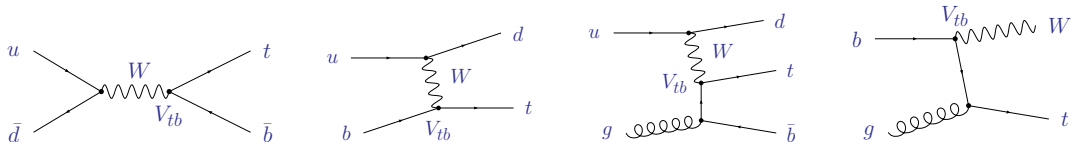

Figure 1.6: Leading order single top production diagrams. From left to right: s-channel, b-initiated t-channel, gluon-initiated t-channel and Wt associated production.

top production mechanism is a direct extraction of this matrix element.
The process that dominates the production both at the Tevatron and at the LHC is the t-channel represented by the two diagrams in the middle of Figure 1.6. The initial state b-quark can be considered to be a part of the proton with its luminosity described by a PDF set (middle left) or coming by the splitting of a gluon into a $b\bar{b}$ pair (middle right). However, the former is suppressed by the small b-quark PDF and thus the largest contribution comes from the gluon-initiated production.
The channel depicted in the diagram on the left-hand side of Figure 1.6 is called the s-channel. Due to its similarity to the Drell-Yan heavy vector boson production, the cross section for the single top production via s-channel is believed to be particularly accurate. However, the experimental signature is not especially distinctive with respect to other SM processes and this makes the direct study of the s-channel very challenging.
The Wt associated production mechanism (Figure 1.6 right) is relevant only at the LHC due to the low gluon luminosity at the Tevatron and the limited phase space to produce both a top quark and a W boson. At NLO, this channel is characterized by the same final-state objects as $t\bar{t}$ events.

1.2.2 Top quark decay in the Standard Model

At leading order in the SM, the top-quark decay width is given by:

$$\Gamma_t^0 = \frac{G_F\, m_t^3}{8\pi\sqrt{2}} \times |V_{tb}|^2 \tag{1.4}$$

where G_F is the Fermi coupling constant. At NLO the decay width is still proportional to $|V_{tb}^2|$ because the corrections that affect the coupling are negligible [80]. Neglecting terms of order m_b^2/m_t^2, α_s and $(\alpha_s/\pi)\, M_W^2/m_t^2$ the total width becomes [109]:

$$\Gamma_t = \Gamma_t^0 \left(1 - \frac{M_W^2}{m_t^2}\right)^2 \left(1 + 2\,\frac{M_W^2}{m_t^2}\right) \left[1 - \frac{2\alpha_s}{3\pi}\left(\frac{2\pi^2}{3} - \frac{5}{2}\right)\right]. \tag{1.5}$$

Because the top quark is heavy and its decay width scales like m_t^3, Γ_t is large: for $m_t = 170$ GeV, it is approximately equal to 1.3 GeV with a very small theoretical uncertainty. The experimental value obtained from Tevatron data is $\Gamma_t = 2.0^{+0.7}_{-0.6}$ GeV [7]. Since the scale at which QCD hadronization occurs ($\Lambda_{\mathrm{QCD}} \approx 200$ MeV) is smaller than Γ_t, the top quark lifetime τ_t is shorter than the time it takes to form a hadron: $\tau_t = \Gamma_t^{-1} < \tau_{had} = \Lambda_{\mathrm{QCD}}^{-1}$. Therefore the top quark is the only quark that decays before

having time to form hadronic bound states.
The top quark is coupled to the down-type quarks via the charged-current weak interaction with relative strengths proportional to the elements of the CKM matrix. Given the especially small values of the V_{td} and V_{ts} elements, peaking at 0.00862 and 0.0403 respectively [34], the tdW and the tsW couplings are suppressed. This implies that within the SM the top quark decays predominantly into a bottom quark and a W boson. The former subsequently hadronizes into a jet of hadrons while the latter further decays into either a quark-antiquark or a charged lepton-neutrino pair.
Everything being taken into account, there are three possible decay channels for top-quark pairs:

- $t\bar{t} \to W^+b\ W^-\bar{b} \to \ell\,\bar{\nu}_\ell\,b\ \bar{\ell}'\,\nu_{\ell'}\,\bar{b}$, called "dilepton channel" corresponding to about 10% of $t\bar{t}$ decays;
- $t\bar{t} \to W^+b\ W^-\bar{b} \to q\bar{q}'\,b\,\ell\,\bar{\nu}_\ell\,\bar{b} + \bar{\ell}\,\nu_\ell\,b\,q\bar{q}'\,\bar{b}$, called "semileptonic", "single lepton" or "lepton+jets" channel corresponding to about 43% of $t\bar{t}$ decays;
- $t\bar{t} \to W^+b\ W^-\bar{b} \to q\bar{q}'\,b\,q''\bar{q}'''\,\bar{b}$, called "hadronic" or "all-jets" channel corresponding to about 46% of $t\bar{t}$ decays.

Only events decaying into the semileptonic channel are selected for the work presented in this thesis. In addition, the events in which the charged lepton is a τ are not considered. This decision is driven by the fact that, when the τ lepton decays into a lighter charged lepton and a neutrino, the event, in addition to being more challenging to reconstruct, provides less information for the escape of the additional neutrino.

1.3 Top quark in beyond-Standard-Model physics

Because of its large mass, the top quark provides the largest contribution to the SM radiative corrections [4]. In particular, the stabilization of the Higgs boson mass is significantly affected by the presence of the top quark, a problem known as the "hierarchy problem".
In the one-loop radiative corrections to the Higgs boson mass, given by:

$$m_H^2 = (m_H^0)^2 + \frac{3\,\Lambda_{UV}^2}{8\pi^2 v^2}\,(-4m_t^2 + 2m_W^2 + m_Z^2 + m_H^2), \tag{1.6}$$

the bare Higgs boson mass squared $(m_H^0)^2$ has to be tuned in such a way that m_H is consistent with the indirect electroweak constraints, i.e. a Higgs boson mass lighter then about 200 GeV. In equation 1.6 Λ_{UV} indicates the energy scale above which we can no longer assume the validity of the SM. If we set this to the Planck scale M_{Planck}, above which we already know that the SM cannot be valid, the radiative corrections to the Higgs boson mass coming from the top quark, the weak bosons and the Higgs boson

[4] This is true if one assumes a Higgs boson that is lighter than the top quark, as direct and indirect evidence seems to prefer.

itself are about 30 orders of magnitude larger than this experimental constraint and thus $(m_H^0)^2$ should be of the same order of magnitude to provide us with a cancellation, a restriction often regarded as "unnatural". Since the quantum corrections from the top quark are the largest, the top quark plays a special role in many models that try to relax this fine tuning going beyond the physics of the SM.
Some models postulate the existence of new particles whose one-loop contributions have opposite sign and cancel the large SM corrections in Equation 1.6. The most popular example of such a solution is "Supersymmetry" [163]. In supersymmetric models each SM particle is given a supersymmetric partner of opposite statistics but otherwise identical. The radiative corrections to the Higgs boson mass due to the superpartners have opposite sign and this provides us with a natural solution to the hierarchy problem. However, since there is no experimental evidence for these new particles, supersymmetry must be broken and the supersymmetric particles heavier than their SM partners. In particular, to provide a mild fine tuning, the superpartner of the top quark can not be too heavy and should be accessible at LHC energies [43].
Some other models introduce new strong dynamics at the TeV scale. A typical example is "Topcolor" in which a new fundamental strong interaction is introduced. The new gauge bosons of these theories couple preferentially to the third generation and could for this reason be detected as $b\bar{b}$ or $t\bar{t}$ resonances [102].
Models with extra dimensions solve the fine tuning of the Higgs boson mass introducing new space-time dimensions. Also in this class of models there are new gauge interactions coupling to the third generation of matter. In particular, Kaluza-Klein excitations of the graviton, of the weak and strong gauge bosons couple to the top quark and would appear as resonances in the $pp \to X \to t\bar{t}$ production channel [88, 134, 81, 130].
Another idea is to introduce a fourth generation of fundamental particles. The new heavy, coloured fermion states could mix with the SM particles and this would loosen the indirect constraints from the unitarity on the CKM matrix and could have an impact on the V_{tb} element, important in single top production.
In general, the new physics related to the top quark affects the way this particle is produced or decays. If there is a heavy particle that couples to the top quark, this particle could decay in a top quark pair and contribute to the SM final state. We would observe a resonance in the $t\bar{t}$ invariant mass distribution. But for a very heavy resonance, the boost of the top quarks produced in its decay would entail a very small angular separation between the final state objects, a very challenging scenario from an experimental perspective. If, on the other hand, this new particle coupling to the top quark is light, the top quark would decay into it and we could observe a lack of events with respect to the SM expectations due to the non optimization of the $t\bar{t}$ selection for these new final states. Therefore, a precise measurement of the production cross-section in all decay channels offers a powerful tool to spot hints of new signals.

2 The LHC and the ATLAS detector

This chapter is intended to provide an overview of the experimental setup. The collision data used in this analysis have been provided by the Large Hadron Collider (LHC), described in the first section, and recorded by the ATLAS detector, presented in the rest of this chapter. These are very sophisticated machines and this overview can only cover the main features needed to understand the analysis presented in the rest of this thesis. More exhaustive descriptions can be found in e.g. Ref. [84] and [1].

2.1 The Large Hadron Collider

The Large Hadron Collider is a proton accelerator and collider ring with a circumference of 27 kilometers. It occupies the underground tunnel that was built for LEP, CERN's previous big accelerator, located at a medium depth of 100 meters[1]. The LHC is part of the CERN's complex of accelerators, shown in Figure 2.1. The protons are taken from hydrogen atoms stripped of their electrons, accelerated by a linear accelerator (Linac2 in Figure 2.1) to an energy of 50 MeV and injected in the PS Booster ring (PSB). The booster accelerates the protons to 1.4 GeV before sending them to the Proton Synchrotron (PS), where the energy is increased to 25 GeV. The Super Proton Synchrotron (SPS) receives the beam of protons from the PS and accelerates it to 450 GeV before finally transferring it to the LHC. The protons arrive at the LHC in bunches. The bunch structure of the beam is a direct consequence of the acceleration procedure by means of radio-frequency (RF) cavities. A charged particle traversing a RF cavity can only be accelerated when the oscillating electric field in the cavity has the correct orientation, which happens at a well-defined moment of the RF cycle. The LHC uses eight superconducting RF cavities per beam each delivering 2 MV at 400 MHz and operating at 4.5 K (–268.7 °C). The bunches circulating in the LHC contain about 10^{11} protons. They measure a few centimeters long and a millimeter wide when they are far from an interaction point but their size is squeezed by quadrupole magnets to 16 μm when they are about to collide to increase the probability of proton-proton head-on collisions with high momentum transfer. At nominal operating conditions, the two beams circulating in the LHC consist of 2808 bunches traveling in ultrahigh vacuum (10^{-13} atm) at an energy of 7 TeV (i.e. an energy of 14 TeV is available in the center-of-mass frame of the collision).
In order to bend the trajectory of the 7-TeV beams around the 27-Km ring of the LHC, 1232 dipole magnets provide a total magnetic field of 8.3 T. Figure 2.2 shows a diagram

[1] Due to geological and cost considerations the tunnel ring is tilted, its depth varying from 175 to 50 meters.

of the cross-section of a dipole magnet. Each dipole is 14.3 m long and weighs around 35 tonnes. The dipoles are superconducting and operate at 1.9 K, a temperature lower than the temperature of outer space, obtained by pumping superfluid helium in the magnet system.
The *instantaneous luminosity* is a measure of how many interactions occur per units of area and time. For a machine such as the LHC this quantity depends on the number N_b of protons per bunch, the number n_b of bunches per beam, the area of the cross-section of the beam, given by the its dispersions σ_x and σ_y in the transverse plane and lastly on the frequency f of the collisions:

$$L_{\text{instant}} = \frac{N_b^2 \, n_b \, f}{4\pi \, \sigma_x \, \sigma_y} \tag{2.1}$$

The design goal for the LHC is to reach a bunch spacing of 25 ns, which implies a frequency of 40 MHz, and an instantaneous luminosity of 10^{34} cm^{-2} s^{-1}. The head-on collision between two bunches circulating in opposite directions is referred to as *bunch crossing*. In each bunch crossing one or more pairs of protons may collide. The probabil-

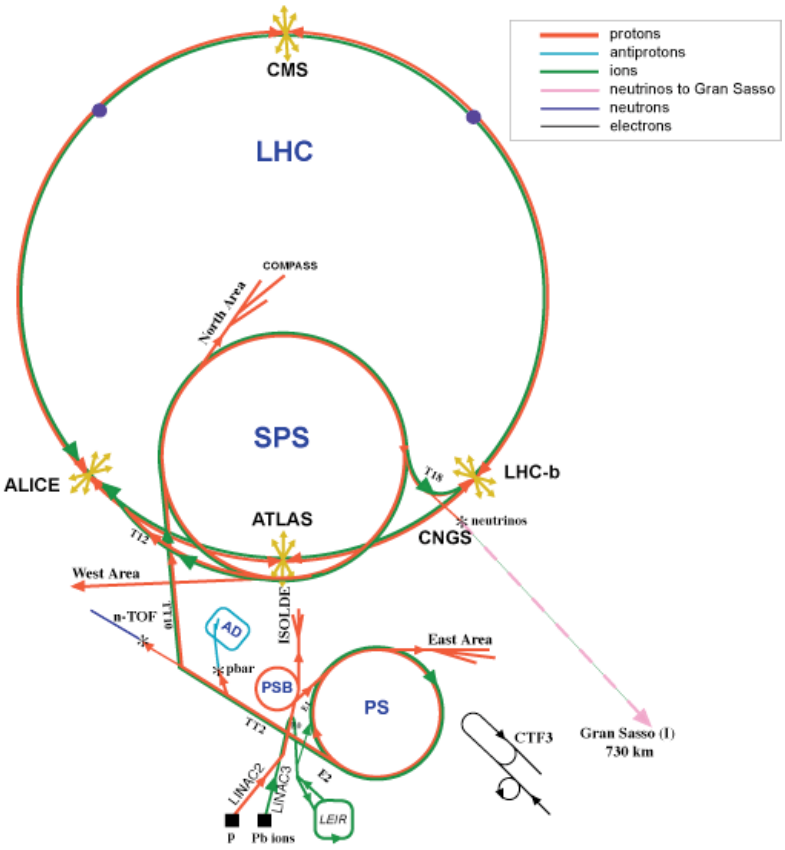

Figure 2.1: The accelerator complex of CERN [59].

ity to observe a certain number of proton interactions follows a Poissonian distribution. Multiple proton collisions are referred to as (in-time) *pile-up* [2] and the mean of the Poissonian is generally denoted by μ. The value of μ at a fixed number of bunches is mainly determined by the number of proton per bunch and their collimation and is proportional to the instantaneous luminosity.
The beams collide at four interaction points, where four experiments are installed to record the products of the collisions. The largest detectors are called ATLAS and CMS. The broad diversity of their physics programmes, most notably the discovery or the exclusion of the Higgs boson, is reflected in their typical general-purpose design. The other two experiments, LHCb and Alice, have specialized research programmes. Alice studies heavy-ion collisions (for which there have been dedicated runs of the LHC) and focuses on the physics of the strong interactions and the quark gluon plasma at extreme values of energy density and temperature. LHCb is specialized in precision measurements of CP violation and rare decays of b-hadrons as well as the search for indirect evidence of new physics in these processes.
The operation of the LHC started in September 2008 but it was interrupted only nine days after by a severe mechanical damage. It took more than one year to repair the failure and eventually the operation was resumed in November 2009. Since March 2010 the data taking proceeds at the reduced center-of-mass energy $\sqrt{s} = 7$ TeV. The bunch spacing, initially set to 75 ns, was reduced to 50 ns in 2011.

[2] Out-of-time pile-up refers to the residual effects in the detector due to events occurred in the previous bunch crossings

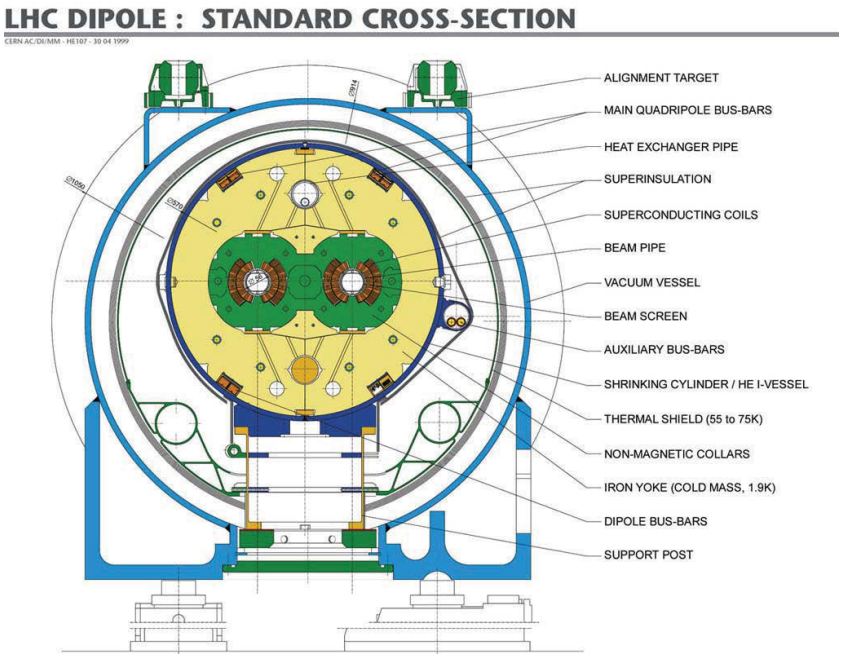

Figure 2.2: Cross-section view of a superconducting dipole magnet operating at the LHC [84].

The integral of the instantaneous luminosity with respect to time, called the integrated luminosity, is a measure of collision data collected. Figure 2.3 shows the day-by-day increasing peak instantaneous luminosity of the LHC in 2011 and the corresponding cumulative amount of events occurred and recorded by the ATLAS experiment. For the 2012 run, the energy of the colliding beams has been raised from 3.5 to 4 TeV, while keeping the bunch spacing constant at 50 ns. This will allow to collect in one year about 15 fb^{-1} of integrated luminosity, three times higher than in 2011. The LHC will be then shut down for a long upgrade period needed to prepare the machine for design-energy running.

2.2 The ATLAS detector

The ATLAS detector belongs to the class of so-called 4π detectors that adopt a cylindrical symmetry around the beam line and cover most of the 4π solid angle surrounding the interaction point. A common feature of this kind of detectors is that they consist of successive layers of instrumentation that can be usually grouped in an inner tracker, a calorimeter and an outer layer of muon detectors.
The inner tracker is immersed in a magnetic field and determines the momentum of charged particles by measuring the radius of the trajectory reconstructed by making multiple position measurements. Most of the particles that enter the calorimeter initiate a particle shower. The calorimeter absorbs the shower and measures the energy of the original particle. Because of their mass, the muons are unique in the depth which they can penetrate matter. They lose only little energy as they scatter off of atomic electrons in the calorimeters. This is why muon detection requires an additional layer of dedicated instrumentation placed beyond the calorimeter.
The ATLAS detector is shown in Figure 2.4: the 4π geometry is achieved by means of a central "barrel" in whose ends two symmetric "end-caps" are plugged.

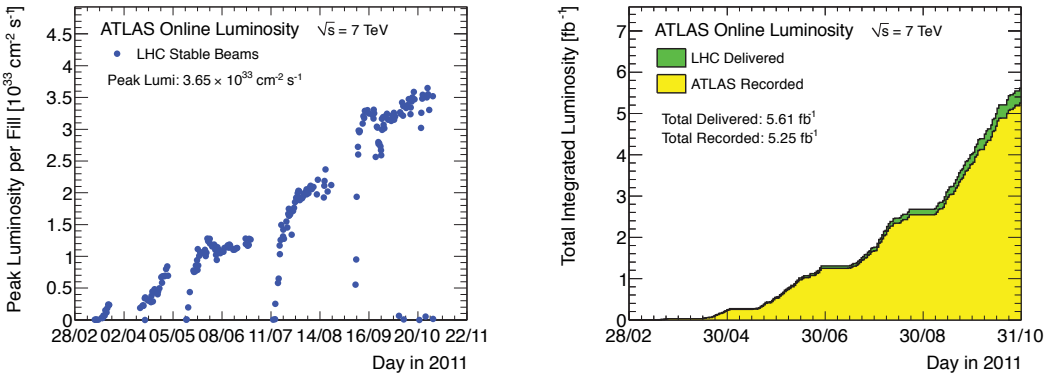

Figure 2.3: Maximum instantaneous luminosity (left) and cumulative integrated luminosity (right) versus day in 2011. The green distribution is the integrated luminosity delivered by the LHC and the yellow one represents the portion recorded by the ATLAS experiment [18].

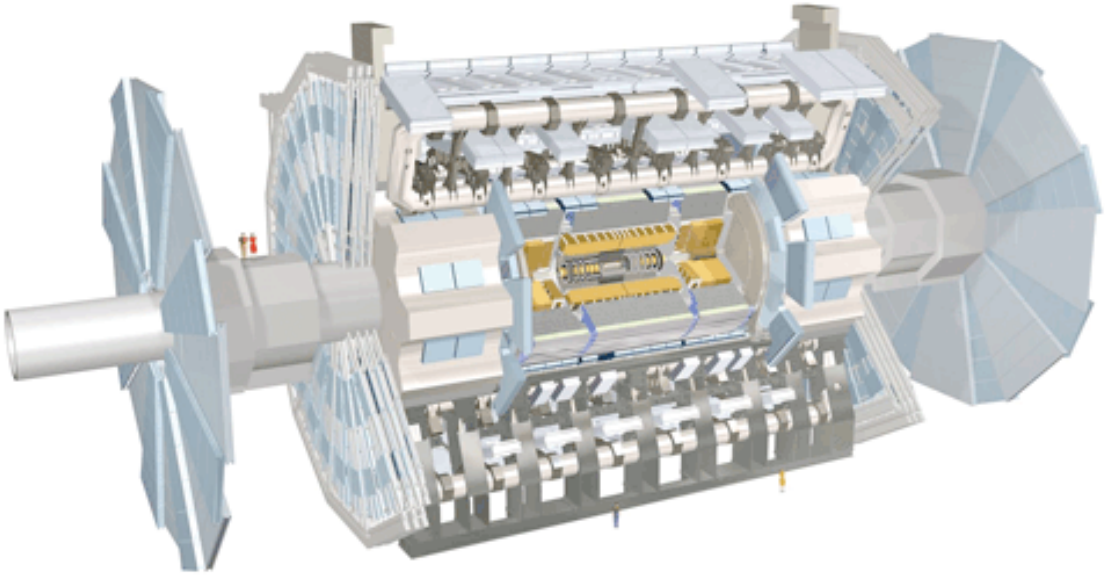

Figure 2.4: The ATLAS detector [1].

2.2.1 The ATLAS coordinate system

Positions in the ATLAS detector are given in a cartesian coordinate system with its origin in the nominal interaction point, the x axis pointing to the center of the LHC ring and the y axis pointing upwards. The z axis is oriented along the beam line and coincides with the detector axis. In the spherical coordinate system the inclination is given by the the polar angle θ starting from the positive z axis and the azimuth is given by the angular distance ϕ in the transverse plane from the positive x axis. The polar angle is commonly replaced by the pseudorapidity defined as:

$$\eta = -\ln\left[\tan\left(\frac{\theta}{2}\right)\right] \tag{2.2}$$

In the transverse xy-plane θ is 90° and η is 0. In the positive/negative z direction $\theta = 0°/180°$ and $|\eta|$ diverges. The detector region that corresponds to small absolute values of the pseudorapidity is usually defined as "central" while the "forward" direction refers to the regions that are close to the beam axis, at high $|\eta|$.
The distance in spherical coordinates is defined as:

$$R = \sqrt{\Delta\eta^2 + \Delta\phi^2}. \tag{2.3}$$

2.2.2 The magnet system

The Lorentz force law tells us that a magnetic field exerts a force on a moving charged particle that is the product of the particle's charge, its velocity, the magnetic field

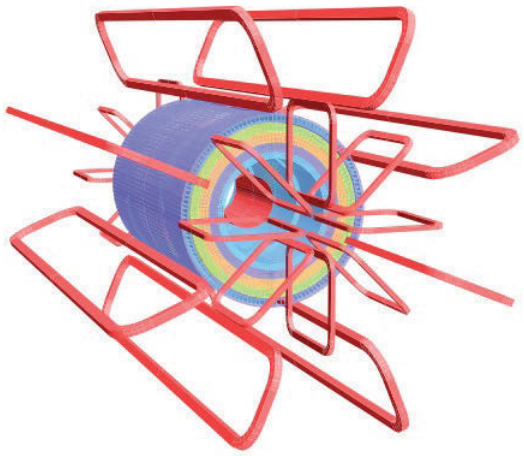

Figure 2.5: The magnet system of the ATLAS detector [1].

strength and the sine of the angle subtended between the particle's direction of motion and the direction of the magnetic field. This force is always perpendicular to both the magnetic field and the instantaneous direction of motion of the particle. It follows that the trajectory of a charged particle moving in an external magnetic field is deflected (in a direction parallel to this force) into a circular orbit whose radius r is proportional to the particle's momentum p: $r = p/qB$, where q and B are the charge of the particle and the magnetic field strength.
To measure the momentum of charged particles the ATLAS detector is equipped with the magnet system shown in Figure 2.5. An internal solenoid magnet provides the inner tracker with an almost uniform 2 T magnetic field. The solenoid is a superconducting magnet and operates at the temperature of 4.9 K. The second field is produced by a very ambitious system of three superconducting air core toroids placed inside the muon spectrometer. The barrel toroid covers $|\eta| < 1.4$ and the two in the end-caps $1.6 < |\eta| < 2.7$. This field is not uniform: it varies from 0.2 T and 3.5 T from barrel to end-caps. In the transition region at $1.4 < |\eta| < 1.6$ the fields overlap and result in a reduced field strength. Nevertheless the field is almost orthogonal to the muon flight direction and allows the momentum measurement of muons in the TeV range.

2.2.3 The inner detector

The Inner Detector (ID) provides charged particle tracking for $|\eta| < 2.5$. With the aid of the 2 T magnetic field provided by the solenoid magnet surrounding the ID, the reconstruction of tracks allows the measurement of the charged particle momenta and the identification of primary and secondary vertices. The ID is composed of three nested sub-detectors: the pixel detector is the innermost followed by the semiconductor tracker and the transition radiation tracker. The ID extends from a radius of about 50 mm to a radius of 1.15 m, with a length of 7 m. The radii of the first few layers and the

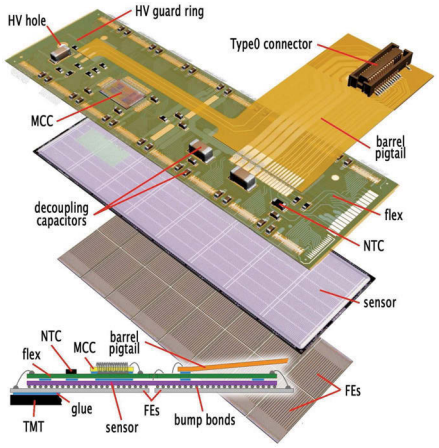

Figure 2.6: A schematic view of the three constituent layers of a pixel module [1].

strength of the magnetic field determine a lower limit to the transverse momentum (the momentum component in the transverse xy-plane) that the ID is sensitive to: particles produced with transverse momentum lower than ~ 0.5 GeV are bent considerably and do not cross enough layers of instrumentation to be identified.

The pixel detector

The pixel detector is composed of modules about 63-mm long and 19-mm wide. Each module consists of a doped silicon sensor, which represents the active part of the module, 16 front-end chips (FEs), whose primary function is to amplify and discriminate the charge collected from the sensor, and a module control chip (MCC) that distributes clock and triggers to the module and sends the data collected by the FEs to off-detector read-out drivers. Figure 2.6 shows the components of a single pixel module.

The sensors are 250 μm thick detectors having n-type implants in an n-type substrate, a feature that allows them to be operated with good charge collection efficiency also below

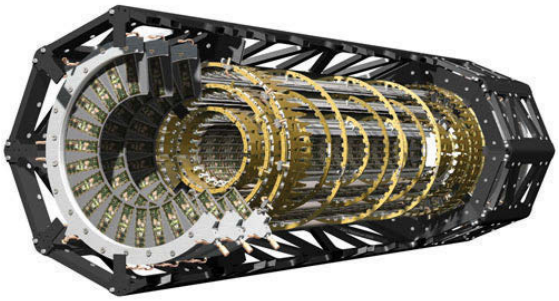

Figure 2.7: The ATLAS pixel detector [1].

depletion voltage [3]. Each of them contains 328×144 pixel cells of size $50\mu\text{m} \times 400\mu\text{m}$ that are connected to the front-end electronics by using bump bonding.
The single pixel acts as a pn-junction depleted of charge carriers by a reverse bias voltage that initially is $\sim$ 150 V, but that will be raised up to 600 V to ensure good charge collection efficiency after ten years of operation. A charged particle traversing the sensor ionizes the atoms forming electron-hole pairs that drift to the cathode and to the anode respectively. The collection of this charge from a single sensing element forms the basis of a "hit".
The pixel detector, shown in Figure 2.7, is constructed from 1744 modules. In the barrel these are arranged on three concentric cylinders around the beam axis. In the end-caps the modules are arranged into six disks perpendicular to the beam axis, three on each side of the interaction point. Each track typically crosses three pixel layers. The single module intrinsic accuracy of the hit position is 10 μm in the R-ϕ plane and 115 μm in the R-z plane. The high pixel granularity also guarantees low occupancy, with a low probability of "double-hits", a crucial requirement especially for high-luminosity runs of the LHC. Due to the large amount of ionizing radiation and neutrons that the pixel detector must withstand at such short distance from the interaction point, the modules have a limited lifetime. In particular, the current innermost barrel layer (B-layer) is expected to reach its radiation dose after approximately three years of operation at design luminosity. The remedy to this will actually not be a replacement of the current B-layer, but the insertion of an additional layer at a smaller radius [54]. This upgrade is scheduled for installation during the 20-month long shutdown in 2013-2014.

The semiconductor tracker

The semiconductor tracker (SCT) uses classic single-sided p-in-n technology with AC-coupled read-out strips. The sensors operate initially at $\sim$ 150 V bias voltage but, as in the case of the pixel detector, higher operating voltages will be required after ten years of operation due to intensive irradiation and subsequent change of effective doping concentration. Each silicon sensor has a thickness of 285 ± 15 μm and is segmented in 768 active strips.
The SCT is composed of 4088 modules. A single module comprises a baseboard glued between two planes of back-to-back detectors. The sensors on the front and back side of the module have a stereo angle of 40 mrad to provide positional information in two dimensions. In the barrel the modules are arranged in four concentric cylinders covering $|\eta| < 1.4$. In each end-cap the modules are distributed on 9 disks that allow particle tracking up to $|\eta| < 2.5$. The SCT comprises five different variants of modules with varying strip length and pitch for different parts of the detector.
The SCT lacks the segmentation of the pixel detector. However, being positioned at a larger radius, where the track density is smaller, it provides the best compromise between hit precision and affordability with over 63 square meters of sensor coverage against the 1.7 square meters coverage of the pixel detector. A drawing of the barrel and end-cap

[3] Such operation might be necessary if the full depletion voltage becomes excessively large after substrate type inversion caused by the high radiation fluence at the LHC.

SCT is shown in Figure 2.8 together with the pixel detector and the end-cap TRT (see next section). On average a track crosses eight strip layers providing four space-point measurements. The intrinsic accuracy of the hit position of a SCT module is 17 μm in the R-ϕ plane and approximately 580 μm in the R-z plane.

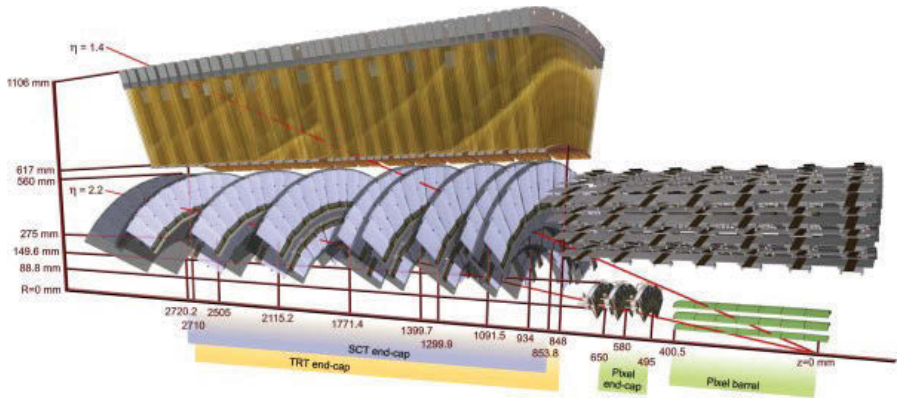

Figure 2.8: A drawing of the three subsystems of the inner detector [1]. Two charged tracks at $\eta = 1.4$ and $\eta = 2.2$ with a transverse momentum of 10 GeV are also shown. The track at $\eta = 1.4$ traverses successively three barrel pixel layers, four SCT end-cap disks and approximately 40 straws of the end-cap TRT. The track at $\eta = 2.2$ traverses only the first barrel pixel layer, two end-cap pixel disks, four SCT end-cap disks and misses the TRT whose coverage does not extend beyond $|\eta| = 2.0$.

The transition radiation tracker

The transition radiation tracker (TRT) provides continuous tracking of charged particles and electron identification via transition radiation. This low-intensity radiation is emitted when a charged relativistic particle crosses the interface between media with different dielectric properties. The transition radiation is composed of photons in the X-ray region emitted at a very small angle with respect to the particle trajectory.
The TRT is build from drift tubes with a diameter of 4 mm. The tubes are filled with a mixture of Xenon (70%), needed for its efficient X-ray absorption, carbon dioxide (27%) and oxygen (3%). A gold-plated tungsten anode wire of 31 μm diameter runs along the tube axis. A high voltage is applied between the wire and the tube so that the gas-filled area is immersed in an electric field. Similarly to semiconductor detectors, the passage of a charged particle ionizes the medium forming pairs of electrons and ions. The electrons drift toward the wire, ionizing other atoms on their way and giving rise to an avalanche multiplication that amplifies the signal and allows its read-out. The charge collected on the wire is proportional to the energy loss of the primary ionizing particle and the arrival time of the signal defines the drift radius of the electrons and thus the track position of the primary particle in the R-ϕ plane. The 4 mm diameter of the tubes together with the gaseous mixture chosen give 48 ns maximum collection time of the signal. In particular, the carbon dioxide provides a plateau of constant drift velocity over a large drift range, low longitudinal diffusion and small electron deflection in the presence of

the external magnetic field.
The barrel TRT consists of three concentric cylinders in which the tubes are placed parallel to the beam. Each of the two end-caps consists of three sets of identical wheels in which the tubes are placed radially. The tube wall was developed to have a good transition radiation yield: it is made of two 35 μm thick multi-layer films bonded back-to-back. Each film is made of a 25 μm thick polyimide layer coated on one side with a 0.2 μm layer of aluminum protected with a 5 μm graphite-polyimide layer and on the other side with a 5 μm polyurethane layer. To improve the mechanical properties of the tubes, the walls are reinforced by carbon fibers.
The TRT only provides R-ϕ information. It contributes to the momentum measurements by performing a large number of position measurements (on average 35 per track) with a precision of about 130 μm.

2.2.4 Calorimetry

Calorimeters are detectors that measure the energy and the position of particles which, in the process, are usually absorbed. Each calorimeter is made of multiple, individual cells aligned to form towers. The analysis of the energy released in cells and towers also permits to measure the lateral and longitudinal profile of particle showers. Typically, incident electromagnetic particles, i.e. electrons and photons, initiate a relatively short and concentrated electromagnetic shower and are fully absorbed by electromagnetic calorimeters. Incident hadrons, on the other hand, may start showering in the electromagnetic calorimeter but then be fully absorbed only in the surrounding hadronic calorimeter.
The calorimeters also provide signatures for particles that are not absorbed, like muons and neutrinos. Muons do not shower, but they deposit an ionization signal which, at LHC energies, is approximately of a few GeV. Neutrinos on the other hand leave no signal but their presence can be inferred by energy conservation: in an hermetically closed calorimeter the escape of a neutrino is detected as missing energy.
The ATLAS calorimetry system is subdivided into an internal electromagnetic calorimeter, an external hadronic calorimeter and a forward calorimeter as shown in figure 2.9.

The electromagnetic calorimeter

The most common interaction for electrons above 10 MeV in a dense medium is bremsstrahlung [164]. When bremsstrahlung occurs, an electron decelerates through Coulomb interaction with a nucleus in the medium and emits photons. These photons can undergo further reactions: for a photon above 10 MeV the production of electron-positron pairs is dominant. Further reactions of these particles propagate the shower.
The radiation length X_0 defines the average distance over which the energy of an electron is reduced by a factor of $1/e$ due to radiation losses. X_0 is found to be:

$$X_0 \approx \frac{716.4\ A}{Z(Z+1)\ln(287/\sqrt{Z})}\ \mathrm{g/cm^2} \tag{2.4}$$

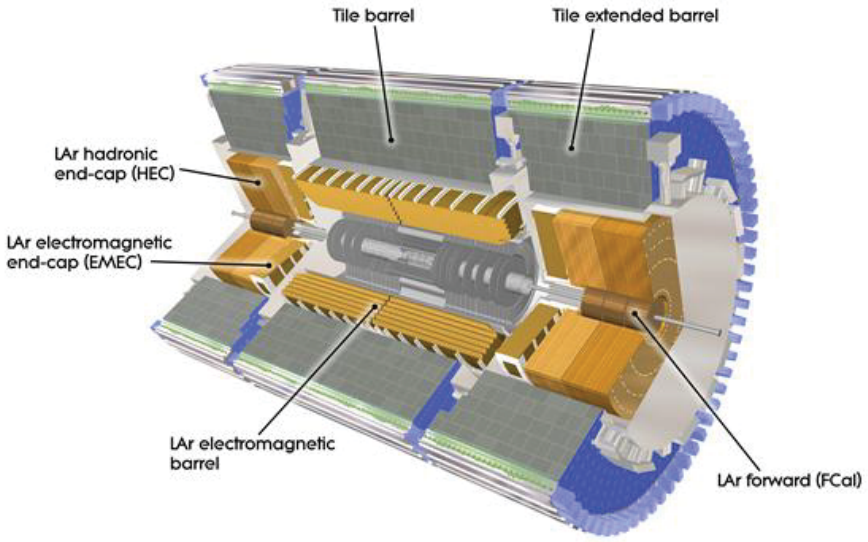

Figure 2.9: The ATLAS calorimeter system [1]. The calorimeter called Tile is the hadronic calorimeter.

where A is the atomic mass number of the material and Z is its atomic number. The absorption length of a photon can be approximated as:

$$X_p = \frac{9}{7} X_0. \tag{2.5}$$

The shower proceeds by bremsstrahlung and pair production until the particles reach the energy (the critical energy ϵ_C) at which the ionization starts to be the most probable process. At this stage the energy loss is described by the Bethe formula:

$$\frac{dE}{dx} = \frac{4\pi N_0 z^2 e^4}{m\beta^2} \frac{Z}{A} \left[\ln \left(\frac{2m\beta^2}{I(1-\beta^2)} \right) - \beta^2 \right]. \tag{2.6}$$

Here m and ze are the incident particle's mass and charge, β is its velocity expressed as v/c, N_0 is the Avogadro's number and I is the mean excitation potential of the medium. The lateral spread of an electromagnetic shower can be expressed in units of the Molière radius, defined as:

$$R_M = \frac{21 \text{ MeV}}{\epsilon_C} X_0. \tag{2.7}$$

where ϵ_C represents the critical energy. Approximately 95% of the lateral spread of electromagnetic showers is contained within $2R_M$.
The ATLAS electromagnetic calorimeters (LAr in figure 2.9) have alternating layers of liquid argon, which represents the active material, and lead absorbers arranged in an accordion geometry. Such a geometry provides naturally a full coverage in ϕ without

cracks and a fast extraction of the signal. Liquid argon is chosen for several reasons: it has a high electron mobility, allowing for quick measurements, it is a noble gas which does not capture free electrons, thus minimizing signal losses, and it is radiation hard. The LAr calorimeters cover the pseudorapidity range $|\eta| < 3.2$.
Figure 2.10 shows the three sampling layers of the LAr calorimeter at $\eta = 0$. The electromagnetic showers start in Layer 1 which has a radiation length of 4.3 X_0 and is highly segmented to assist the ID in the precision measurements of electrons and photons. Most of the electromagnetic shower propagates through Layer 2 which corresponds to 16 X_0. Only a small fraction of the shower is expected to reach Layer 3 which is only installed at $|\eta| < 2.5$.

The hadronic calorimeter

Hadronic showers are not as well understood as the electromagnetic ones, but some models offer useful descriptions. In the spallation model, the hadronic showers are described as the interaction between fast-traveling hadrons and the nucleons of the medium which, as a result, are expelled from their nuclei and undergo further reactions in the detector. The excited nuclei eventually emit photons to reach their ground state thus creating additional particles to the original hadron. There is a great variation between any two hadronic showers, but some average quantities can be defined.
The nuclear interaction length defines the mean length a hadronic particle would travel before undergoing an inelastic collision and it is given very roughly by:

$$\lambda_I \approx 35 \text{ g cm}^{-2} A^{\frac{1}{3}} , \tag{2.8}$$

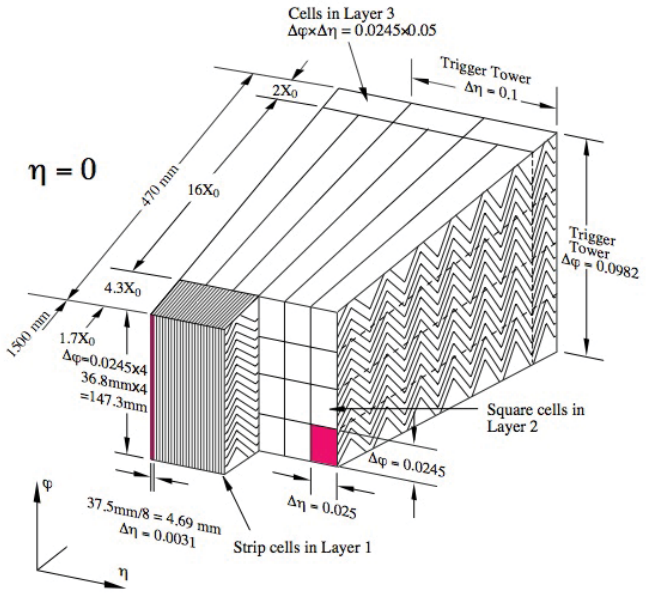

Figure 2.10: The three sampling layers of the ATLAS LAr calorimeter at $\eta = 0$ [1].

where A and ρ are the atomic mass number and the density of the material the particle is passing through. The particles created in the shower carry a smaller and smaller fraction of the primary particle's energy. The depth of the shower at which 95% of the energy is contained is a function of the nuclear interaction length and the energy of the primary hadron and is expressed by [17]:

$$L(95\%) \approx 2.5\,[0.54 \ln E(\mathrm{GeV}) + 0.4]\,\lambda_I. \tag{2.9}$$

In ATLAS, the hadronic calorimeter covers $|\eta|<1.7$ in the barrel and $1.5<|\eta|<3.2$ in the end-caps. The barrel is a cylinder divided into three sections: the central barrel covers $|\eta|<1$ and two extended barrels at $0.8<|\eta|<1.7$. These are constructed from plastic scintillator plates called "tiles" embedded in iron absorbers. The secondary particles created in the absorber produce light flashes in the tiles. The light is collected by wavelength shifting fibers and led to photomultipliers that produce a signal proportional to the light yield. The tile calorimeter consists of three sampling layers with a total interaction length of $9.7\lambda_I$ at η=0. This is sufficient to shield the outer muon spectrometer from hadronic showers. At larger η the requirement of radiation hardness imposes the use of liquid argon as active material and absorbers made of copper. Each one of the end-cap hadronic calorimeter consists of two wheels that provide in total four sampling layers.

The crack region

There is a gap between the barrel and the end-cap calorimeters called *crack* or *transition* region. This region is filled with cables and services for the inner detector and the electromagnetic calorimeter and therefore can be only partially instrumented. A number of scintillators is installed in the gap to provide us with an estimate of the energy loss of particles traversing the inactive material. The analysis presented here discards events with electrons falling in the crack region.

The forward calorimeter

In the extreme forward region $3.1<|\eta|<4.9$ another calorimeter is installed 4.7 m away from the interaction point. The particle flux in this region is very high and liquid argon is again used as active material for its radiation hardness. The forward calorimeter is divided into three segments: the first uses copper absorbers and is optimized for electromagnetic energy measurements. the outer two layers have tungsten absorbers and are used for hadronic calorimetry. In total, the three layers add up to ~210 X_0 and ~$10\lambda_I$.

2.2.5 The muon spectrometer

The Muon Spectrometer (MS) extends over 40 m in length and 20 m in height and covers up to $|\eta| < 2.7$. Because of their large mass muons are highly penetrating particles: they leave a track in the inner detector and pass through the dense calorimeters depositing only little energy. Furthermore, muons are long-lived enough to travel several meters

and fly out of the detector. For high momentum muons the resolution of the inner detector is insufficient[4]. The MS is designed to provide an independent momentum measurement with a resolution of $\sigma_{p_T}/p_T = 10\%$ for muons with $p_T = 1$ TeV. To achieve such a precision, four different tracking technologies are used: precision measurements are performed by monitored drift tubes and cathode strip chambers and fast muon triggering is provided by thin gap chambers and resistive plate chambers.

MDTs and CSCs

Over most of the pseudorapidity range precision measurements are provided by monitored drift tubes (MDTs) but at large η ($|\eta| > 2$) and close to the interaction point cathode strip chambers (CSC) with higher granularity are used to sustain the demanding particle flux.
The MDTs are aluminum tubes with a diameter of 3 cm. A 50 μm diameter anode wire made of tungsten and rhenium run through the center of the tube. They are filled with a gas mixture consisting of 93% of argon and 7% carbon dioxide kept at a pressure of 3 bar. Just like the straw tubes of the TRT, a high voltage is applied between the wire and the tube and an electric field is created between them. The muons traverse the tubes and ionize the gas. The stripped electrons drift to the wire generating an avalanche multiplication proportional to the energy deposited by the muon. The maximum drift time is about 700 ns and the single wire resolution is about 80 μm. The tubes are arranged in multilayer chambers, and the chambers are organized into stations. At a given ϕ in the barrel three stations arranged radially form a sector. The diagram in figure 2.11 shows a detailed view of three barrel sectors in the transverse plane. In the end-caps the chambers are arranged in three wheels, separated by roughly 7 m.
The CSCs are multi-wire proportional chambers with segmented cathode strips and a wire spacing of 2.5 mm. They are filled with a gas mixture composed of 80% argon and 20% carbon dioxide and the maximum drift time is approximately 30 ns. The measurement of the charge induced on the cathode by the avalanche formed on the anode wire gives the coordinates. The strips of one cathode are arranged perpendicularly to the radial anode wires to give the measurement of θ. A second set of cathode strips parallel to the wires provide the second spatial coordinate ϕ. Good spatial resolution is achieved by segmentation of the read-out cathodes and by charge interpolation between neighboring strips. The finer granularity of the CSC chambers is needed in the forward region, where the track density is higher. 32 CSC chambers are installed in the innermost layer at $2.0 < |\eta| < 2.7$.

RPCs and TGCs

In addition to the high-precision tracking detectors, the MS is instrumented with a dedicated trigger system that covers $|\eta| < 2.4$. It comprises two different technologies:

[4] The resolution of the momentum measurement of tracking detectors such as the inner detector depend on the curvature of the track. The higher the momentum, the more the track segment of a charged particle in the inner detector can be approximated by a straight line and it then becomes impossible to determine the momentum.

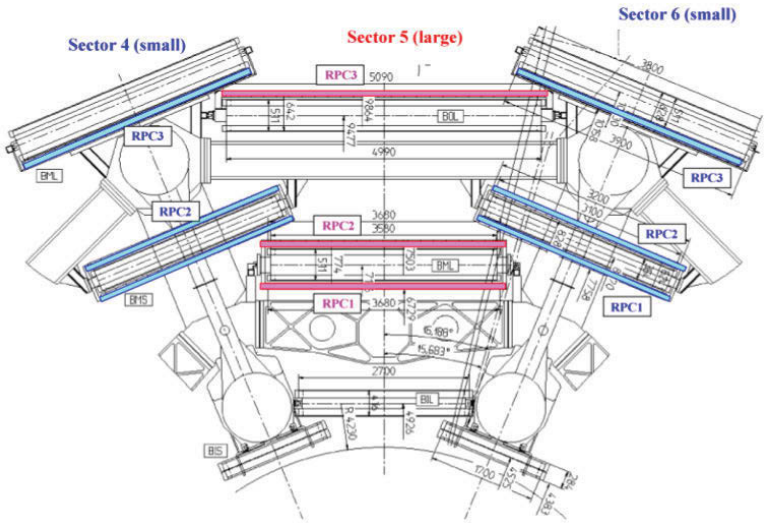

Figure 2.11: Transverse view of three barrel sectors, each with three stations of MDT chambers. The circles indicate the toroid magnets whose axis is normal to the plane of the page. The colored panels on one side of the outer station and either side of the middle station are the RPC trigger chambers (see text) [1].

resistive plate chambers (RPCs) are used in the barrel and thin gap chambers (TGCs) are employed in the end-caps. Both types of trigger chambers have an excellent time resolution of only 20 ns and also provide a second measurement of the track coordinates orthogonal to the precision measurements obtained with the MDTs and the CSCs. The RPCs are gaseous parallel electrode-plate detectors. There are two plastic resistive plates separated by an insulating spacer with a 4.9 kV/mm electric field between them. Each chamber has two independent detector layers. There are three chambers in each sector of the barrel: one on each side of the middle layer of drift tube chambers and one near the outer layer of drift tube chambers (Figure 2.11). The TGC are multi-wire proportional chambers similar to the CSCs operated in saturation mode to guarantee a quick response. The gas mixture is 55% carbon dioxide and 45% n-pentane. There are 3588 TGCs installed at $1.05 < |\eta| < 2.7$. Depending on their position, the TGCs give a resolution of $\Delta\eta =$ 7-36 mm and $\Delta\phi =$ 2-3 cm.

2.2.6 The trigger system

The input event rate for ATLAS is in the GHz regime. It is neither desirable nor possible to write out every event that occurs. A system of hardware and software collectively called the trigger is in place to select only the interesting ones and reduce the initial rate by several order of magnitudes. The ATLAS trigger menu - the list of conditions that have been deemed sufficient to justify keeping an event - has up to 256 items. However most of them require at least one of four basic conditions: an electromagnetic object (an electron or a photon), a jet of hadrons, an imbalance of energy on the transverse plane

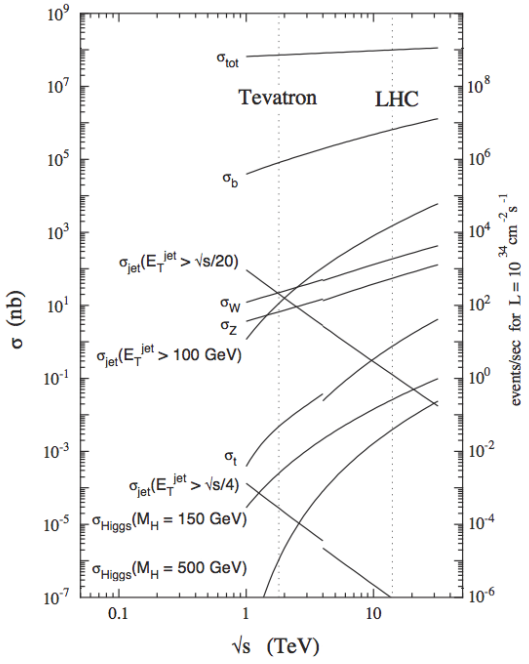

Figure 2.12: Cross-sections and rates for a luminosity of 10^{34} cm^{-2}s^{-1} in proton-(anti)proton collisions as a function of the center-of-mass energy [108].

of the detector or a muon.
Figure 2.12 shows the cross-sections and the rates of some processes at the LHC's design energy and luminosity. The manageable data storage rate is about 200 Hz. This requires an overall rejection factor of 5×10^6. To obtain such a reduction, there are three consecutive trigger levels in ATLAS: candidate objects are first identified and crudely reconstructed at the first trigger level and then processed in the second and third levels, collectively known as the high level trigger (HLT).

Level 1 trigger

The Level 1 trigger (LVL1) makes the initial selection based on reduced-granularity information of the activity in the muon trigger chambers and the calorimeters. It is a hardware trigger whose components are directly integrated into the ATLAS sub-detectors. Low and high momentum muons are identified by reconstructing the track segments in the RPCs and the TGCs using coincidence windows for discrimination. A schematic view of the muon trigger system is shown in Figure 2.13: low momentum muons have a smaller bend radius and are identified by the first two layers of RPCs in the barrel and the last two of TGCs in the end-caps. High momentum muons are characterized instead by a straighter track and the coincidence layers used are the first and the last one. Finally, the classification of the muon transverse momentum is achieved by using look-up tables of track hits containing information of transverse momentum thresholds. The calorimeter trigger at this level is based on low resolution information from all the

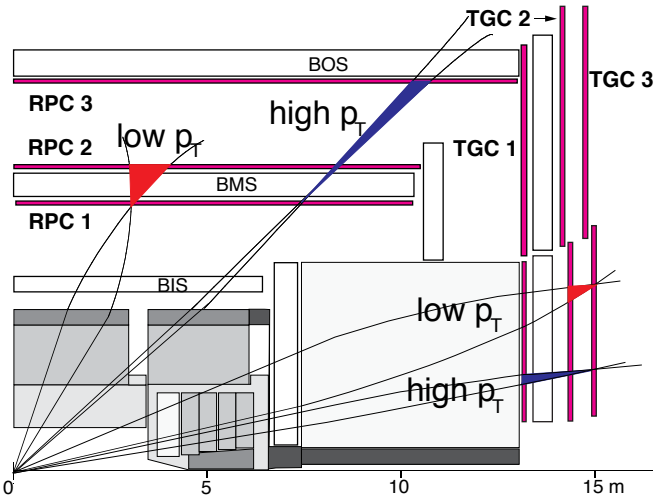

Figure 2.13: Low transverse momentum and high transverse momentum muons traversing the RPC trigger chambers [1].

ATLAS calorimeters (electromagnetic and hadronic; barrel, end-cap and forward). It is designed to search for high transverse momentum electrons, photons, jets and tau leptons decaying into hadrons, as well as large missing and total transverse energy. Here, the transverse energy is defined by the the sum of all vectored energy depositions $\vec{E}_T$ in the transverse plane. Since the initial transverse momentum of the incoming protons is approximately zero, the total vector sum over the transverse energy of the final states has to remain at zero. Hence, the missing transverse energy is defined as:

$$\vec{E}_T^{Miss} = -\sum \vec{E}_T. \tag{2.10}$$

The LVL1 trigger also identifies the bunch-crossing uniquely. The nominal bunch-crossing interval is 25 ns but whilst this is comparable to the muon time-of-flight through the MS, the pulse shape of the calorimeter signals extend over many (typically four) bunch crossings. The maximum L1 accept rate which the detector read-out systems can handle is 75 kHz and the the target latency is 2.5 μs after the bunch-crossing with which it is associated. During this time the information for all detectors channels is retained in pipeline memories contained in custom integrated circuits placed on or near the detector.

The high level trigger

After a LVL1 accept, events are read out from the pipeline memories and stored in read-out buffers until they are processed by the second level trigger, LVL2. LVL1 sends LVL2 the coordinates of detector regions where potentially interesting physics objects are detected (called Regions Of Interest, ROI), together with a rough estimate of the transverse momentum of the candidate object and the event energy sums. With an increased processing latency of 10 ms due to an input rate reduced by LVL1, LVL2 accesses data from the read-out buffers, if necessary with full precision and granularity.

This is a software-based trigger that runs on dedicated computing farms. Despite the fact that LVL2 has more time to make its decision, the selection algorithms at this stage still have to be kept simple and efficient. It is expected that LVL2 reduces the rates to about a few kHz. The event filter (EF) is the final level of on-line selection. It is a software trigger that runs on dedicated farms and works with the full event information collected by the read-out buffers. The EF also performs tasks such as vertex reconstruction and final track fitting. The algorithms applied at this stage are similar to those used in the subsequent off-line reconstruction of selected events. The EF reduces the event rate to approximately 200 Hz, with an average single-event processing time of about four seconds.

2.2.7 Luminosity detectors

The luminosity is a crucial ingredient in all cross-section measurement. ATLAS is equipped with a number of luminosity detectors. The Beam Condition Monitor (BCM) [64] is primarily designed to monitor beam losses and provide fast feedback to the accelerator team. It consists of two arms of diamonds sensors located at $z = \pm 184$ cm and $r = 5.5$ cm. The BCM counts the single-sided and coincidence rates as a function of the Bunch Crossing IDentifier thus providing us with bunch-by-bunch rates not subject to the deadtime of the ATLAS data acquisition system. The virtue of this detector as luminosity monitor is in its fast response of only 0.7 ns which allows for rejection of backgrounds from beam-halo (interactions of the beams with the collimators, see next chapter). LUCID [1] is the main relative luminosity monitor in the ATLAS experiment. It is located at $z = \pm 17$ m and $|\eta| \approx 5.8$ and it detects charged particles from inelastic proton collisions in the forward direction in order to measure the integrated luminosity and to provide on-line monitoring of the instantaneous luminosity and beam conditions. LUCID is constructed from aluminum tubes filled with gas (C_4F_{10}) pointing to the interaction region. The charged particles that enter these tubes emit a cone of Cherenkov light that is collected at the other end of the tube where photo-multipliers read out the signal. The goal of LUCID is to measure the luminosity with an uncertainty of better than 5%. LUCID and BCM are the two detectors primarily used for the measurement of the luminosity in 2011.
Farther away from the interaction point there are also ALFA and ZDC [1]. ALFA is a scintillating fibre detector inserted in the beamline at $z = \pm 240$ m and it measures the elastic proton-proton Coulomb scattering at very small angles. The optical theorem connects the elastic-scattering amplitude in the forward direction to the total cross section and can thus be used to extract the absolute luminosity. The Zero-Degree Calorimeter detects the neutrons and the photons with $|\eta| > 8.3$ in both proton-proton and heavy ion collisions. It is located at $z = \pm 140$ m. It consists of one electromagnetic calorimeter module corresponding to about 29 radiation lengths followed by three hadronic modules each of about 1.14 interaction lengths.

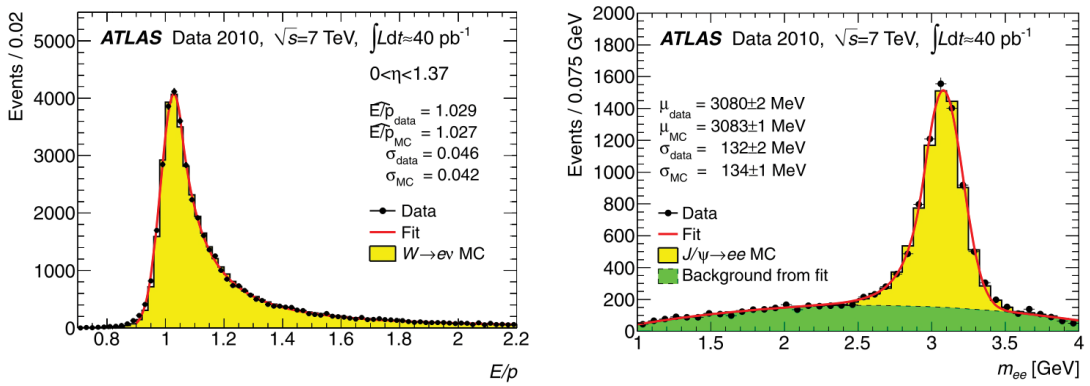

Figure 2.14: On the left, E/p distribution of electrons from $W \to e\nu_e$ events selected in the barrel EM calorimeter ($0 < \eta < 1.37$) in data and in simulation. On the right, reconstructed di-electron mass distribution for $J/\psi \to ee$ decays. The data are compared to the sum of the simulated signal and background contribution [2].

2.3 Object reconstruction and identification

2.3.1 Track reconstruction in the inner detector

The reconstruction of tracks in the ID is divided into three main steps. In the first step the hits in the pixel and SCT are converted into clusters and transformed into space points and the timing information in the TRT is converted into calibrated drift circles. A track-finding stage follows: track seeds are first formed from the space points in the three pixel layers and the first SCT layer. Track candidates are obtained by extending these seeds through the outer SCT layers and fitted excluding outlier clusters. Good tracks are required to have a limited number of holes (i.e. no hits in a given layer) and clusters shared with other tracks. The selected tracks are extended into the TRT and refitted with the full information of all three sub-detectors. The quality of the refitted tracks is compared to the previous track candidates of the silicon detectors: the hits on the extended tracks that result in a bad fit are labelled as outliers.
At an advanced stage of event reconstruction dedicated vertex algorithms using exclusively ID information are used to reconstruct primary and secondary vertices. The primary vertex is selected requiring the largest transverse momentum sum calculated from the transverse momenta of all the tracks associated to it.

2.3.2 Electron reconstruction

Accurate reconstruction of electrons is difficult because of the harsh environment dominated by QCD multi-jet events and the significant energy loss of electrons in the inner detector. Electron reconstruction starts in the electromagnetic calorimeter: it is seeded using a sliding-window algorithm with a window size corresponding to 5×5 Layer-2 cells. A cluster is then reconstructed around this seed. The number of cluster cells is

fixed but varies with $|\eta|$: for electrons (and converted photons) in the barrel the energy is collected over an area of 3×7 cells whereas in the end-caps this area corresponds to 5×5 cells. The position and the energy of the reconstructed cluster are then corrected: in particular the energy corrections optimize the energy resolution and the linearity of the response using η-dependent weights. In the standard electron reconstruction the cluster seed is matched with a reconstructed track in the inner detector. Further combined reconstruction properties, such as the ratio between the cluster energy and the track momentum and the cluster position and the track direction, are used to identify electrons. The inner-detector momentum measurement is not expected to improve the electron energy measured in the calorimeter. However, the electron flight direction in η and ϕ is better determined from the associated track. The left-hand side of Figure 2.14 shows a comparison of the energy E measured by the electromagnetic calorimeter to the momentum p of the electron track measured by the inner detector. The ratio E/p is shown for electrons emitted in $W \to e\nu_e$ decays selected in the barrel: E/p is close to unity with a significant tail at large values due to Bremsstrahlung occurring in the inner detector. On the right-hand side, a good agreement between data and simulation is shown for the di-electron mass distribution of electrons coming from $J/\psi \to ee$ events: the width of this distribution is an estimate of the calorimeter electron energy resolution. The identification of isolated electrons also combines shower-shape variables such as lateral and longitudinal shower profiles. Three sets of cuts have been studied: they are called *loose*, *medium* and *tight* selection according to the signal efficiency and jet rejection they correspond to. Shower shape variables of the EM calorimeter middle layer and hadronic leakage variables are used in the *loose* selection. Variables from the EM calorimeter strip layer, track quality requirements and track-cluster matching are added to the *medium* selection. The *tight* selection adds particle identification using the TRT, discrimination against photon conversions via a b-layer hit requirement and information about reconstructed conversion vertices. The cuts are optimised in 10 bins of cluster η (defined by calorimeter geometry, detector acceptances and regions of increasing mate-

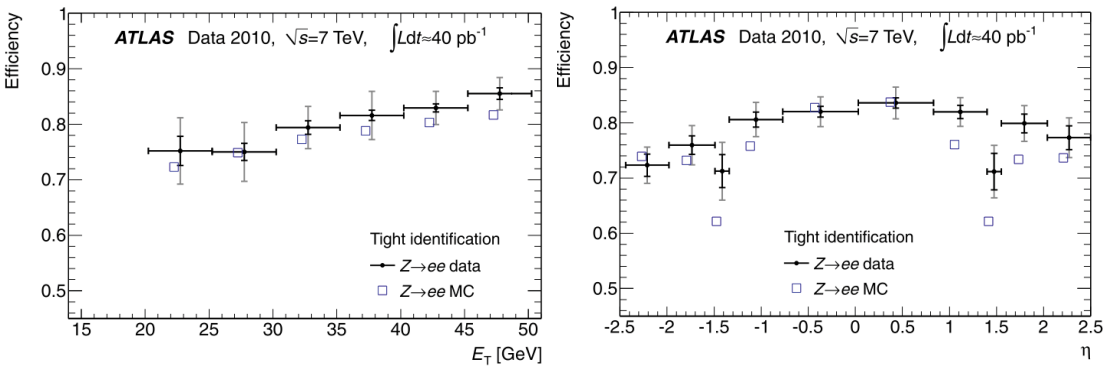

Figure 2.15: *Tight* electron identification efficiency measured in real and simulated $Z \to ee$ events as a function of the electron transverse energy (left) and pseudorapidity (right) [2].

rial in the inner detector) and 11 bins of cluster transverse energy from 5 GeV to above 80 GeV. The analysis presented here uses electrons passing the tight selection. The efficiencies of the tight electron identification cuts measured in $Z \to ee$ events are shown in Figure 2.15 as a function of the electron transverse energy and pseudorapidity.

2.3.3 Jet reconstruction and calibration

The jets used in this analysis are reconstructed with the anti-k$_t$ algorithm [52] with a distance parameter $R = 0.4$ using the *FastJet* software [51, 53]. The reconstruction of these jets is triggered by the reconstruction of topological clusters of calorimeter cells. Topological clusters (topoclusters) are designed to follow the shower development exploiting the fine segmentation of the ATLAS calorimeters: the clustering starts from seed cells whose signal-to-noise[5] ratio is above a threshold of S/N = 4. Neighboring cells that have a signal-to-noise ratio of at least S/N = 2 are included iteratively and finally all neighboring cells are included. All cells of the reconstructed topocluster are successively searched for local maxima of deposited energy and these maxima are then used as seed cells for a new iteration of the topological clustering which will split the original cluster into more topoclusters. A topocluster is defined to have an energy equal to the energy sum of all the included cells and a reconstructed direction as that of a vector with its origin in the origin of the ATLAS coordinate system and pointing to the energy-weighed topocluster barycenter. A more detailed description of the clustering algorithms in ATLAS can be found in [126].
Jets are reconstructed at the electromagnetic scale, which is the basic signal scale for the ATLAS calorimeters. It accounts correctly for the energy deposited in the calorimeter by electromagnetic showers. This energy scale is established using test-beam measurements for electrons in the barrel and endcap calorimeters. The fact that jets also contain hadrons make the calibration of the jet energy necessary. The hadronic jet energy scale is on average restored using data-derived corrections and calibration constants derived from the comparison of the reconstructed jet kinematics to the one of the corresponding truth level jet in Monte Carlo studies. In 2010 and 2011, ATLAS used a simple calibration scheme (called EM+JES) that applies jet-by-jet corrections as a function of the jet energy and pseudorapidity to jets reconstructed at the electromagnetic scale. This calibration scheme consists of three subsequent steps:

- the average additional energy due to in-time pile-up is subtracted from the energy measured in the calorimeters using correction constants extracted from in-situ measurements;
- the position of the jet is corrected such that the jet direction points to the primary vertex of the interaction instead of the geometrical center of ATLAS;
- the jet energy and position as reconstructed in the calorimeters are corrected using constants derived from the comparison of reconstructed jets with the corresponding truth jets in Monte Carlo.

[5] The noise includes the expected electronic noise and calorimeter activity due to pile-up events.

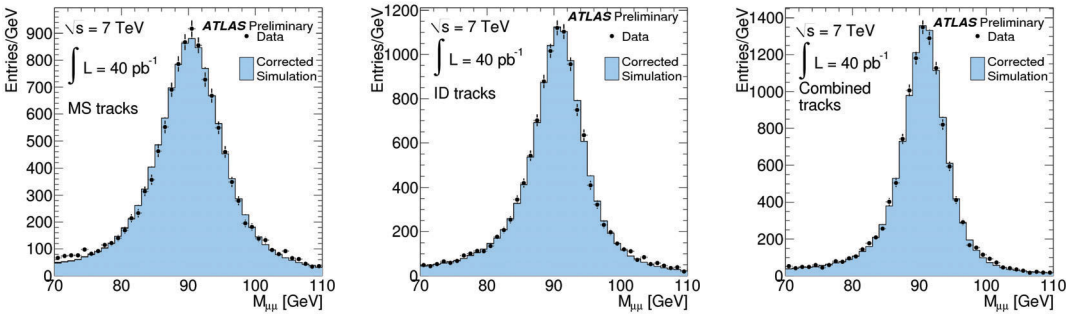

Figure 2.16: Di-muon invariant mass comparison in the Z boson mass range between collision data and simulation. The distribution is integrated over the full range in η. From left to right the MS, ID and combined measurements are shown [72].

The EM+JES calibration restores the jet energy scale within 2% for the full kinematic range [68].

2.3.4 Muon reconstruction

Muons are accurately measured by the inner detector and the muon spectrometer: the former provides the best measurements at low and intermediate momenta whereas the latter takes over above ~ 30 GeV. When these two measurements are combined we speak about *combined* muons. This analysis takes into account combined muons exclusively.
At the passage of a muon each MDT or CSC station starts an independent calculation of drift circles. These are then combined into straight lines called track segments. The search for segments is seeded by activity in the trigger chambers. Starting from the outer layer and moving inward, the track segments are combined into a stand-alone muon-spectrometer track candidate. The final stand-alone track-fitting procedure takes into account the geometrical description of the traversed material and the magnetic field inhomogeneities along the muon trajectory. The track is then extrapolated back to the interaction point and the momentum is corrected for the energy loss in the inner detector and in the calorimeters. The combination of the MS stand-alone track with an inner-detector track is performed in the region $|\eta| < 2.5$. This combination significantly improves the momentum resolution of the track and suppress the background from semi-leptonic decays of heavy flavor hadrons and pion or kaon decays in flight. Figure 2.16 shows the improvement of the track momentum resolution in the distribution of the di-muon invariant mass in the Z boson region for MS (left) and ID (middle) stand-alone tracks and for combined tracks (right).

2.3.5 Reconstruction of missing transverse energy

Neutrinos are inferred by a momentum imbalance after adding up all visible detector activity of a given event. The first step of missing transverse energy reconstruction is based on the energy of the calibrated calorimeter cells and on the reconstructed muons.

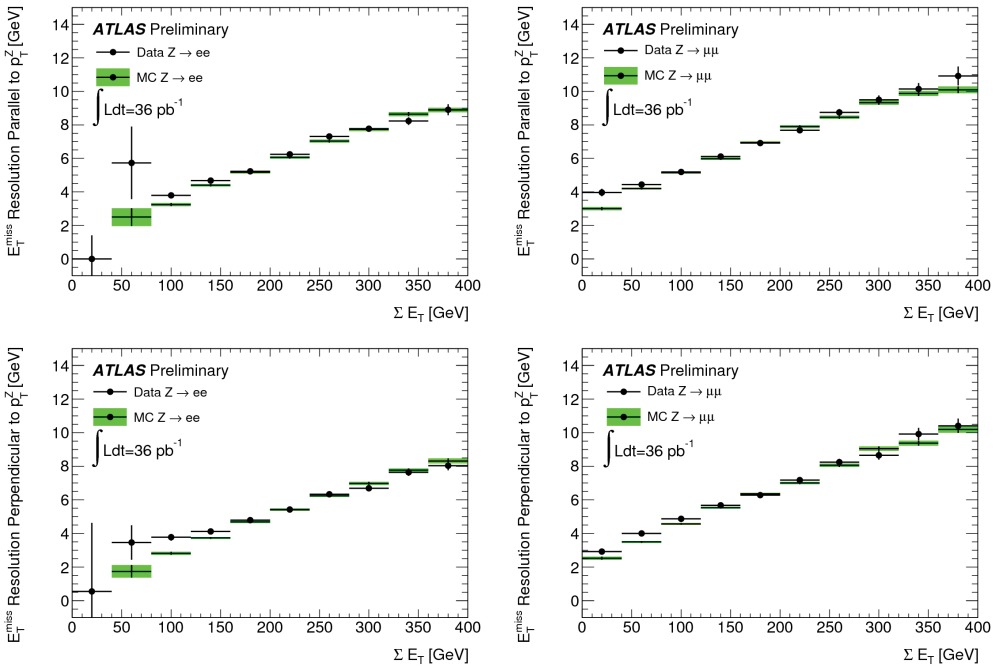

Figure 2.17: Resolution of E_T^{Miss} in $Z \to ee$ (left) and $Z \to \mu\mu$ (right) events projected along an axis parallel (top) and perpendicular (bottom) to the Z boson transverse momentum as a function of the total calorimeter transverse energy of the event [73].

To avoid double-counting of muon energy loss in the calorimeters, the muons are included using the stand-alone MS reconstruction but only good-quality muons with a matched track in the inner detector are considered. The missing transverse energy is then corrected for the energy lost in the calorimeter crack region. Finally, a refined calibration of the missing transverse energy is performed through association of fully calibrated calorimeter cells to the physics objects of the event: electrons, high-transverse-momentum jets and low-transverse-momentum (soft) jets. The ordering of these objects indicates the order of association of the cluster to the objects: if a cell belongs to more than one object only the first association is used. The E_T^{Miss} is calculated as:

$$E_{x,y}^{\text{Miss}} = E_{x,y}^{\text{Electrons}} + E_{x,y}^{\text{Jets}} + E_{x,y}^{\text{SoftJets}} + E_{x,y}^{\text{Muons}} + E_{x,y}^{\text{CellOut}} \tag{2.11}$$

$$E_T^{\text{Miss}} = \sqrt{(E_x^{\text{Miss}})^2 + \left(E_y^{\text{Miss}}\right)^2} \tag{2.12}$$

(which was already expressed in vectorial form in Equation 2.10). The cells which do not contribute to any reconstructed object but which survive an optimized noise cut are also calibrated and included in the calculation in the CellOut term. Figure 2.17 shows the resolution of the missing transverse energy measured in $Z \to ee$ (left) and $Z \to \mu\mu$ (right) events, for which no missing energy is expected. The quantity plotted is the resolution along an axis which is parallel (top) and perpendicular (bottom) to the transverse component of the Z boson momentum and it is parametrized in terms of the transverse calorimeter activity defined as:

$$\sum E_T = \sum_{i=1}^{N_{cell}} E_i \sin\theta_i \tag{2.13}$$

where E_i and θ_i are the energy and the polar angle of the cells associated to energy clusters.

3 Monte Carlo simulation

Monte Carlo (MC) simulations of physics processes are used in particle physics for several purposes: to extract a new signal from a background of SM processes, to make comparisons of theoretical predictions with data, to provide a realistic input for the design of an experiment, to design a reconstruction procedure or an event selection, etc. As previously mentioned, the property of factorization allows us to separate the treatment of a physics process into different regimes according to the scale of momentum transfer involved. The matrix elements of the hard subprocesses at hadron colliders are computable in perturbative QCD. However, the vast majority of collisions at the LHC are soft, leading to dissociation of beam particles and multi-particle production with low transverse momenta. These soft processes also need to be simulated but their non-perturbative nature means that we have to resort to models with tunable parameters to describe the data.
This chapter is dedicated to the description of the simulation of proton-proton collisions and of the MC samples used in this thesis. This overview is based on the description in Ref. [44]. At the end of this chapter the ATLAS simulation infrastructure is briefly described.

3.1 Modeling of proton-proton collisions

A reliable computer simulation of proton-proton collisions involving the hard process of interest also has to include the modeling of low-momentum scale subprocesses associated to it. As depicted in the diagram in Figure 3.1 for top-quark pairs, the hard process is

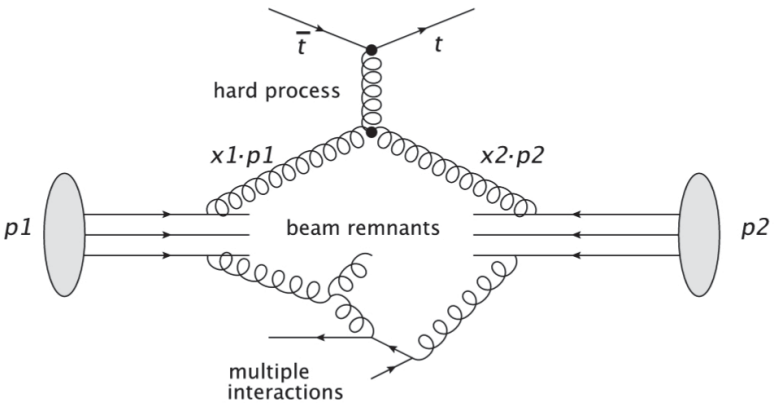

Figure 3.1: Phenomenology of $t\bar{t}$ production in proton-proton collisions.

the part of the event where large momentum transfer occurs and it determines the main characteristics of the event. The partons participating in the hard scattering are asymptotically free quanta and their interaction can be described by perturbation theory. The partonic content of the protons is described by the PDFs (see Section 1.2.1). Technically this is achieved by linking the generator of the MC simulation against software libraries containing information about the PDFs and their evolution.
Since the particles entering and leaving the hard process are partons, they can radiate gluons. These gluons can radiate other gluons or even produce quark-antiquark pairs, generating showers of outgoing partons. Partons on their way to the scattering process are expected to radiate giving rise to Initial State Radiation (ISR). Likewise, when the production of the final state partons is accompanied by gluon emission we speak about Final State Radiation (FSR) (see also Figure 3.2). Technically parton showers algorithms are formulated as forward evolution of the outgoing partons (FSR) or backward evolutions of incoming partons (ISR) downwards from the scale set by the hard process.
It is possible that in a given proton-proton collision more than one pair of partons may interact with each other thus producing additional partons which may contribute to the final state of the hard process and the associated parton showers. These *underlying events* occur predominantly at scales much lower than the scale of the hard process and hence they are also modeled as parton evolutions.
The beam remnants in Figure 3.1 are all that is left in the colliding protons after the partons participating in the hard scattering and underlying events are taken out. The beam remnants are color-connected to the hard scattering and the underlying event.
As the event evolves downwards in momentum scale, it ultimately reaches a scale at which QCD becomes strongly interacting. At this stage the perturbative evolution must be replaced by a non-perturbative hadronization model that describes the confinement of the system of colored partons into colorless hadrons. The hadrons produced in this hadronization phase are typically unstable resonances. Their decays into lighter particles long-lived enough to be detected also need to be simulated.
Finally, as previously mentioned, additional soft proton-proton collisions can occur. These pile-up events should be overlaid on top of the hard event. Additional pile-up comes from occasional interaction of the beams with gas in the beam pipe, from backgrounds due to the interaction of the beams with the collimators (beam halo) or from noise due to cavern background which is primarily made up of low-energy photons and neutrons generated from interactions in the cavern walls or in the detector shielding.
For the simulation of all these physics aspects the use of approximations cannot be avoided. To increase the quality of the agreement with the data, MC generators use tunable parameters with arbitrary but informed choices of their values. The cross-section of the stable final states obtained after the full MC simulation is expressed in terms of the various simulation stages by:

$$\sigma_{\text{final state}} = (\sigma_{\text{hard process}} \oplus \sigma_{\text{UE}}) \otimes \text{PS} \otimes \text{hadronization} \otimes \text{hadron decays} \; (\otimes\text{pileup}), \quad (3.1)$$

where σ_{UE} is the cross-section of the underlying event and PS stands for Parton Showers, i.e. initial and final state radiation.

3.2 Monte Carlo generators used in the analysis

3.2.1 Signal samples

Nominal sample

The generator used for the nominal signal samples is MC@NLO 3.41 [92]. This is a specialized generator for the production of the hard process which provides the implementation of the NLO matching scheme between matrix elements and parton showers. Cross sections and values of observables are accurate to the NLO level. The PDFs used, CTEQ66 [138], are at NLO accuracy. The simulation of all the secondary processes described in Section 3.1 is achieved by interfacing MC@NLO to the general purpose generator HERWIG 6.510 [75] and JIMMY[1] [47]. The $t\bar{t}$ cross section is normalized to the reference approximate NNLO prediction obtained with HATHOR [15]: $\sigma_{t\bar{t}} = 164.6$ pb for $m_t = 172.5$ GeV. The sample statistics available corresponds to ~ 15 fb^{-1}. The nominal samples are generated with a top mass $m_t = 172.5$ GeV. Other samples have been generated with different values of the top quark mass ranging from 140 GeV to 200 GeV. These samples are used in the extraction of the top quark mass from the measurement of the production cross section.

Samples for systematic studies

In order to assess the uncertainty stemming from the choice of the nominal generator, the MC@NLO signal is compared to the signal generated by POWHEG [91], which also produces final states at NLO accuracy. To isolate the effect on the hard process, POWHEG is interfaced, like MC@NLO, with HERWIG and JIMMY. POWHEG can also

[1]The CTEQ66 HERWIG and JIMMY AUET1 tune to the ATLAS data was used [65].

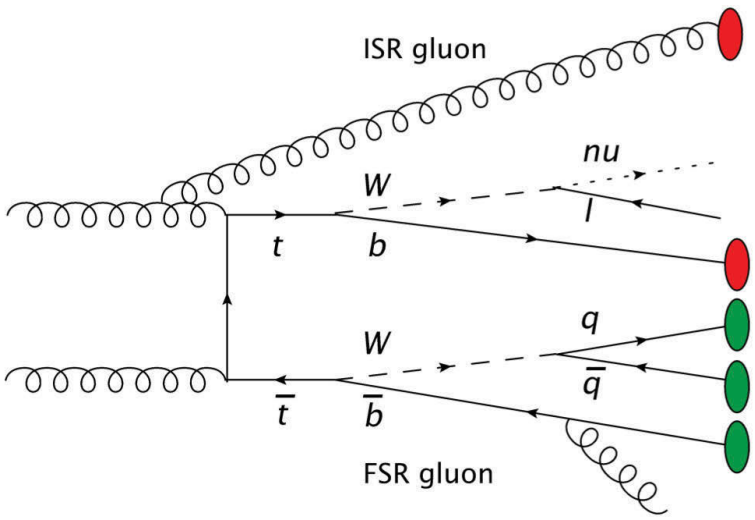

Figure 3.2: Initial and final state radiation in $t\bar{t}$ production.

Parameter	ISR ↓	ISR ↑	FSR ↓	FSR ↑
PARP(64)	4	0.25	1	1
PARP(67)	0.5	6	4	4
PARP(72) [GeV]	0.192	0.192	0.096	0.384
PARJ(82) [GeV]	1	1	2	0.5

Table 3.1: Parameter variation in PYTHIA for the assessment of the systematic uncertainty related to the modeling of initial al final state radiation.

be interfaced with the general purpose generator PYTHIA [151] thus enabling studies of the effect of using two different hadronization models.
For systematic studies of the initial and final state radiation a number of samples has been generated using AcerMC [111], specialized in the production of the hard process at LO accuracy, interfaced with PYTHIA. In four samples the ISR and FSR parameters are varied individually within experimentally not excluded values to increase and decrease the activity related to initial and final state radiation.
The relevant initial state radiation parameter in PYTHIA is PARP(67) which multiplies the Q^2 scale of the hard scattering to define the maximum parton virtuality allowed in Q^2-ordered space-like showers. Hence, the effect of changing the value of this parameter is equivalent to changing the hard process scale, which is in general not unambiguously determined by theoretical considerations. The default value of PARP(67) is based on Tevatron studies. A similar parameter (PARP(71)) exists for the final state radiation. However, the variation of this parameter has no effect on $t\bar{t}$ observables and it is not considered in $t\bar{t}$ systematic studies.
The PYTHIA parameters PARP(61) and PARP(72) set the value of Λ_{QCD} for the parton shower evolution of initial and final state radiation. A variation of these parameters affects the evolution of the strong coupling constant α_S and changes the parton shower radiation spectrum. In case of initial state radiation, the parameter PARP(64) multiplies the value of Q^2 in the definition of α_S. The effect of changing PARP(61) by a factor k is proportional to changing PARP(64) by a factor $1/k^2$. The systematic studies carried out for this analysis include variations of PARP(64) and PARP(72).
Finally, the last parameter which has a relevant impact on $t\bar{t}$ production is PARJ(82) which represents the scale at which the perturbative final-state parton-shower evolution terminates and the non-perturbative model takes over.
The default values of these parameters are: PARP(64)=1, PARP(67)=4,
PARP(72)=0.192 GeV and PARJ(82)= 1 GeV. The MC samples used in this analysis to assess the systematic uncertainty related to initial and final state radiation were created with the variations listed in Table 3.1.

3.2.2 Background samples

The production of a W boson in association with jets represents the major source of background for $t\bar{t}$ analyses in the single-lepton channel. This background is simulated

with ALPGEN [131] interfaced to HERWIG and JIMMY. The samples with a light-flavor jet content and those with a heavy-flavor jet content are produced separately with ALPGEN. In the W+light jets samples, the jets arising from the matrix element come from gluons and massless u, d, s and c quarks whereas all the b-quark jets originate from low transverse momentum b quarks from the parton showers. In the samples with jets from heavy flavor, massive b quarks originate from the matrix element. In addition, $W + c(\bar{c})$+jets and $W + c\bar{c}$+jets samples with massive c quarks have been generated separately.
The production of a Z boson in association with jets represents a minor source of background for $t\bar{t}$ analyses in the semi-leptonic channel since leptonic decays $Z \to \ell\ell$ contain two charged leptons while the standard $t\bar{t}$ selection (Section 4.2) requires exactly one. Like W+jets, Z+jets is produced with ALPGEN and HERWIG. These samples also contain the Drell-Yan contribution from $\gamma^* \to \ell\ell$ and the Z/γ^* interference. The invariant mass of the lepton pair lies in the mass range $40 < M(\ell\ell) < 2000$ GeV. For both W+light jets and Z+jets production, the samples are split according to the different number of partons in the final state: there are 5 samples with an exclusive number of partons that goes from 0 to 4 and an inclusive sample with more than 4 partons. The $W + b\bar{b}$+jets and the $W + c\bar{c}$ are split into up to 3 final state partons and the $W + c(\bar{c})$+jets samples up to 4. Since there is no attempt in ALPGEN to match explicitly the matrix-element c and b quarks and the jets from the parton showers, the same heavy flavor final state may end up in more than one sample. For example, an event with a W, a c and a u quark may be generated in both the light jets sample with two final state partons and the $W + c$+jets sample with one additional parton. The overlapping events have been identified and discarded in the analysis using a dedicated tool centrally distributed by the ATLAS collaboration.
The simultaneous production of two vector bosons (WW, ZZ and WZ) has been simulated with HERWIG and included in the analysis as a source of background. Both weak bosons can decay leptonically and hadronically leading to configurations with a charged lepton, missing transverse energy and jets which fake the signature of the $t\bar{t}$ signal. In the simulation, the W decays inclusively but for the samples used a generator filter was applied to select only events with at least one electron or muon with a minimum transverse momentum of 10 GeV and $|\eta| < 2.8$. The cross sections for single boson and di-boson production are normalized to NNLO and NLO predictions respectively [46].
Finally, the last source of background that is taken from simulation is single top production which is produced with MC@NLO+HERWIG/ JIMMY and using the MSTW 2008 NNLO PDFs. In the nominal samples the top quark has a mass of 172.5 GeV but samples with the same mass variations as the $t\bar{t}$ samples are available. The reference cross sections used are approximate NNLO calculations which are equal to 64.6 pb [115], 4.6 pb [113] and 14.7 pb [114] for the t- , s- and Wt- production channels respectively.

3.3 The ATLAS simulation system

Athena is the name of the common framework for event processing in ATLAS. The entire ATLAS simulation system is built within Athena as a concatenation of many distinct processing stages comprising the fundamental event generation, the interaction of the final state particles with the detector and the digitization of the physics quantities with the production of the final output equivalent to that coming from the real detector.
The Athena framework is interfaced with more than 40 MC generators. The ones used for top-quark physics have been discussed in the previous section. The second stage of simulation processing is the propagation of the products of the interaction through the detector layers starting from the inner tracker to the muon system. The simulation of these interaction is performed within Athena using Geant 4 [12]. Before being handed over to Geant 4, the generated events are smeared, rotated and boosted according to a beam spot parameterization taken from the ATLAS condition database providing a realistic distribution of interaction points. The detector description is taken from a geometry database that is common to simulation and reconstruction applications. The geometry database includes variants of the ATLAS detector such as extra material and sub-detector misalignments that are regularly updated to include improved descriptions in response to data/MC comparison.
The final stage of simulation is the digitization. The ATLAS digitization software transforms the hits into detector responses taking care of the peculiarities of each sub-detector like e.g. electronic noise and channel-dependent variations. Dead channels and noise rate are read from a database to reproduce run-dependent conditions. This is also the stage at which the simulation of the signal events is overlaid with pile-up events, cavern background and cosmic rays. The simulation of these last two phenomena require more specialized treatment and dedicated generation software.
Simulated events are reconstructed with the same algorithms used for the data event reconstruction. The data and MC samples used in this analysis are constructed with Athena release 16.6 which was used in the data taking of the first half of the year 2011. The official data format of Athena is the AOD (Analysis Object Data). Each AOD stores thousands of variables and can reach the size of several gigabytes. Since a physics analysis generally needs to use hundreds of AODs, many ATLAS Working Groups have decided to conveniently derive smaller samples (D3PD) containing only the relevant variables of filtered events passing a basic selection (e.g. at least one lepton with a minimum transverse momentum threshold). The D3PDs used in this analysis are centrally provided by the ATLAS Top Working Group and analyzed with a software framework called SFrame [2].

Monte Carlo samples are usually produced before or during a data-taking period. When the simulated conditions do not reproduce correctly the data it is necessary to correct the MC events at the analysis level. An example of two such cases which are relevant for the analysis presented here are described below:

[2] http://sourceforge.net/projects/sframe

Pile-up re-weighting

The average number of interactions per bunch crossing is a parameter of the simulation. The value chosen for the 2010 production campaign was found to be too small compared to the real average number of interactions occurring at the LHC in early 2011 causing an evident data-MC discrepancy. Furthermore, in 2011 the proton bunch spacing was decreased from 75 ns to 50 ns producing also an out-of-time component of pile-up coming from overlapping signals in the detector from neighboring bunch crossings. A common tool provided by the ATLAS collaboration has been used in this analysis to correct, in a form of event-by-event weight, the simulation according to the pile-up conditions observed in data.

LAr Hole

On April 30th 2011 a hardware failure in the acquisition system affected the electromagnetic calorimeter creating a dead region. The failure occurred after the production of the MC samples and hence had to be reproduced in the simulation at the analysis level. First, all the events containing jets with a minimum momentum of 20 GeV close to the dead region are discarded in data and in MC. In addition, all the electrons intersecting the hole in the electromagnetic calorimeter are removed in MC and the missing transverse energy is corrected accordingly. These corrections have been applied to a fraction of simulated events equal to the fraction of data events affected.

4 Event Selection and background estimation

As described in Section 2.3, during the reconstruction of tracks, particles and jets some selections are performed to suppress fake objects generated by the reconstruction algorithms. Usually, the objects that enter a physics analysis must undergo additional selection to maximize the contribution from the process of interest and reduce background contamination. The efficiency of the reconstruction and of the subsequent selection of the leptons produced in top-quark decays are measured in data and in MC with a technique called "Tag and Probe". Generally, simulation mis-modeling or unaccounted detector effects cause the efficiency measured in MC to differ from the real one measured in data. Hence the acceptance of the MC samples used in this analysis is corrected using scale factors defined as the ratio between the data and the MC efficiency.
Section 4.1 describes the selection of the physics objects produced in the decay of top-quark pairs and the calculation of the scale factors for the correction of the MC acceptance. The set of cuts to select $t\bar{t}$ events is described in Section 4.2. Section 4.3 describes other physics processes that have a similar experimental signature and thus can pass the selection designed for $t\bar{t}$ pairs. These processes fake the signal of interest and hence are collectively called *background*.

4.1 Object selection

4.1.1 The "Tag and Probe" method

Using the "Tag and Probe" method it is possible to measure and compare the efficiency of a given selection both in simulation and in real data. The method relies on the use of di-object final states: for the calculation of lepton efficiencies $Z \to \ell\ell$ events are the most common choice because the Z boson production is a well-understood process with a clean signature and a relatively high production rate. The main idea of the Tag and Probe method is to tag the object for which a certain condition is realized and to probe the same condition on the second object. Hence, the Tag and Probe efficiency can be defined as the number of events $N_{\text{Tag\&Probe}}$ in which the condition is realized for both objects normalized to the total number of events N_{Tag} in which the condition is satisfied for the tag object:

$$\epsilon_{\text{Tag\&Probe}} = \frac{N_{\text{Tag\&Probe}}}{N_{\text{Tag}}} \tag{4.1}$$

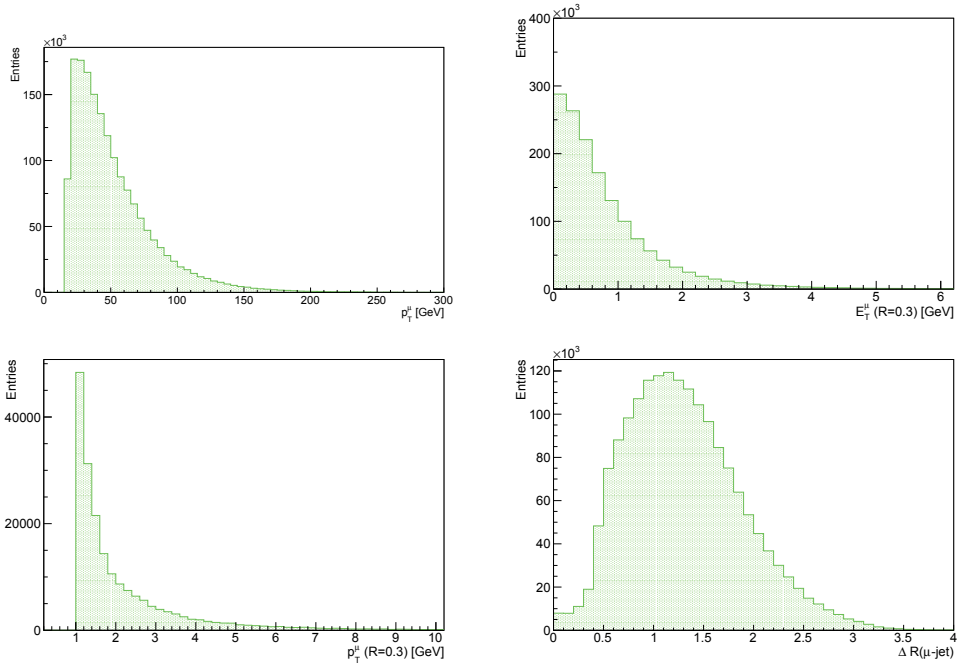

Figure 4.1: Muon kinematics in selected $t\bar{t}$ events. The cut on the displayed variable is not applied. The thresholds in the dafault selection are: muon transverse momentum $p_T^\mu > 20$ GeV (top left), calorimeter energy deposit around the muon combined track $E_T^\mu(R = 0.3) < 4$ GeV (top right), sum of the transverse momenta of ID tracks around the muon combined track $p_T^\mu(R = 0.3) < 4$ GeV (bottom left) and distance ΔR between muon and closest jet with $p_T^{\text{jet}} > 20$ GeV greater than 0.4 (bottom right).

The scale factors are defined as:

$$SF = \frac{\epsilon^{\text{data}}_{\text{Tag\&Probe}}}{\epsilon^{\text{MC}}_{\text{Tag\&Probe}}} \tag{4.2}$$

and they are often parameterized as a function of kinematic variables over whose range the ratio in Equation 4.2 is not constant like e.g. the probe lepton p_T or η. The SF are provided in the form of event weights to correct the acceptance of the simulated events. The $Z \to \ell\ell$ events considered for the calculation of the SF are selected with a cut on the invariant mass of the lepton pair that is usually varied for the evaluation of the systematic uncertainties of the scale factors. The selection of the leptons varies according to which efficiency is under study.

4.1.2 Muons

Selection

The reconstruction of muons with the ATLAS detector was described in Section 2.3.4. As mentioned there, only combined (CB) muons, i.e. muons reconstructed from a combination of individual measurements from the ID and the MS, are considered in this analysis because they represent the muon candidates with the highest purity.
All the $t\bar{t}$ candidates decaying in the muon+jets channel are selected with a chain of muon triggers that require at least one reconstructed muon with:

- a LVL1 trigger accept with a minimum transverse momentum of 10 GeV;
- a LVL2 and EF trigger accept with a minimum transverse momentum of 18 GeV.

This trigger chain is called "EF_mu18". To inspect whether a reconstructed muon has passed a certain trigger chain, it is checked that it overlaps with a trigger muon which passes the same chain. The maximum distance required to claim an overlap and hence a trigger match for muons produced in top quark decays has a nominal value of $R = 0.15$ as this is the minimum angular distance for which it is possible to discern two separate objects in the detector.
The offline muon selection that follows is aimed at rejecting muons not coming from the process of interest: $t \to W \to \mu\nu$. First of all, some requirements are needed for the ID segment of the track associated to a combined muon:

- the ID track must have at least one hit in the innermost layer of the pixel detector. If the muon has traversed an area which is known to be not functioning or not instrumented this requirement is dropped. On top of this, the total number of pixel hits plus the total number of crossed dead pixel sensors must be greater than one,
- the number of SCT hits plus the number of crossed dead SCT sensors must not be smaller than six,
- a maximum number of two "holes" (i.e. expected but missing hits because the particle has traversed not functioning or not instrumented areas) in the pixel and SCT detectors is allowed,
- in the pseudorapidity region $\eta < 1.9$, the number N of TRT hits plus the number of outliers on the muon track (defined in Section 2.3.1) must be greater than five, with the additional requirement that 90% of N comes from hits and not outliers,
- in the pseudorapidity region $\eta \geq 1.9$, the previous requirement is applied only if $N > 5$.

The reconstructed combined muon with a good-quality ID track is used in the analysis only if it has, on top of the trigger requirement, a transverse momentum of at least 20 GeV and $|\eta| < 2.5$. To match the momentum scale and resolution observed in data,

which are measured from the peak position and width of the di-muon invariant mass distributions of real $Z \to \mu\mu$ decays, the simulated muon momentum is scaled and smeared before any selection is applied. To ensure isolation, the energy deposition in the calorimeters and the sum of track transverse momenta measured in cones of radius $R = 0.3$ around the muon track are each required to be less than 4 GeV. Additionally, muons are required to have a distance ΔR greater than 0.4 from any jet with $p_T > 20$ GeV. These isolation cuts have been designed to suppress muons coming from decays in flight of hadrons which in general have additional calorimeter activity in their vicinity. Some muon kinematical variables for selected $t\bar{t}$ events are displayed in Figure 4.1. All the cuts described in this section and in Section 4.2 are applied except the one concerning the variable being shown. The reduced acceptance for low values of the muon transverse momentum comes from the muon trigger requirement.

Reconstruction efficiency and scale factors

The reconstruction efficiency for CB muons is the product of the muon reconstruction efficiency of the ID, the reconstruction efficiency of the MS and the matching efficiency between the ID and the MS measurements. The individual reconstruction efficiencies are measured in data and in MC with the Tag and Probe method using Z boson decays into muons: one decay muon is required to be reconstructed in both systems whereas the other muon is identified by just one of the systems in order to probe the efficiency of the other. The scale factors for CB muon reconstruction in ATLAS are calculated by a dedicated group of experts using 200 pb^{-1} of 2011 data and distributed centrally. They have been found to be roughly consistent with unity throughout the η range with very small uncertainties which are taken into account in the evaluation of the systematic uncertainty of the $t\bar{t}$ cross section.

Trigger efficiency and scale factors

The efficiency of the EF_mu18 trigger chain is measured with the Tag and Probe method using $Z \to \mu\mu$ events. The condition to be realized in case of trigger efficiencies is the match of a reconstructed muon with a trigger object from the muon triggers. The trigger efficiency is thus defined as the ratio of events for which both the tag and probe muon have a trigger match to the total number of events for which the tag muon has a trigger match.

$$\epsilon_{EF\_mu18} = \frac{\mathrm{N}^{\mathrm{EF\_mu18}}_{\mathrm{Tag\&Probe}}}{\mathrm{N}^{\mathrm{EF\_mu18}}_{\mathrm{Tag}}} \tag{4.3}$$

Except for the trigger requirement that is being probed, the two muons are required to pass all the selections previously described. This ensures that the efficiency is evaluated on the same kind of muons used in the analysis. Furthermore they are required to have opposite electric charge and to reconstruct an invariant mass that lies in the mass window:

$$|M_{\mu_{Tag}\mu_{Probe}} - M(Z)| \leq 12 \text{ GeV} \tag{4.4}$$

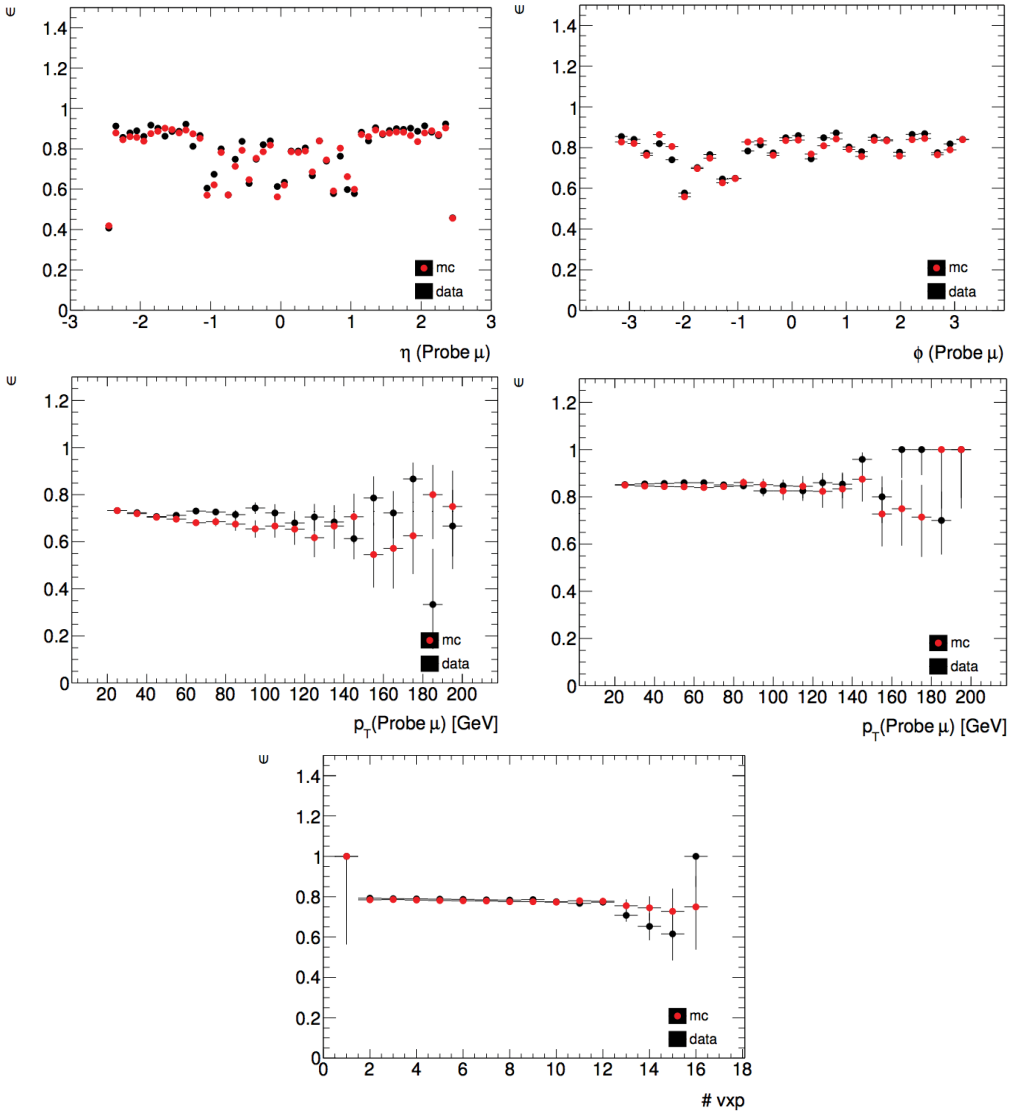

Figure 4.2: Comparison of the Tag-and-Probe EF_mu18 trigger efficiencies for data and MC as a function of the probe muon η, ϕ, p_T and number of primary vertices (pile-up). The p_T dependence is studied separately in the barrel (middle left) and end-caps (middle right) [87].

where $M(Z)$ is the world average value of the Z boson mass [34].
The data sample used for the measurement of the data trigger efficiency is the same used in the extraction of the cross section and corresponds to 700 pb^{-1}. The corresponding $Z \to \mu\mu$ MC samples were described in Section 3.2.2 and correspond to about 50 fb^{-1}.
The trigger efficiency is studied as a function of a number of kinematic and isolation variables. Figure 4.2 shows the Tag and Probe efficiencies of the EF_mu18 trigger as a function of the probe muon p_T, η, ϕ, distance to the closest jet and number of primary vertices (pile-up). From the distribution of the efficiency as a function of $|\eta|$, it is clearly visible that the efficiency is lower in the barrel region ($|\eta| \leq 1.05$) than in the end-caps. This is due to the reduced geometrical coverage of the RPC detectors close to the feet of the toroidal magnet support structure, also visible at $\phi \sim -2$ and -1.
The SFs are divided in η and ϕ bins according to the small disagreements observed in the data and Monte Carlo efficiencies. Furthermore, a dependence of the SFs on the muon transverse momentum is observed in the barrel. This stems from a misconfiguration of the LVL2 muon trigger that caused an underestimation of the trigger efficiency for Monte Carlo muons with $p_T > 40$ GeV. The effect, which is also visible in the middle-left plot in Figure 4.2, was found to increase linearly with the muon transverse momentum and to cause a 30% muon loss at $p_T = 500$ GeV. Since the p_T range of muons from Z decays is limited (see the plots in the middle of Figure 4.2), the Tag and Probe technique can not be used to estimate the behavior of the Monte Carlo efficiencies above a p_T threshold of about 150 GeV. The residual effect of this misconfiguration in the p_T range below 150 GeV is accounted for by further dividing the trigger SFs in three p_T bins: $20 < p_T < 60$ GeV, $60 < p_T < 120$ GeV and $120 < p_T < 150$ GeV. For the analysis presented in this work it was chosen to discard the small number of events in which the muon that fires the trigger has a transverse momentum greater than 150 GeV and to apply the trigger SFs regularly to each event according to the muon η, ϕ and p_T. The fraction of discarded events is smaller than 1%, as Figure 4.1 shows.
The systematic uncertainty of the muon trigger SFs stems from the invariant mass cut around the Z boson mass, from the ΔR value chosen for the muon trigger match and from the isolation required for the tag muon. These effects were studied and the shift from the nominal values were added in quadrature to the statistical uncertainty to provide a total uncertainty on the muon trigger SFs, which was then taken into account for the evaluation of the systematic uncertainty of the $t\bar{t}$ cross section. The removal of the isolation requirement for the tag muon has been found to produce the largest shift from the nominal values of the trigger scale factors.

Identification efficiency and scale factors

The muon identification efficiency measured with the Tag and Probe technique is defined as the number of combined reconstructed probe muons passing the standard muon selection previously described divided by the total number of combined reconstructed probe muons:

$$\epsilon_{\text{Id}} = \frac{N_{\text{Top muons}}}{N_{\text{combined muons}}}. \tag{4.5}$$

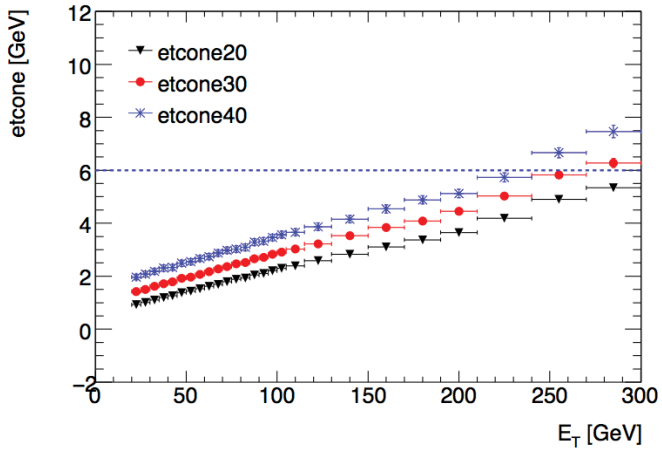

Figure 4.3: *EtCone20* distribution for the electrons produced in $t\bar{t}$ decays. Also shown the distributions for *EtCone30* and *EtCone40* defined as the energy deposited in a cone centered on the electron axis and with a radius $\Delta R = 0.3$ and 0.4 respectively [61].

As in the case of the trigger, the data efficiency is evaluated on the same dataset used in the cross-section analysis. For the efficiency in the simulation, the same MC samples used to measure the trigger scale factors are used. The identification scale factors have not shown a significant dependence on any kinematic or isolation variable. The offline identification scale factor used in this analysis is centrally provided [87] and found to be $\mathrm{SF_{Id}} = 1.0008 \pm 0.0003\ (\mathrm{stat}) \pm 0.0003\ (\mathrm{syst})$.

4.1.3 Electrons

Selection

All the electrons used in the cross-section analysis are required to pass a trigger chain called "EF_e20_medium" which requires an electron candidate passing the medium identification cuts (see Section 2.3.2) and having at the EF level a transverse cluster energy $E_T > 20$ GeV. The trigger match is performed, as for the muons, by requiring a maximum distance $\Delta R = 0.15$ between the reconstructed electron and the trigger object. All the triggered electrons are required to pass the *tight* selection which has an overall efficiency of about 75% (see Figure 2.15) and includes a well reconstructed ID track associated to the electromagnetic cluster.
Three types of problems with the EM calorimeter can arise during data taking and affect the quality of the reconstructed energy of an electron object. These are:

- some cells are not read out because they are connected to non-functioning read-out hardware: if part of the electron cluster falls in a dead region of the first or second calorimeter layer, the electron is rejected;
- some sectors have zero voltage: clusters falling into dead high-voltage regions are

rejected;

- some isolated cells produce a high noise signal or no signal at all. These cells are masked during reconstruction and their energy is set to the average energy of the neighboring cells. An electron is rejected if one of the cells in the core of its cluster is masked.

All these corrections are applied at the analysis level. The loss of electron acceptance due to these quality requirements is around 6%.
Only electrons associated to clusters with a transverse energy greater than 25 GeV are considered in the analysis because this is where the plateau region[1] of the electron trigger efficiency starts. The transverse energy of an electromagnetic cluster is defined as a function of the calorimeter cluster energy and the direction of the track pointing to it:

$$E_{\mathrm{T,cluster}} = \frac{E_{\mathrm{cluster}}}{\cosh\left(\eta_{\mathrm{track}}\right)}. \tag{4.6}$$

This variable is shown for selected $t\bar{t}$ events on the left-hand side of Figure 4.4. The cut at 25 GeV is not applied and, as in the case of the muons, the lower acceptance at small E_T values is due to the trigger requirement. The electron clusters are also required to be within $|\eta_{\mathrm{cluster}}| < 2.47$ with the exclusion of the calorimeter transition region $1.37 < |\eta_{\mathrm{custer}}| < 1.52$.
It is expected that electrons produced in the decay chain $t \to W \to e$ are isolated from jet activity, unless they accidentally overlap with one of the jets of the event. The main background sources for high-momentum, isolated electrons are the electrons produced in the decay of heavy flavors and in the conversion of photons or fake signatures generated by hadrons. The suppression of these backgrounds is possible by requiring little activity, i.e. small energy deposits, in the vicinity of the electromagnetic cluster. The technical requirement is that the energy deposited in a cone centered around the electron axis and with a radius $\Delta R = 0.2$ be smaller than 3.5 GeV once the energy associated to the electron itself is subtracted. The variable containing this energy deposit around the cluster, called *EtCone20*, was observed to increase with the transverse energy of the cluster as a consequence of the increased bremsstrahlung and leakage from the shower lateral spread, see Figure 4.3. Therefore, this variable is now corrected for this effect and for the additional contribution due to pile-up events before the cut is applied; the threshold value set at 3.5 GeV ensures a cut efficiency of about 96%. On the right hand side of Figure 4.4 the corrected variable is shown before the cut for selected $t\bar{t}$ events.

Trigger, reconstruction, identification and isolation efficiency and scale factors

The efficiencies of the electron trigger, reconstruction and identification used in the analysis are measured by a dedicated group using $Z \to ee$ and $W \to e\nu$ events and distributed centrally in ATLAS [87]. The trigger scale factors are provided in 18 η_{cluster}

[1] When the efficiency of a trigger which bases its decision on the value of a given kinematic variable is parameterized as a function of this variable, the region of constant maximum efficiency beyond the threshold value is called *plateau*.

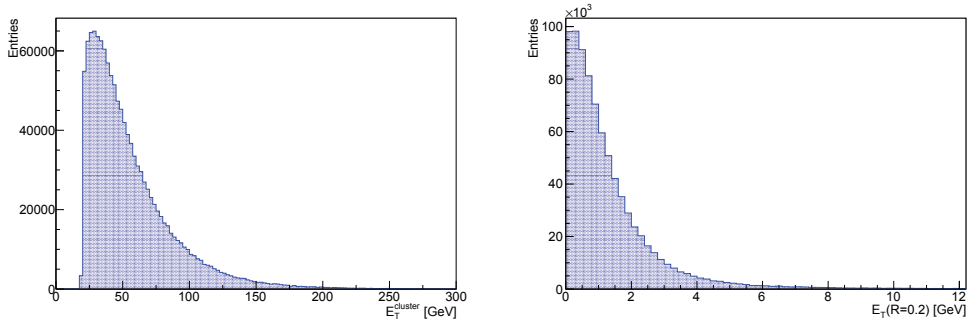

Figure 4.4: Distribution of electron cluster transverse energy (left) and *EtCone20* (right) for selected $t\bar{t}$ events. The cut on the displayed variable is not applied. The thresholds in the default selection are: cluster transverse energy $E_T > 25$ GeV and calorimeter transverse energy deposit around electron cluster $E_T(R = 0.2) < 3.5$ GeV.

bins from –2.47 to +2.47 and integrated over $E_{\mathrm{T,cluster}}$. In the region $|\eta_{\mathrm{cluster}}| < 1.37$ they are all very close to 1, whereas for $|\eta_{\mathrm{cluster}}| > 1.37$ they drop gradually to about 0.97.
The electron reconstruction scale factors, including the track requirement, are measured for $E_{\mathrm{T,cluster}} > 15$ GeV in 3 $|\eta_{\mathrm{cluster}}|$ bins. They are also consistent with 1 except in the region $|\eta_{\mathrm{cluster}}| > 2.37$ where the scale factor peaks at 0.97.
The tight identification scale factors are provided in 18 $|\eta_{\mathrm{cluster}}|$ bins from –2.47 to +2.47 and, due to a significant $E_{\mathrm{T,cluster}}$-dependence, in 5 $E_{\mathrm{T,cluster}}$ bins. When measuring versus one variable the scale factors are integrated over the other so that they can be treated as uncorrelated. The ratio of the $E_{\mathrm{T,cluster}}$-dependent scale factors to the average scale factors is used to define $E_{\mathrm{T,cluster}}$-dependent corrections to be applied in addition to the η_{cluster}-dependent scale factors.
The efficiency and scale factors of the additional isolation cut are measured using $Z \to ee$ decays. The Tag and Probe isolation efficiency is defined as the number of electron probes that pass the *tight* selection and the isolation cut normalized to the number of electron probes that pass the tight selection:

$$\epsilon_{\mathrm{iso}} = \frac{\mathrm{N}_{tight+\mathrm{iso}}}{\mathrm{N}_{tight}}. \tag{4.7}$$

An additional systematic uncertainty of 2% is applied to the data measurement to cover possible unmeasured data-MC discrepancy introduced by this cut and propagated to the uncertainty on the scale factors.

Electron energy scale and resolution

The electron energy scale in data was determined by constraining the peak position of the di-electron invariant mass distribution of $Z \to ee$ events [13]. An offset, which is less than 2% in the range $|\eta_{\mathrm{cluster}}| < 2.5$, was observed and hence a correction for the

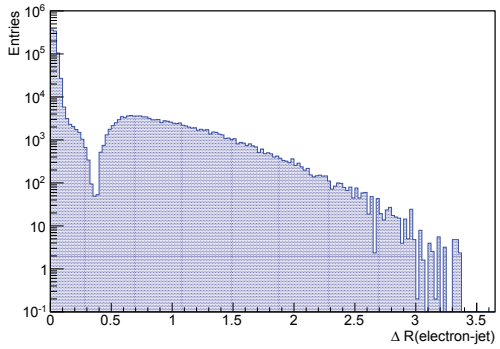

Figure 4.5: Distance between the electron and the closest jet in selected $t\bar{t}$ events before the jet selection described in Section 4.1.4. The other selection cuts described in Section 4.1.3 and 4.2 are applied. Jets for which $\Delta R < 0.2$ are likely to be fake objects reconstructed from the electron energy cluster and are therefore removed.

electron energy scale is applied to all the electrons in data according to their η_{cluster} before the standard selection previously described. The systematic uncertainty affecting the correction factors are dominated by uncertainties from the detector material and the energy scale of the first layer of the electromagnetic calorimeter.
At the same time, the shape of the $Z \to ee$ invariant mass distribution is not reproduced well by the MC simulation. Consequently the energy of all the MC electrons is smeared. The systematic uncertainties stemming from scaling and smearing the electron energy are propagated to the $t\bar{t}$ cross section. Both electron energy smearing and scaling factors as well as their uncertainties are centrally provided in ATLAS.

4.1.4 Jets

As described in Section 2.3.3, jets are observed as groups of topologically related energy depositions in the calorimeters with a number of ID tracks associated to them. The first step is to distinguish the jets produced in proton-proton collisions from background jets not originating from hard scattering events. The main backgrounds are:

- beam-gas events, in which protons of the beam collide with the residual gas within the beam pipe
- beam-halo events, caused for example by interactions in the collimators in the beam line placed outside the ATLAS detector
- cosmic rays
- large calorimeter noise.

Two types of calorimeter noise are addressed. The first one comes from sporadic noise bursts in the hadronic end-cap calorimeter, where noisy cells contribute almost all of the jet energy. Jets reconstructed from these problematic cells are characterized by a

large fraction of energy in the hadronic end-cap calorimeter with a large energy fraction from cells with poor signal shape quality, obtained by comparing the measured pulse to the expected pulse shape. Due to the capacitive coupling between channels, the neighboring cells have an apparent negative energy. The second type of noise is rare coherent noise in the electromagnetic calorimeter. Similarly, fake jets arising from this source are characterized by a large electromagnetic energy fraction and a large fraction of cells with poor signal shape quality.
Cosmic rays or non-collision background can induce events in which the jets candidates are not in time with the beam collision. A cut on the jet time, defined with respect to the event time recorded by the trigger, is applied to reject these backgrounds. Furthermore, a cut on the electromagnetic energy fraction of the jet is applied to make sure that the jet deposited some energy in the electromagnetic calorimeter, as it is expected for any jet originating from the interaction point. Since the charged particles of jets within the acceptance of the inner detector are expected to be tracked, this cut is applied together with a cut on the scalar sum of the p_{T} of the tracks associated to the jet normalized to the jet p_{T}. Lastly, a cut on the maximum energy fraction in any single calorimeter layer is applied to further reject non-collision background.
Events containing jets which fail these quality criteria are discarded only in data because most of the variables needed are not well modeled in the MC simulation. This selection has an efficiency above 99%. Some energy clusters in the calorimeters are reconstructed as an electron as well as a jet. To avoid duplicates in the analysis, the jet closest to a selected electron is always removed if these objects have overlapping axes ($\Delta R < 0.2$). This cut is applied before any quality selection for the jets. The distance ΔR between selected electrons and the closest jet in selected $t\bar{t}$ events is shown in Figure 4.5 before the overlap removal.
As a last step, the jets of the events which pass all the selections described in this section are required to have a minimum transverse momentum of 25 GeV and $|\eta| < 2.5$.

4.1.5 $\mathbf{E}_T^{Miss}$

The reconstruction of the missing transverse energy was described in Section 2.3.5. The physics objects that enter the calculation in Equation 2.11 are consistent with the object definitions described in the previous sections. The electron term satisfies the *tight* selection with $\mathrm{p}_T > 10$ GeV. The jets used are reconstructed with the anti-k_t algorithm and a distance parameter R = 0.4: clusters associated with jets with a $\mathrm{p}_T > 20$ GeV are corrected to the EM+JES scale, while clusters associated with soft jets ($7\,\mathrm{GeV} < p_T < 20\,\mathrm{GeV}$) are included at the electromagnetic scale. The muon term is determined from the p_T of muons in the full acceptance range of the muon spectrometer, $|\eta| < 2.7$. For $|\eta| < 2.5$, all combined muons are used.
The missing energy is corrected at the analysis level for the leptons' energy and momentum scaling and smearing with a common tool provided by the ATLAS collaboration.

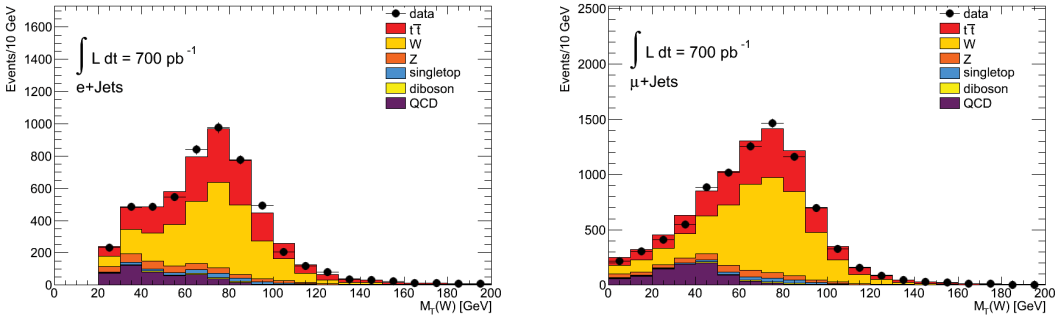

Figure 4.6: The W transverse mass distribution in the electron (left) and muon (right) channel with four selected jets in the final state.

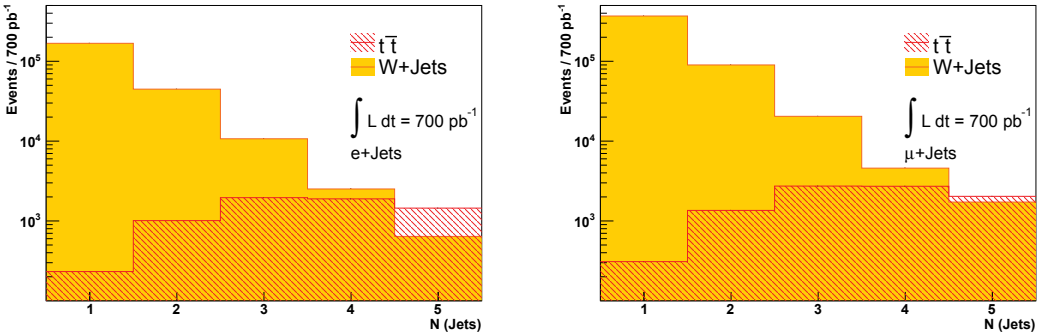

Figure 4.7: Expected number of selected events in an integrated luminosity of 700 pb^{-1} as a function of jet multiplicity for the $t\bar{t}$ signal and the main background process, W+Jets. The last jet bin is inclusive.

4.2 Top pair event selection

The $t\bar{t}$ candidate events that contribute to the cross-section analysis are selected with a set of kinematic cuts specifically designed to enhance $t\bar{t}$ [11]. Only $t\bar{t}$ candidates with a signature compatible with the lepton+jets channel are retained. The selection cuts are:

- the event has passed either the electron or muon trigger chain chosen for $t\bar{t}$ analysis, i.e. EF_e20_medium or EF_mu18;
- there are at least five tracks originating from the primary vertex candidate;
- the event has exactly one selected electron (Section 4.1.3) with $E_T > 25$ GeV or one selected muon (Section 4.1.2) with $p_T > 20$ GeV;
- the selected lepton is the object that fires the trigger used to select the event;
- the event has a minimum amount of missing transverse energy to account for the escape of a neutrino: in the electron channel $E_T^{Miss} > 35$ GeV and in muon channel

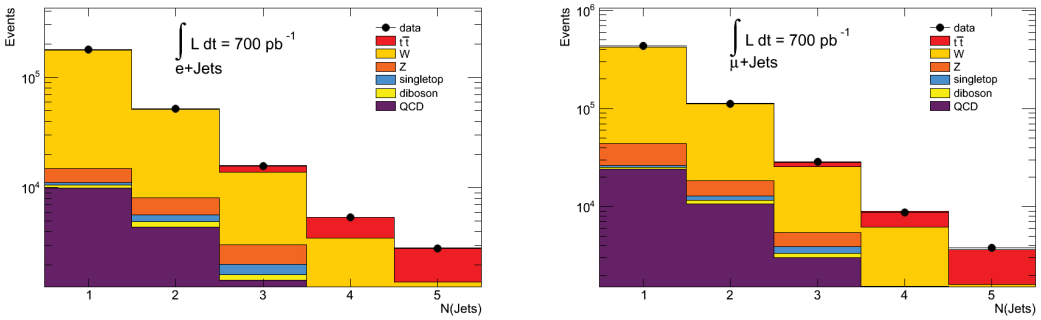

Figure 4.8: Signal and background yield after event selection in the electron (left) and in the muon (right) channel as a function of the number of selected jets in the final state. The last jet bin is inclusive.

$\mathrm{E}_T^{Miss} > 25$ GeV.

The primary vertex selection helps the rejection of non-collision background. The cut on the missing transverse energy plays a central role in the rejection of the QCD multi-jet background. This process, which can fake the $t\bar{t}$ signal when one of the jets is misidentified as a lepton or when a hadron inside a jet decays into a lepton that happens to pass the isolation cuts required for $t\bar{t}$ analysis, has in fact no missing energy. The missing-transverse-energy threshold value differs between the electron and the muon channel because the QCD contamination is of different magnitude: before any selection the QCD background is larger in the electron channel than in the muon channel. This is due to the fact that jets have an experimental signature which is similar to that of the electrons whereas they do not normally leave hits in the three layers of the muon chambers.
The charged lepton and the neutrino of a $t\bar{t}$ event are the decay products of a W boson. However, the direct reconstruction of the W boson mass is prevented by the impossibility of measuring the z component of the neutrino momentum due to the significant amount of unmeasured longitudinal momentum carried by the proton remnants down the beam pipe. Instead we reconstruct the W transverse mass, defined as:

$$M_T(W) = \sqrt{2p_T^{\ell} p_T^{\nu}(1 - \cos\phi_{\ell\nu})} \tag{4.8}$$

where $\phi_{\ell\nu}$ is the angle between the charged lepton and the neutrino, i.e. the missing transverse energy, in the transverse plane and p_T^{ν} coincides with the missing transverse energy. As shown in Figure 4.6, this gives a Jacobian peak with an edge at the W mass and the bulk of the distribution lying below the W mass comes from events with a non-zero lepton longitudinal momentum. The tail above the W mass arises from the width of the W and from events in which the W is not produced at rest. The selection of $t\bar{t}$ candidates of this analysis also includes:

- $M_T(W) > 25$ GeV in the electron channel and

- $M_T(W) + \mathrm{E}_T^{Miss} > 60$ GeV in the muon channel.

In the muon channel, a triangular region in the E_T^{Miss}-$M_T(W)$ plane is excluded. This is motivated by the fact that true $W \to \ell\nu$ events with large E_T^{Miss} also have large $M_T(W)$. This effect is not reproduced by the QCD multi-jet events reconstructed with a fake lepton and hence this cut achieves further rejection against this background. In the electron channel a more stringent cut on $M_T(W)$ is required because of the more important QCD background.
Although a total number of four jets is expected[2] the requirement on the number of final-state jets is loosened to include signal events in which a jet is not reconstructed properly or falls outside the acceptance region considered and events in which there is enhanced parton activity. Figure 4.7 shows the expected number of selected $t\bar{t}$ events in an integrated luminosity of 700 pb^{-1} as a function of the number of jets. The same distribution for the major background, the simultaneous production of a W boson and QCD jets (see next section) is also shown. It is possible to see that the signal yield in the exclusive three-jet bin and in the inclusive five-jet bin is comparable to the signal yield of the exclusive four-jet bin. However, the signal-to-background ratio is degraded substantially in the lower multiplicity bins (one and two jets) due to larger background contamination. For this reason we define the signal region as consisting of three different numbers of well reconstructed jets: an exclusive number of three and four jets and an inclusive number of at least five jets.
The number of data and MC events obtained after the selection described in this section is shown in Figure 4.8 as a function of the jet multiplicity in the electron and in the muon channel separately. In these plots the data is drawn on top of the stacked histograms of all the processes expected to contribute. These are the $t\bar{t}$ signal and five sources of background which will be discussed in the next section. One can also see how the first two jet bins are completely dominated by the background while the $t\bar{t}$ signal (in red) starts to emerge in the three-jet bin. Detailed event yields are also listed in Tables 4.1 and 4.2.

4.3 Estimation of background processes

There is a number of SM processes that can be misidentified as semi-leptonic $t\bar{t}$ events at rates large enough to significantly affect the $t\bar{t}$ reconstruction and production cross-section measurement. They are reviewed in this section.

4.3.1 W+Jets

The main source of background for semi-leptonic $t\bar{t}$ events is the production of a W boson in conjunction with jets: when the W decays leptonically, we have exactly the same final state objects in the detector. This background is taken from simulation and the details of the MC samples were given in Section 3.2.2. Since the normalization of this

[2] Two light jets come from the hadronic decay of one of the W bosons and two hard jets from the hadronization of the b quarks.

Electron Channel	1 Jet	2 Jets	3 Jets	4 Jets	>4 Jets
$t\bar{t}$	232	1010	1958	1891	1449
W+Jets	161932	43112	10834	2486	1024
QCD	9949	4409	1455	465	153
Single top	574	704	379	146	61
Z + jets	3781	2482	1022	342	150
Di-boson	603	537	177	45	10
Total Predicted	177072	52255	15824	5376	2847
Data Observed	179461	51823	15622	5397	2813

Table 4.1: Event yields in the electron channel. The data yield corresponds to the number of events selected in 700 pb^{-1} of collision data at $\sqrt{s} = 7$ TeV. The MC yields for $t\bar{t}$, W and Z+Jets, single top and di-boson production are normalized to the same integrated luminosity. The final number of W+Jets events is corrected with the data-driven scale factors from charge-asymmetry measurements (Section 4.3.1). QCD is extracted directly from data (Section 4.3.2). The total number of predicted events is the sum of the processes considered.

Muon Channel	1 Jet	2 Jets	3 Jets	4 Jets	>4 Jets
$t\bar{t}$	309	1356	2734	2719	2034
W+Jets	382668	93418	20188	4643	1079
QCD	24248	10633	3028	826	276
Single top	1000	1138	573	199	80
Z + jets	17436	5568	1552	450	156
Diboson	1091	1006	307	69	17
Total Predicted	426753	113119	28382	8906	3643
Data Observed	433913	111738	28640	8680	3815

Table 4.2: Event yields in the muon channel. The same description of Table 4.1 holds.

	Muon channel	Electron channel
1 Jet	0.983 ± 0.034	0.948 ± 0.080
2 Jets	0.942 ± 0.076	0.907 ± 0.058
3 Jets	0.870 ± 0.097	0.881 ± 0.123
4 Jets	0.849 ± 0.142	0.839 ± 0.166
≥ 5 Jets	0.687 ± 0.180	1.098 ± 0.331

Table 4.3: Data-driven scale factors to correct the normalization of W+Jets in MC. The scale factors are provided for the electron and muon channel separately and for different number of jets [157].

process is not accurately known in MC, a data-driven correction is required. The overall normalization is extracted from data using a method that exploits the asymmetric cross section for positive and negative charged leptons from W decays. The reason why the W boson production in proton-proton collisions is charge asymmetric stems from the relative difference in the quark-antiquark PDFs. Positively charged W bosons can be produced from parton level processes such as $u\bar{d} \to W^+$ or $c\bar{s} \to W^+$ and depend on products of PDFs such as $u(x_1)\bar{d}(x_2)$. Negatively charged W bosons can be produced in e.g. $d\bar{u} \to W^-$ or $s\bar{c} \to W^-$ and depend on products such as $d(x_1)\bar{u}(x_2)$. The PDFs of up and down valence quarks are different in a proton and hence there is charge asymmetry. The ratio:

$$r = \frac{\sigma(pp \to W^+)}{\sigma(pp \to W^-)} \tag{4.9}$$

is relatively well understood in theory [132, 121]. The main theoretical uncertainty on r is due to the PDF uncertainty and r is predicted within a few percent at LHC energies, which is better than the prediction of the total cross section for the production of W bosons in association with three or more jets. The formula used to extract the W+Jets background is [11]:

$$N_{W^+} + N_{W^-} = \frac{\left(N_{W^+}^{MC} + N_{W^-}^{MC}\right)}{\left(N_{W^+}^{MC} - N_{W^-}^{MC}\right)} \left(D^+ - D^-\right) = \left(\frac{r_{MC}+1}{r_{MC}-1}\right) \left(D^+ - D^-\right) \tag{4.10}$$

where D^+ and D^- are the total number of events in data after the standard $t\bar{t}$ selection with a lepton positively and negatively charged and r_{MC} is the ratio in 4.9 evaluated on MC simulation. Equation 4.10 is valid because $t\bar{t}$, QCD and Z+Jets are charge symmetric and hence $N_{W^+} + N_{W^-} \approx D^+ - D^-$ is a good approximation. There is a small source of charge asymmetry in data from single top production; this contribution is estimated from MC simulation and subtracted from Equation 4.10. Scale factors defined as the ratio between the number of W+Jets events estimated with the charge asymmetry method and the MC prediction were centrally provided to all top quark analyses. The numbers used in this analysis are listed in Table 4.3.

4.3.2 QCD

The nominal contribution of the QCD multi-jet background is estimated from data with the *matrix method* in both channels. This method is based on counting events with two sets of identification criteria: in this context the set of standard $t\bar{t}$ cuts becomes the *tight* QCD selection; in addition a loosened version is defined similar to the standard one but in which some lepton requirements are dropped. The requirements dropped in the muon channel for the *loose* selection are the track-based and the calorimeter-based muon isolation cuts. For the loose electron selection, the tight electron quality is replaced by the medium one with the additional requirement of a hit in the innermost layer of the pixel detector. The electron isolation requirement is also loosened: the value of EtCone20 is required to be less than 6 GeV instead of 3.5 GeV.
The objects passing the loose lepton selection but failing the tight one are considered to be fake leptons. They are likely to originate from semi-leptonic b-quark jet decays, long lived weakly decaying states such as $\pi^{\pm}$ or K mesons, mis-reconstruction of π^0 showers or photons and leptons from photon conversion.
The total number of events passing the loose selection in each channel is:

$$N^{\text{loose}} = N^{\text{loose}}_{\text{real}} + N^{\text{loose}}_{\text{fake}} \tag{4.11}$$

where $N^{\text{loose}}_{\text{real}}$ ($N^{\text{loose}}_{\text{fake}}$) is the contribution from events containing real (fake) leptons which pass the loose selection. The total number of events passing the tight selection can be expressed by:

$$N^{\text{tight}} = \varepsilon_{\text{real}} N^{\text{loose}}_{\text{real}} + \varepsilon_{\text{fake}} N^{\text{loose}}_{\text{fake}} \tag{4.12}$$

where $\varepsilon_{\text{real}}$ and $\varepsilon_{\text{fake}}$ are the efficiencies for a loose real and fake lepton to also fulfill the tight selection criteria:

$$\varepsilon_{\text{real}} = \frac{N^{\text{tight}}_{\text{real}}}{N^{\text{loose}}_{\text{real}}} \tag{4.13}$$

and

$$\varepsilon_{\text{fake}} = \frac{N^{\text{tight}}_{\text{fake}}}{N^{\text{loose}}_{\text{fake}}}. \tag{4.14}$$

The efficiency for real muons is measured with the Tag and Probe method in a sample of $Z \to \mu\mu$ events. Analogously $\varepsilon_{\text{real}}$ in the electron channel is derived with the same method in a sample of $Z \to ee$ events. The fake-lepton efficiency is measured in QCD-enriched data samples: in the muon channel this is obtained using a low transverse mass region $M_T(W) < 20$ GeV with an inverted triangular cut $M_T(W) + \text{E}_T^{Miss} < 60$ GeV and in the electron channel using a low missing transverse energy region 5 GeV $< E_T^{Miss} < 20$ GeV. In the muon channel the efficiencies are parameterized as a function of muon η, to account for effects due to detector acceptance, and leading jet p_T, which is a measure of the event hadronic activity and hence of muon isolation. The efficiencies in the electron channel are a function of electron η.

The number of fake leptons passing the tight selection can be expressed by:

$$N_{\text{fake}}^{\text{tight}} = \frac{\varepsilon_{\text{fake}}}{\varepsilon_{\text{real}} - \varepsilon_{\text{fake}}} \left(N^{\text{loose}} \varepsilon_{\text{real}} - N^{\text{tight}} \right) \tag{4.15}$$

The final estimate in Equation 4.15 can be translated into event weights giving the probability for an event passing the loose selection to also fulfill the tight one. The weights obtained with the matrix method in both channels are provided by the ATLAS collaboration [24] so that the final QCD sample is obtained by selecting loose data events and by applying these weights on an event-by-event base.
A second implementation of the matrix method in the muon channel is based on a different parameterization for the fake efficiency: in addition to muon η and leading jet p_T also the distance $\Delta R_{\text{min}}(\mu, \text{jet})$ between the muon and the closest jet is used thus taking into account also the dependency on jet multiplicity[3]. The nominal QCD estimate in the muon channel is build from the average estimate between the two available matrix-method implementations, as recommended by the *Top Working Group* of the ATLAS collaboration. The systematic uncertainty of the above QCD estimations is estimated to be 50%.

4.3.3 Other backgrounds

Smaller sources of background events include the production of Z bosons in association with jets (Z +Jets), single top quark production and the simultaneous production of two weak bosons. These backgrounds are taken entirely from the MC simulation. The details were given in Section 3.2.2.

[3] The default selection requires $\Delta R_{\text{min}}(\mu, \text{jet}) > 0.4$ (Section 4.1.2). Therefore the fake efficiency is expected to be lower for muons closer to jets and this effects increases with the number of jets in the event.

5 Measurement of the $t\bar{t}$ production cross section in the single lepton channel

5.1 Analysis strategy

The extraction of the $t\bar{t}$ production cross-section is based on a multivariate analysis (MVA). MVA techniques are powerful because they use combined information from a set of discriminating variables which are chosen to enhance the separation between signal and background. The distributions of the discriminating variables for $t\bar{t}$ and W+Jets, which is by far the most important background in this analysis, are passed to a multivariate classifier which is trained to classify the events according to their "signal likeness". The one-dimensional response D of the trained classifier is subsequently applied to the data, the signal and all the background processes and the cross section is extracted in a binned maximum likelihood fit to the data distribution of D. The same procedure is carried out simultaneously in the six channels of the signal region previously defined: electron and muon channel with three, four and more than four jets. As discussed at the end of Section 4.2, events with only three jets are included because they still carry substantial information about the $t\bar{t}$ signal; more importantly this channel also carries additional information about the background that helps to constrain the fit parameters.

The results presented in this chapter are based on the proton-proton collision data collected with the ATLAS detector in the first half of 2011 at the center-of-mass energy $\sqrt{s} = 7$ TeV and during stable-beam conditions. After requiring good-quality criteria for the data acquisition, i.e. all the ATLAS sub-detectors operating under nominal conditions, the total integrated luminosity is about 700 pb^{-1}. The statistics available for this measurement is such that the $t\bar{t}$ cross section in the single lepton channel is already dominated by the systematic uncertainties. One remarkable aspect of the MVA approach employed in this analysis is that these are incorporated in the fit through the use of nuisance parameters of the likelihood function and constrained directly in the fit to the data. The same analysis but with slightly different results constituted the most precise $t\bar{t}$ cross-section measurement in the year 2011 [71]. A similar analysis had already been performed with data collected in 2010 for an integrated luminosity of $\int L = 35\,\text{pb}^{-1}$ [3].

Section 5.2 explains in detail the construction of the so-called "templates", the distributions D of the multivariate classifier, starting from four input variables. Section 5.3 describes the extraction of the cross-section and in Section 5.4 its systematic uncertainties are addressed. The results are discussed in Section 5.5.

5.2 Classification

A good event classification mainly relies on a good discrimination between signal and background. In order to enhance the discrimination power, more than one variable can be combined through a statistical approach. The criteria that the variables are required to meet are particularly based on considerations of:

- their simultaneous separation power in both electron and muon channel and in all three jet-multiplicity bins;
- their overall data-MC agreement.

The technique used to extract the cross section proved to be able to constrain the systematic uncertainties affecting the cross section directly in the fit to the data (see [3] and [71]). Armed with this knowledge, this aspect can be exploited to constrain the largest sources of systematic uncertainty by including variables that are especially sensitive to them. Lastly, to retain a good compromise between discrimination power and simplicity, a total number of four variables is chosen.
The input variables on which the presented measurement of the $t\bar{t}$ cross section is based are described in this section.

Charged-lepton pseudorapidity

Compared to W+Jets events, the charged lepton produced in semi-leptonic decays of $t\bar{t}$ pairs is more often emitted in the central region of the detector. From the distributions in Figure 5.1 and Figure 5.2 we see that the pseudorapidity of the charged lepton provides a good separation power in both the electron and the muon channel and in all jet multiplicity bins. It is also worth noting that the lepton pseudorapidity is a well understood variable not expected to introduce correlations with the other input variables (see Section 5.2, in particular Figure 5.14 and 5.15). The pseudorapidity of the electrons is transformed to hide the discontinuity stemming from the presence of a transition region between the calorimeters:

$$\eta^e = \begin{cases} \eta & \text{for } |\eta| < 1.37 \\ \eta - 0.15 & \text{for } 1.52 < \eta < 2.47 \\ \eta + 0.15 & \text{for } -2.47 < \eta < -1.52 \end{cases} \tag{5.1}$$

The data-MC comparison for this variable after event selection is shown in Figure 5.3 and 5.4: the shape and the normalization of the data is reproduced by the cumulative contribution of the six physics processes considered moderately well.

Leading-jet transverse momentum

The "leading" jet is the jet of the event with the highest transverse momentum. The p_T of the leading jet is by definition very sensitive to the uncertainty in the jet energy-scale calibration (see Section 2.3.3) which is known to be one of the largest sources of

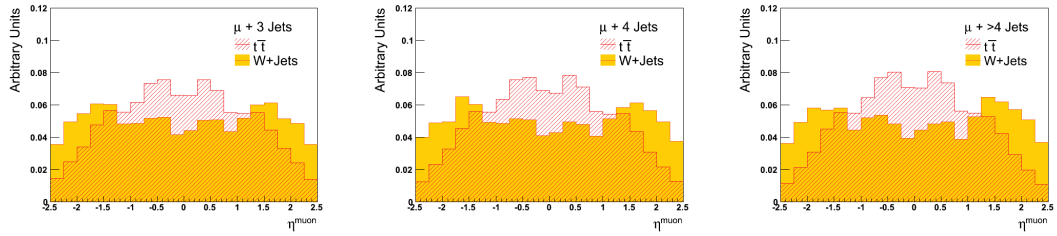

Figure 5.1: Normalized distributions of the muon pseudorapidity for selected $t\bar{t}$ and W+Jets MC events decaying in the muon channel.

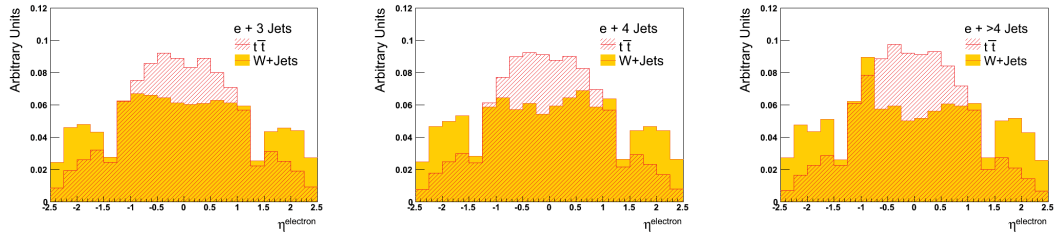

Figure 5.2: Normalized distributions of the transformed electron pseudorapidity for selected $t\bar{t}$ and W+Jets MC events decaying in the electron channel.

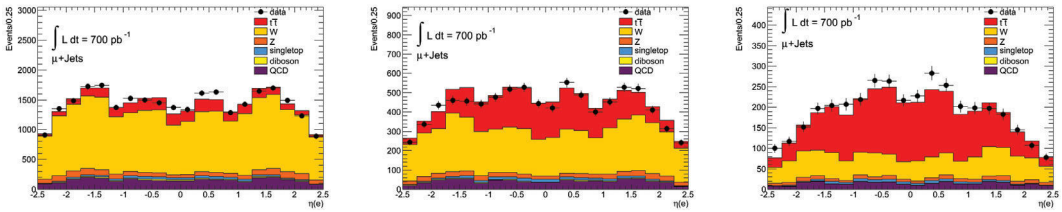

Figure 5.3: Muon pseudorapidity of selected events with three (left) four (middle) and more than four (right) jets. The simulated processes are normalized to 700 pb^{-1}.

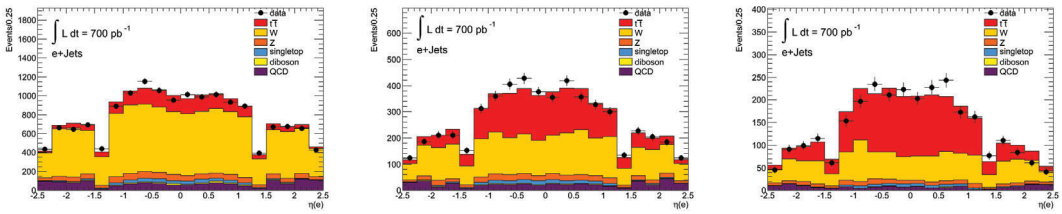

Figure 5.4: Electron pseudorapidity of selected events with three (left) four (middle) and more than four (right) jets. The simulated processes are normalized to 700 pb^{-1}.

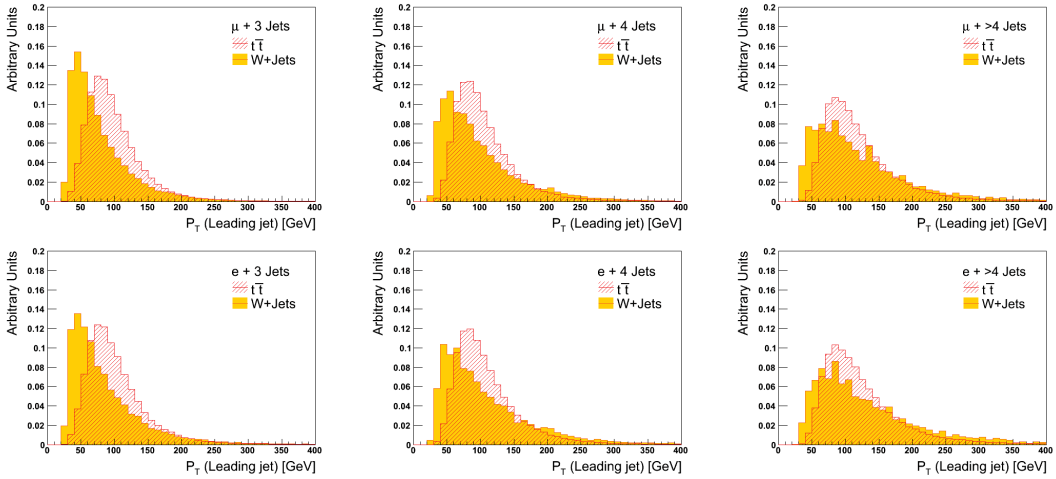

Figure 5.5: Normalized leading-jet p_T for selected $t\bar{t}$ and W+Jets MC events.

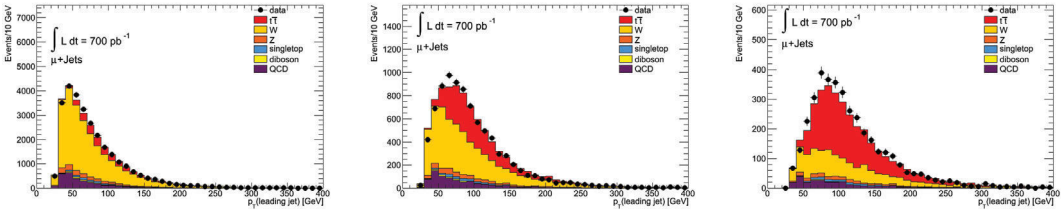

Figure 5.6: Leading-jet p_T of selected events in the muon channel. From left to right the distribution is shown for events with three, four and more than four jets. The simulated processes are normalized to 700 pb^{-1}.

systematic uncertainty affecting the cross section measurement. The leading-jet p_T was not used in the analysis performed with 2010 data but instead it was introduced for the more precise measurement in 2011 [71]. The motivation behind the inclusion of this variable was driven by the expectation of reducing the contribution of the jet energy scale uncertainty to the total uncertainty of the cross section due to the possibility of constraining it directly from the data in the fitting procedure. The presented analysis uses the leading-jet p_T for consistency with Ref. [71].
The separation power is shown in Figure 5.5: while this is good in the lower jet-multiplicity bins, the W+Jets background looks more similar to the $t\bar{t}$ signal in events with at least five jets. This effect will be reflected in the performance of the MVA classifier (see next section). The data-MC comparison for this variable is shown in Figure 5.6 and 5.7.

$H_{T,3p}$

The $H_{T,3p}$ variable belongs to the category of event-shape variables which characterize the topology of an event's energy flow. It is defined as the sum of the transverse mo-

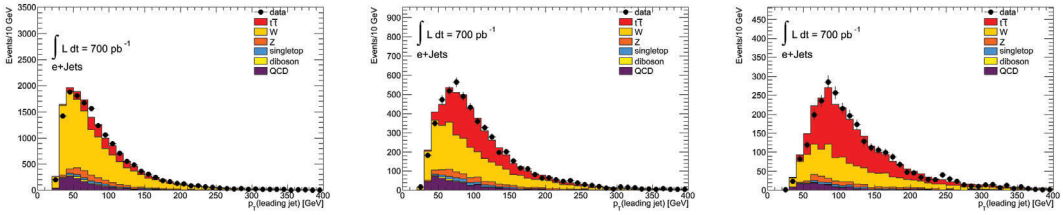

Figure 5.7: Leading-jet p_T of selected events in the electron channel. From left to right the distribution is shown for events with three, four and more than four jets. The simulated processes are normalized to 700 pb^{-1}.

mentum of the third leading jet and, if present, the fourth leading jet normalized to the sum of the absolute values of all the longitudinal momenta of all the selected objects of the event:

$$H_{T,3p} = \frac{\sum_{i=3}^{N_{\text{jets}=4}} p_{T,i}}{\sum_{j=1}^{N_{\text{objects}}} |p_{z,j}|} \tag{5.2}$$

The sum over the objects includes the charged lepton, the neutrino and up to four leading jets. As hinted before, the longitudinal momentum of the neutrino can not be inferred by the energy imbalance in the longitudinal direction because of the unmeasured component carried away by the proton remnants in the beam pipe. Instead we impose a W mass constraint on the charged lepton-neutrino system:

$$\begin{aligned} P_W^2 = M_W^2 &= (P_\ell + P_\nu)^2 \\ &= (E_\ell + E_\nu)^2 - (\vec{p}_\ell + \vec{p}_\nu)^2, \end{aligned}$$

and solve for $p_{z,\nu}$, the unknown longitudinal component of the neutrino momentum:

$$M_W^2 = (E_\ell + E_\nu)^2 - (\vec{p}_{T,\ell} + \vec{p}_{T,\nu})^2 - (p_{z,\ell} + p_{z,\nu})^2. \tag{5.3}$$

Here, P_W, P_ℓ and P_ν are the four-momentum of the W boson, the charged lepton and the neutrino. E_ν in Equation 5.3 can be written as $E_\nu = \sqrt{p_{T,\nu}^2 + p_{z,\nu}^2}$. Equation 5.3 is thus a quadratic equation with a two-fold ambiguity for $p_{z,\nu}$; in this analysis the smaller $p_{z,\nu}$ solution is always chosen.
To obtain a smoother input distribution for the multivariate classifier, the $\mathrm{H}_{T,3p}$ variable is transformed into $H_{T,3p} \rightarrow \exp(-4 \times H_{T,3p})$. The separation power and data-MC agreement for $\exp(-4 \times H_{T,3p})$ are shown in Figure 5.8 and Figures 5.9 and 5.10. No significant deviation between predictions and data is observed.

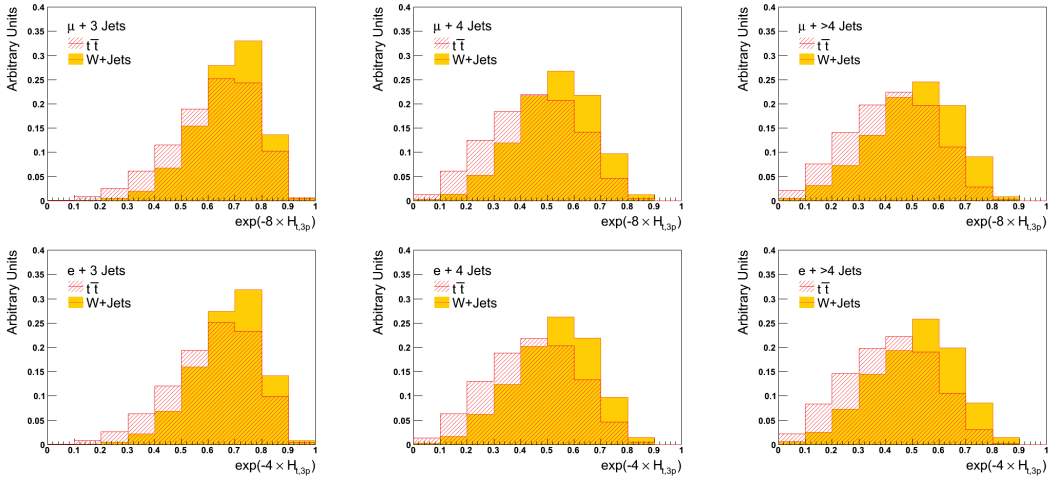

Figure 5.8: Normalized distributions of $\exp(-4 \times H_{T,3p})$ for selected $t\bar{t}$ and W+Jets MC events.

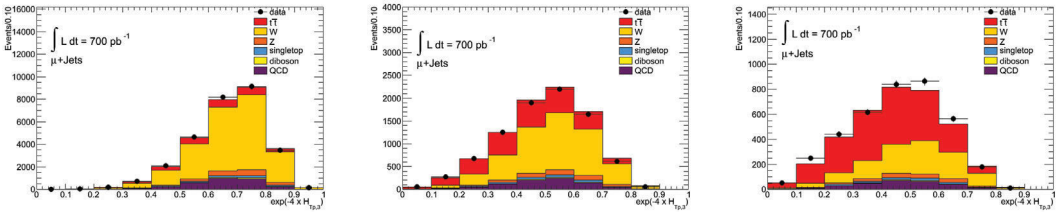

Figure 5.9: $\exp(-4 \times H_{T,3p})$ of selected events in the muon channel. From left to right the distribution is shown for events with three, four and more than four jets. The simulated processes are normalized to 700 pb^{-1}.

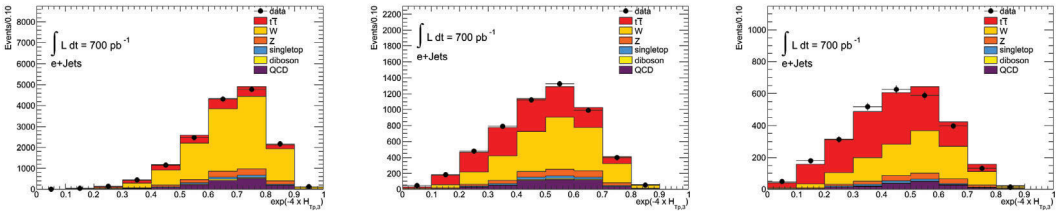

Figure 5.10: $\exp(-4 \times H_{T,3p})$ of selected events in the electron channel. From left to right the distribution is shown for events with three, four and more than four jets. The simulated processes are normalized to 700 pb^{-1}.

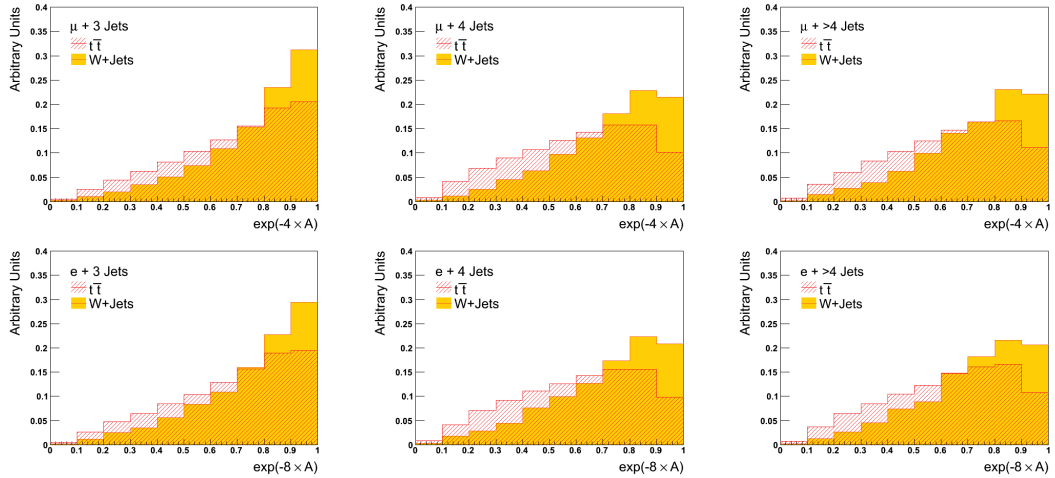

Figure 5.11: Normalized distributions of $\exp(-8 \times A)$ for selected $t\bar{t}$ and W+Jets MC events.

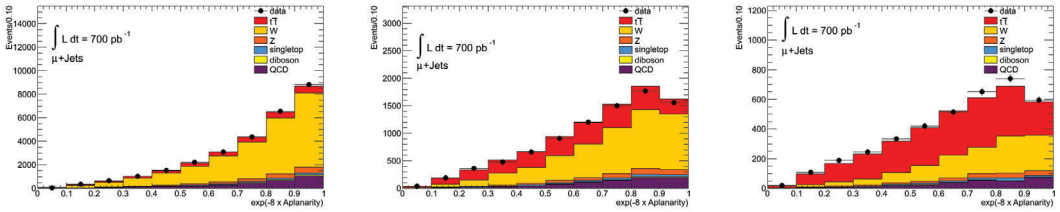

Figure 5.12: $\exp(-8 \times A)$ of selected events in the muon channel. From left to right the distribution is shown for events with three, four and more than four jets. The simulated processes are normalized to 700 pb^{-1}.

Aplanarity

The aplanarity A is another event-shape variable. It is defined as 1.5 times the smallest eigenvalue of the momentum tensor which is defined as:

$$M_{ij} = \frac{\sum_{k=1}^{N'_{\text{objects}}} p_{ik} p_{jk}}{\sum_{k=1}^{N'_{\text{objects}}} p_k^2} \tag{5.4}$$

where p_{ik} is the i-th momentum component of the object k and p_k is the modulus of its momentum. The sum is over the momenta of up to four leading jets and the charged lepton. To obtain a smoother input distribution for the likelihood discriminant the aplanarity is transformed into $A \to \exp(-8 \times A)$. The separation power and the data-MC agreement for $\exp(-8 \times A)$ are shown in Figure 5.11 and Figures 5.12 and 5.13.

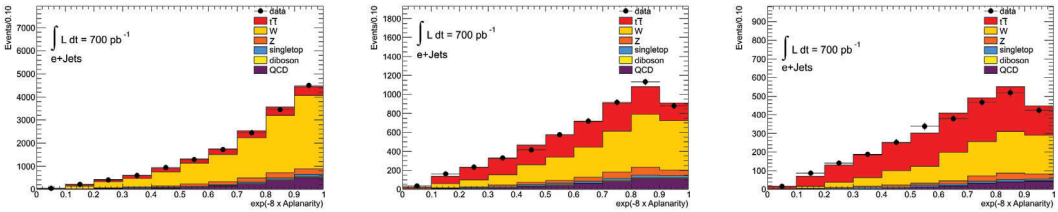

Figure 5.13: $\exp(-8 \times A)$ of the selected events in the electron channel. From left to right the distribution is shown for events with three, four and more than four jets. The simulated processes are normalized to 700 pb^{-1}.

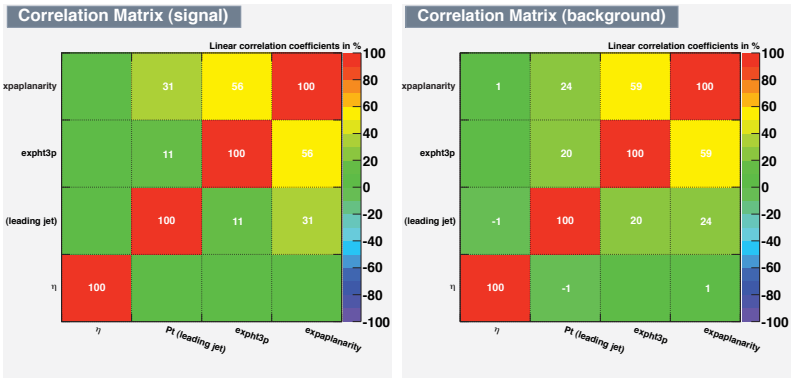

Figure 5.14: Linear correlation coefficients between the four input variables for the training samples of $t\bar{t}$ (left) and W+Jets (right) in the e + 4 jets channel.

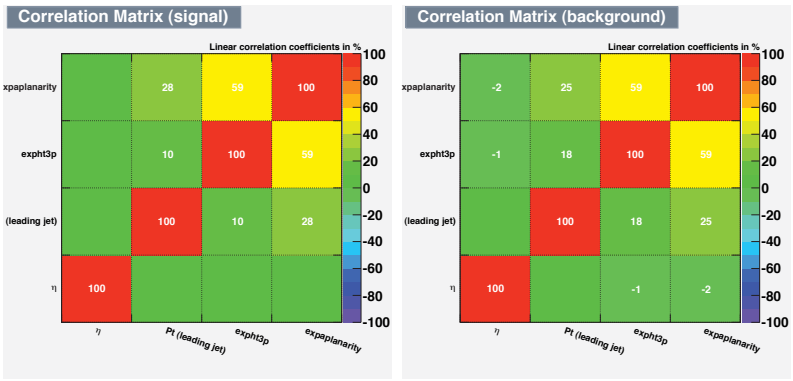

Figure 5.15: Linear correlation coefficients between the four input variables for the training samples of $t\bar{t}$ (left) and W+Jets (right) in the μ + 4 jets channel.

Likelihood classifier

The analysis proceeds with the classification of the data, the signal and the backgrounds. This is performed by a software package called TMVA [106]. A typical TMVA classification analysis consists of two independent phases: the training phase, where a multivariate method is trained, tested and evaluated and an application phase, where the method is applied. For this analysis, a projective likelihood estimator is trained, independently in all six channels, to distinguish between $t\bar{t}$ and W+Jets events using the four input variables described above. The inclusion of the other (smaller) backgrounds in the training phase did not provide any significant gain in classification power and therefore only $t\bar{t}$ and W+Jets are used at this stage. Before the beginning of the training phase, the input data sets in each channel are randomly halved in two subsets which are used separately to ensure statistical independence between training and application. The application subsets are always re-normalized to the total number of events in each channel.
As described in [106], the method of maximum likelihood consists of building a model out of probability density functions (PDF) that reproduce the input variables for signal and background. For a given event, the likelihood for being of signal type is obtained by multiplying the signal probability densities of all input variables, which are assumed to be independent, and normalising this by the sum of the signal and background likelihoods, i.e. the likelihood ratio $y_{\mathcal{L}}(i)$ for the event i is defined by:

$$y_{\mathcal{L}}(i) = \frac{\mathcal{L}_S(i)}{\mathcal{L}_S(i) + \mathcal{L}_B(i)}, \tag{5.5}$$

where:

$$\mathcal{L}_{S(B)}(i) = \prod_{k=1}^{n_{\text{var}}} p_{S(B),k}(x_k(i)) \tag{5.6}$$

In Equation 5.6 $n_{\text{var}} = 4$ and $p_{S(B),k}$ is the signal (background) PDF for the kth input variable x_k. The PDFs are normalized:

$$\int_{-\infty}^{\infty} p_{S(B),k}(x_k)dx_k = 1 \qquad \forall k. \tag{5.7}$$

The one-dimensional probability densities of the four input variables are unknown and their shapes are empirically approximated in TMVA by interpolating the bin centers of the training-data histograms with nonparametric, quadratic spline curves. Beside a faithful representation of the data, it is important at this stage that statistical fluctuations of the training-data histograms are smoothed out as much as possible without destroying the significant information. The likelihood method crucially depends on a good-quality PDF representation. Since this is strongly case dependent, TMVA provides the user with a number of parameters that can be adjusted to improve the performance of the training phase: these parameters usually modify the copies of the histograms of the input variables on which the PDFs are estimated. The most relevant parameters have been found to be the average number of entries per bin and the number of smoothing iteration via TH1::Smooth() [148]. The values chosen are documented in Table 5.1. The

agreement between input training data and PDFs can be scrutinized visually and by means of statistical tests printed on the standard output, e.g. a χ^2 estimator between the original input distribution and the PDF constructed on its modified copy.
A drawback of the likelihood classifier is that it ignores the correlations among the discriminating input variables (see Equation 5.6). In realistic cases this is not an accurate assumption and it leads to performance loss. Figures 5.14 and 5.15 show the linear correlation coefficients among the input variables evaluated by TMVA on the training samples of the $t\bar{t}$ signal and the W+Jets background in the electron and muon channel with four jets. These linear correlation matrices are similar to and hence representative of the other four channels. Furthermore, the scatter plots in Figure 5.16 and 5.17 for $t\bar{t}$ and W+Jets in the electron channel with four jets help to visualize also the non-linear components of the correlations. Similar scatter plots are obtained in the other five channels. As expected by their construction, the two event shape variables are correlated with the transverse momentum of the leading jet and, to a greater extent, with each other.
A linear decorrelation procedure is applied before the beginning of the training phase. TMVA computes the linear decorrelation by first diagonalising the covariance matrix C and computing its square-root:

$$D = S^T C S \qquad \rightarrow \qquad C' = S\sqrt{D}S^T \tag{5.8}$$

(where S is a diagonal matrix) and then by multiplying the initial variable tuple $\mathbf{x}$ by the inverse of the square-root matrix:

$$\mathbf{x} \rightarrow (C')^{-1}\mathbf{x}. \tag{5.9}$$

The linear decorrelation procedure does not have a strong effect, probably due to the presence of the nonlinear components. Only little additional information is recovered, as reflected in the slight increase of:

- the area of the background rejection versus signal efficiency function (Receiving Operating Characteristic, ROC);
- the separation $\langle S^2 \rangle$, defined by:

$$\langle S^2 \rangle = \frac{1}{2} \int \frac{(\hat{y}_S(y) - \hat{y}_B(y))^2}{\hat{y}_S(y) + \hat{y}_B(y)} dy \tag{5.10}$$

  where $\hat{y}_S(y)$ and $\hat{y}_B(y)$ are the signal and background PDFs of the response value y of the classifier;
- the discrimination significance, defined by the difference between the classifier means for signal and background divided by the quadratic sum of their root-mean-squares.

A larger value for the integral of the ROC curve indicates a better performance. The separation is zero for identical signal and background shapes and it is one for shapes

Variable	Number of jets	Smoothing iterations	Average events per bin
Lepton η	3,4	5	500
Leading jet p_T	3,4	0	500
Aplanarity	3,4	5	500
$H_{T,3p}$	3,4	5	500
Lepton η	>4	2	300
Leading jet p_T	>4	0	300
Aplanarity	>4	2	300
$H_{T,3p}$	>4	2	300

Table 5.1: TMVA settings of the training phase. These parameters were adjusted to improve the goodness of the PDFs estimated on the distributions of the input variables. They are the number of smoothing iterations via TH1::Smooth() and the average number of entries per bin.

with no overlaps. The values obtained before and after linear decorrelation are printed to standard output after the evaluation of the training phase and summarized in Table 5.2. Given the very little improvement in classification power provided by the linear decorrelation, the procedure is discarded for the sake of simplicity.
The trained likelihood estimator is used to classify the data, whose composition is unknown, the signal and the backgrounds. For each channel, the classifier output is stored in histograms called *templates*. By TMVA convention, signal (background) events accumulate at large (small) classifier output value, which is limited in the range between 0 and 1. Figures 5.18 and 5.19 show the normalized response for $t\bar{t}$ and W+Jets events. In general, the overlap region is significant, suggesting that the likelihood classifier underperforms: this is probably due to an overall weak discriminating power of the input variables as well as the presence of internal correlations. Also visible is a slight decrease in performance towards higher jet multiplicities. This effect stems from the increasing signal-likeness of the W-Jets background as a function of the number of jets. In Figure 5.20 and 5.21 the data template is drawn on top of the stacked templates from all six physics processes. These distributions represent the (nominal) input to the extraction of the $t\bar{t}$ production cross section, presented in Section 5.3.

Overtraining check

The problem of overtraining occurs when too many model parameters are adjusted on too few data points. Overtraining leads to a fictitious increase of the classification performance measured on the training sample. A way to detect overtraining is thus to compare the training performance on a statistically independent sample. The sensitivity to overtraining depends on the number of model parameters and thus on the MVA method chosen. The likelihood method is known to be only mildly affected. However, an overtraining check is performed. The training sample is split in two: one half is used for the actual training of the likelihood classifier and the other half is used only in the

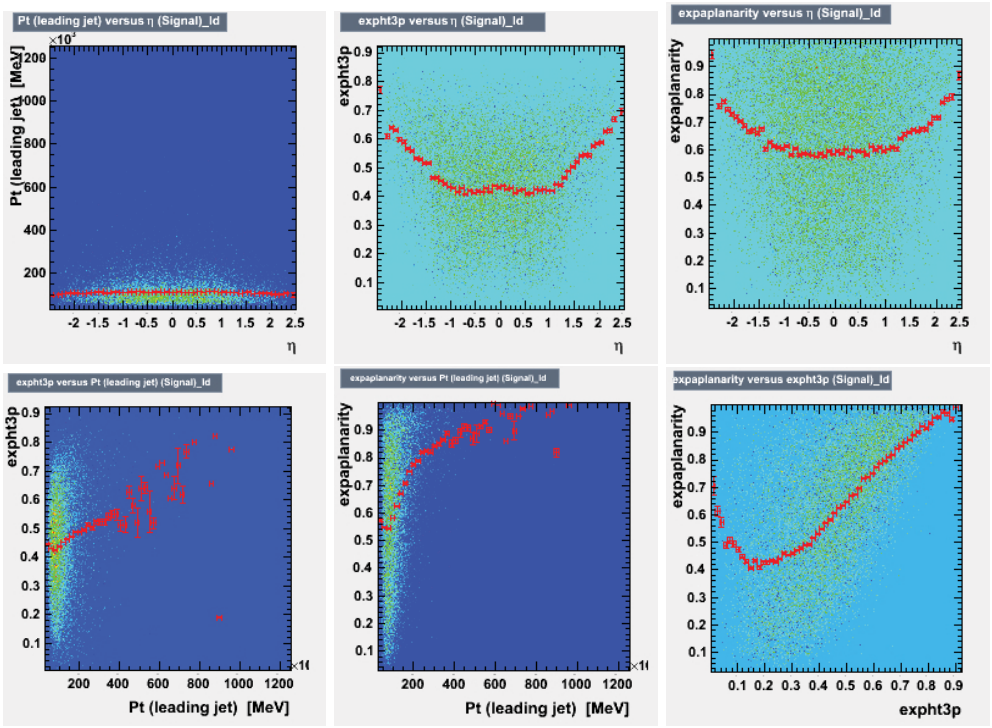

Figure 5.16: Scatter plots with the superimposed profile showing the correlation between the input variables for the training sample of the $t\bar{t}$ signal in the electron channel with four jets.

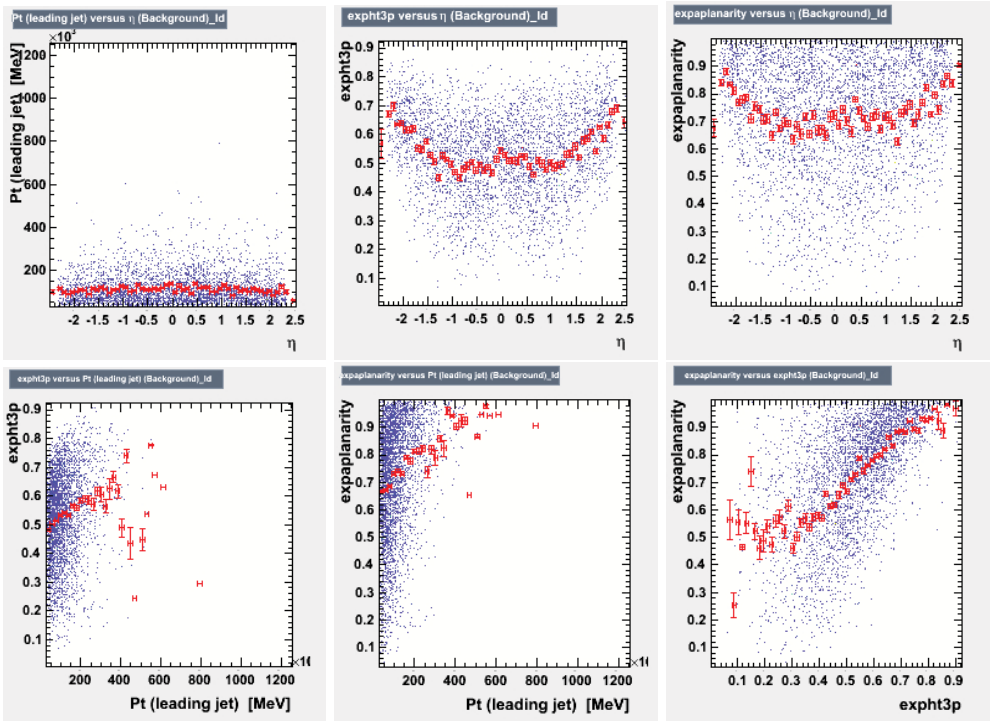

Figure 5.17: Scatter plots with the superimposed profile showing the correlation between the input variables for the training sample of the W+Jets background in the electron channel with four jets.

Channel	ROC-integ.	Separation	Significance
e + 3 jets	0.736	0.179	0.616
e + 3 jets (deco)	0.739	0.184	0.625
e + 4 jets	0.721	0.173	0.600
e + 4 jets (deco)	0.736	0.185	0.632
e + >5 jets	0.731	0.206	0.548
e + >5 jets (deco)	0.748	0.208	0.603
μ + 3 jets	0.765	0.217	0.677
μ + 3 jets (deco)	0.764	0.217	0.681
μ + 4 jets	0.739	0.185	0.636
μ + 4 jets (deco)	0.739	0.185	0.649
μ + >5 jets	0.710	0.167	0.570
μ + >5 jets (deco)	0.717	0.174	0.593

Table 5.2: Area of the background rejection versus signal efficiency function (ROC-integ.), separation and significance, as defined in the text, with and without linear decorrelation.

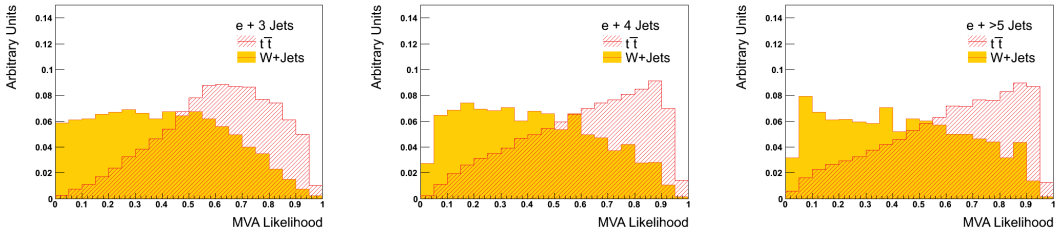

Figure 5.18: Normalized response of the likelihood classifier evaluated on the application sample showing the separation between $t\bar{t}$ and W+Jets in the electron channel.

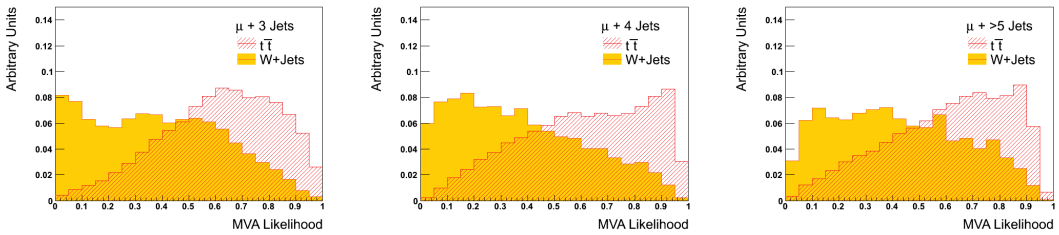

Figure 5.19: Normalized response of the likelihood classifier evaluated on the application sample showing the separation between $t\bar{t}$ and W+Jets in the muon channel.

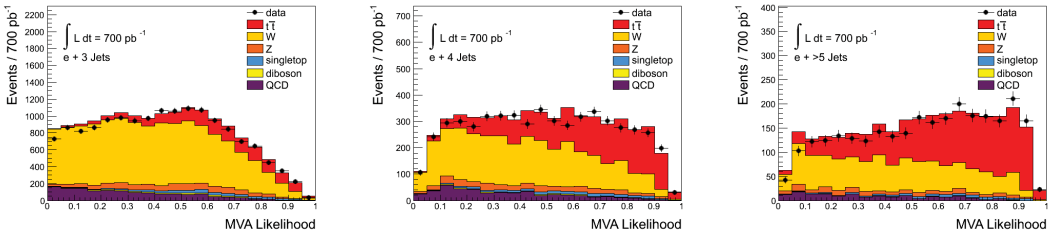

Figure 5.20: Template of the data and stacked templates of the six physics processes considered in the electron channel.

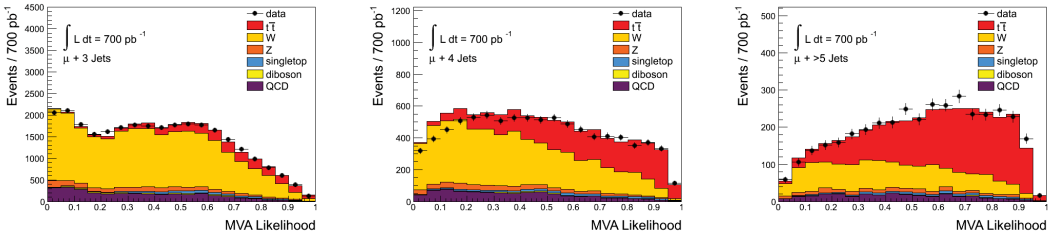

Figure 5.21: Template of the data and stacked templates of the six physics processes considered in the muon channel.

evaluation of the response. The result is shown in Figure 5.22 for the electron and muon channel with four jets: the output of the training sample (data points) is drawn on top of the independent test sample (solid distribution). Analogous results are obtained for the other channels. No significant difference in the classifier performance is observed implying that the method used is free from overtraining problems.

5.3 Extraction of the cross section

The cross section is extracted in a maximum likelihood template fit based on the numerical minimization program MINUIT [107]. The fitter takes as input the templates of the

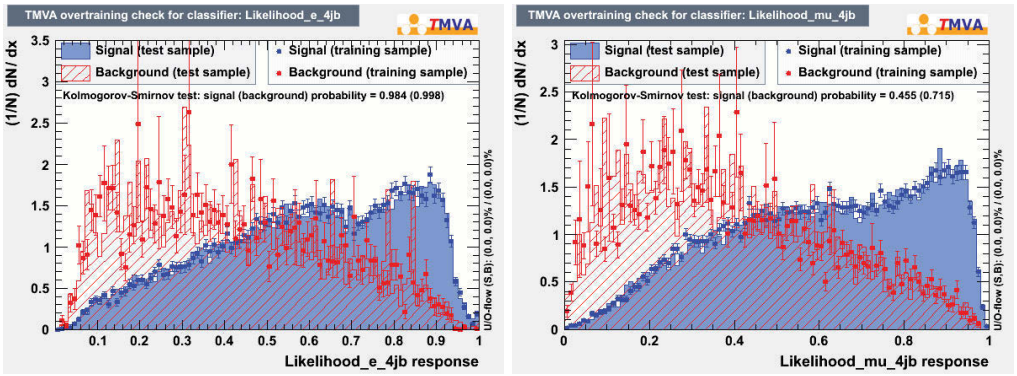

Figure 5.22: Overtraining check in the electron (left) and muon (channel) with four jets.

data, of the signal and of the backgrounds. These come in the form of one-dimensional histograms divided into twenty bins (see Figure 5.20 and 5.21). Before the fit, the templates relative to the six analysis channels are placed side by side and treated as one large one-dimensional histogram with 120 bins, i.e. the fit is performed simultaneously in the six channels.
The construction of the likelihood function to be minimized starts from an extended maximum likelihood function defined as the product of independent Poisson probabilities for each bin of this histogram:

$$\mathcal{L}_0(\vec{\mu}) = \prod_k \frac{\mu_k^{n_k} \exp[-\mu_k]}{n_k!}. \tag{5.11}$$

Here, n_k is the number of events observed in the k-th bin of the data templates and μ_k is the expected number of events in the same bin, calculated from the sum of the bin entries of the signal and background templates. μ_k must depend on the the overall template normalization:

$$\mu_k(\vec{\beta}) = \sum_j \beta_j \nu_{jk} \tag{5.12}$$

where the sum index j runs over all the physics processes, ν_{jk} is the number of entries of the process j in the kth bin and β_j describes the normalization of the physics process j. The parameters β_j are the free parameters of the fit, adjusted in the minimization of $-\ln(\mathcal{L})$ to fit the data. Since the templates for signal and backgrounds are normalized to the integrated luminosity of the data set used, the parameters β_j are initially set to 1.0. Gaussian constraints Δ_j for the β_j parameters can be included by multiplying $\mathcal{L}_0(\vec{\mu})$ with:

$$\prod_j \frac{1}{\sqrt{2\pi}\Delta_j} \exp\left[-\frac{(\beta_j - 1)^2}{2\Delta_j^2}\right] \tag{5.13}$$

There are in total 16 β parameters. The $t\bar{t}$ signal templates are assumed to be 100% correlated across the six channels. The parameter that drives their normalization, β_0, is the parameter of interest: $\beta_0 = \sigma^{t\bar{t}}_{\text{measured}}/\sigma^{t\bar{t}}_{\text{theory}}$ which is left unconstrained in the fit. The relative normalization of the W+Jets templates in the six channels is not expected to be accurate and hence the fit employs six normalization parameters. The templates of the smaller backgrounds, Z+Jets, single top and di-boson production, are treated as 100% correlated across the six channels and there are three β parameters driving their normalization. As discussed in Section 4.3.2, the QCD background is obtained by means of data-driven methods which predict both shape and normalization of this background. As for W+Jets, each channel is assigned an independent normalization parameter for a total of six QCD normalization parameters.
Each systematic uncertainty comes in the form of two additional sets of templates: besides the nominal ones, each process has in each channel a template created with the upper one-standard deviation of a systematic source and another one created with

the lower one-standard deviation of the same source[1]. Because of the thresholds in the event selection, the systematic templates obtained by raising and lowering the value of the systematic parameter are, in general, expected to have a different normalization. At the same time, altering the value of the systematic sources results in an overall distortion in the shape of the template spectra. A typical example is the jet energy scale uncertainty which affects all jet energies in an event in the same direction. The systematic uncertainties are included in the fit via parameters δ_i which are nominally set to $\delta_i = 0$ with a one-standard deviation set to $\delta_i = \pm 1$. To transform them in continuous parameters, the fitter interpolates the parameters δ quadratically between $\delta \in [-1, +1]$ using Lagrange polynomials and linearly outside this range [110]. This general technique is called *vertical morphing*. The δ-parameters are included in the likelihood function by rewriting the expected number of entries for the process j in the k-th bin, ν_{jk} in Equation 5.12, as a function of "morphing" parameters ε_{jik} which are functions of the parameters δ_i. Their explicit form is given by:

$$\varepsilon_{jik}(\delta_i) = \begin{cases} \lambda^+_{jik} + (\delta_i - 1)\left\{\left(\frac{3}{2}\lambda^+_{jik} - 1\right)\left(\frac{1}{2}\lambda^-_{jik} - 1\right)\right\} & \text{for } \delta_i > +1 \\ \frac{1}{2}\delta_i\left\{(\delta_i - 1)\lambda^-_{jik} + (\delta_i + 1)\lambda^+_{jik}\right\} - (\delta_i - 1)(\delta_i + 1) & \text{for } |\delta_i| \leq +1 \\ \lambda^-_{jik} + (\delta_i + 1)\left\{\left(-\frac{1}{2}\lambda^+_{jik} + 1\right)\left(-\frac{3}{2}\lambda^-_{jik} + 1\right)\right\} & \text{for } \delta_i < -1 \end{cases} \quad (5.14)$$

where $\lambda^{\pm}_{jik}$ is the expected number of entries in the k-th bin of the systematic template i of the process j divided by the number of entries in the same bin of the nominal template of the same process:

$$\lambda_{jik} = \frac{\nu^{\pm}_{jik}}{\nu^{\pm}_{jk}}. \quad (5.15)$$

An illustrative example of how template morphing works is given in Figure 5.23 for a simplified scenario in which there is only one systematic source. When there are multiple systematic sources, the expected number of entries per bin in Equation 5.12 is multiplied by the factor $\prod_i \varepsilon_{jik}(\delta_i)$. A Gaussian constraint is applied to the δ-parameters by multiplying $\mathcal{L}_0(\vec{\mu})$ with:

$$\frac{1}{\sqrt{2\pi}} \exp\left(-\frac{\delta_i^2}{2}\right). \quad (5.16)$$

This technique allows the inclusion of those systematic sources in the likelihood function which can be assumed to follow a continuous distribution. In cases where this assumption cannot be considered accurate the effect of the systematic uncertainty is evaluated outside the fit, as described in Section 5.3.1.

Finally, to take into account the statistical uncertainty in the templates due to finite MC samples, the expected number of events in a bin is treated as a Gaussian with uncertainty σ_k^{bin} following a simplified approach of the method suggested in [23]. The uncertainty is obtained from the quadratic sum of the uncertainties of each template, which in turn

[1] Since the fitter always expects for each systematic uncertainty two additional templates for the up and down variations, the templates relative to one-sided systematic sources are symmetrized before the fit with respect to the nominal ones

are given by $1/\sum w_b^2$ where w_b are the weights of each entry in the bin. The expected number of events, μ_k in Equation 5.11, is multiplied with a nuisance parameter δ_k^{bin} and the likelihood function is multiplied for each bin with a Gaussian constraint of the form:

$$\frac{1}{\sqrt{2\pi}} \exp\left[-\frac{(\delta_k^{bin}-1)^2}{2(\sigma_k^{bin})^2}\right]. \tag{5.17}$$

Besides minimizing $-\ln(\mathcal{L})$, MINUIT includes methods designed to analyze the shape of the function around the minimum to evaluate the uncertainty in the parameter values. In particular, the uncertainty in all β and δ parameters is extracted both with HESSE from the second derivatives of $-\ln(\mathcal{L})$ at the minimum and with MINOS which finds asymmetric positive and negative errors by varying the parameters one at a time and searching the value for which the function minimum shifts by a certain fixed amount.

5.3.1 Pseudo-experiments

For many purposes it is useful to create distributions of pseudo-data to be used in the fit in place of the real data. The pseudo-data have the form of regular templates: binned distributions ranging from zero to one. To create distributions of pseudo-data the following procedure is followed in each channel:

- each β and δ is shifted by a random number drawn from a Gaussian distribution. The Gaussian is truncated at ± 1.25 to prevent the δ parameters to go too far in the linearly extrapolated region;
- the nominal templates are shifted according to the modified parameters;
- the total estimate is obtained by summing over the modified templates;
- new bin entries are drawn from a Poisson distribution with mean μ which is set, for each bin, to the original number of entries.

A pseudo-experiment (PE) consists in fitting the pseudo-data using the same templates used to fit the real data.
To evaluate the impact of a given systematic uncertainty on the cross section, two sets of PEs are performed: in one the δ representing the uncertainty under study is fixed to $+1$ and in the other to -1. In both cases a fit to the distribution of pseudo data is performed and the extracted β_0 is stored in a histogram. The same procedure is repeated 3000 times and as a last step the distribution of the fitted β_0 is fitted to a Gaussian to extract the mean value. The up and down deviations of the mean value obtained with the parameter δ_i fixed to ± 1 from the β_0 obtained in the nominal fit represents the systematic uncertainty contribution of the source i. The relative up and down deviations are added in quadrature to the other systematic uncertainties of the cross sections.
PEs are also used to evaluate the expected statistical and systematic uncertainties. The first one is defined as the standard deviation of the distribution of fitted β_0 obtained in a set of PEs without δ parameters. For the evaluation of the second one, a set of

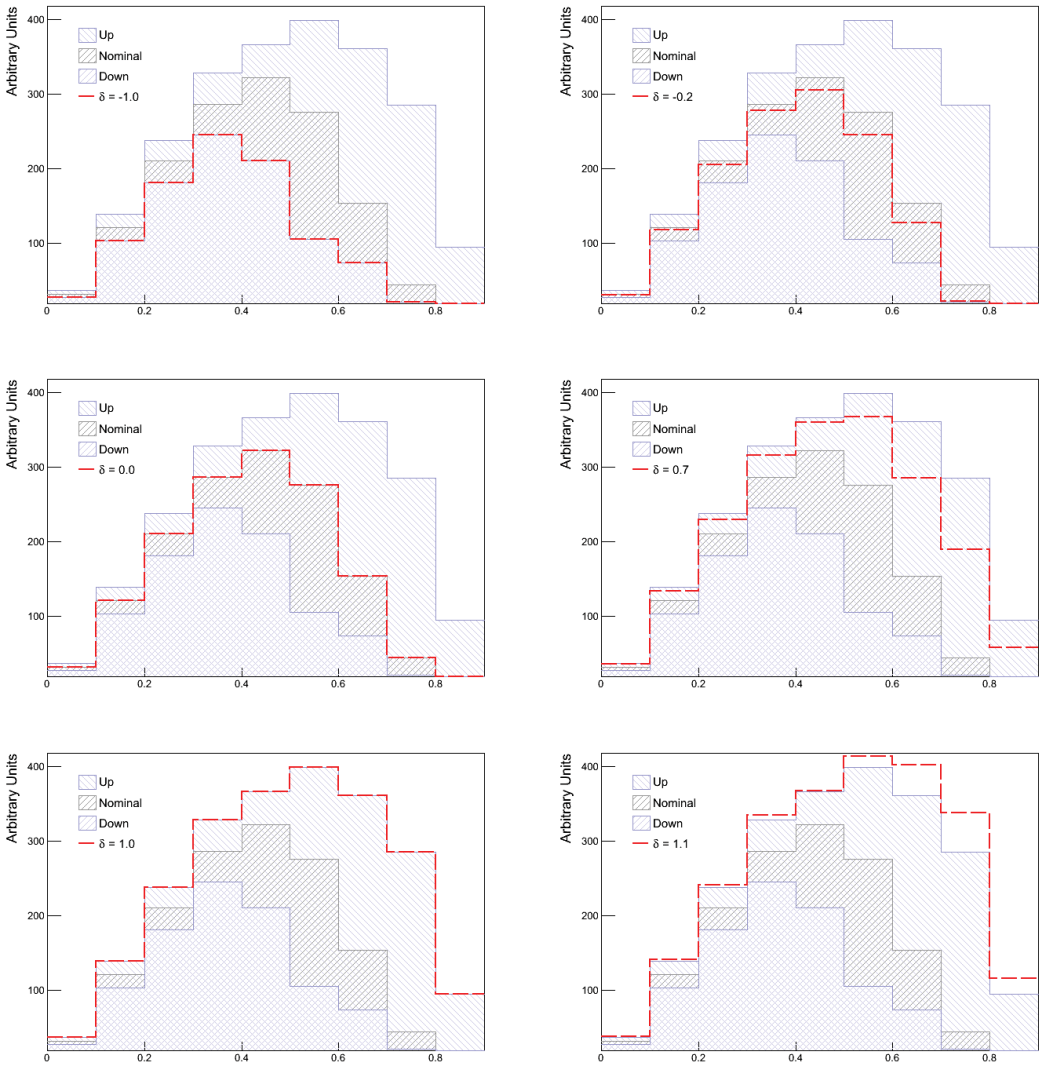

Figure 5.23: An illustration of template morphing as a function of δ inside and outside the region of quadratic interpolation. For $\delta \in [-1, +1]$, templates change shape ranging from the down to the up systematic template. In its default setup, $\delta = 0$ and the template coincides with the nominal case.

PEs is performed with all the δ parameters that are normally included in the fit. In this case, the estimate is obtained by quadratically subtracting the expected statistical uncertainty from the standard deviation of fitted β_0 distribution.
To evaluate the uncertainty stemming from the limited MC statistics of the templates PEs include Gaussian shifts of the bin entries prior to the shifts drawn from the Poisson distribution. For each bin, the Gauss function mean value is set to the bin content and its standard deviation to its statistical uncertainty. The Gaussian shifted bin entries are the new expectation values for the Poisson distributions. By quadratically subtracting the expected statistical uncertainty previously evaluated from the standard deviation of fitted β_0 values, an estimate of the uncertainty due to the limited MC statistics in the templates is obtained and added in quadrature to the uncertainty on the cross section.

5.4 Sources of the systematic uncertainties

The sources of systematic uncertainty affecting the $t\bar{t}$ cross section can be divided into two main categories: those affecting the single physics objects like leptons and jets stem from MC mismodeling and limited knowledge of the detector response. The second type comes from the choice of a model for the description of a physics process, like the choice of a given MC generator or data-driven technique. Because of their very different nature systematic uncertainties come in different forms: most of the object-based systematic uncertainty represent the one-stadard deviation of a parameter whose default value is used in the nominal analysis. These systematics are included in the fit and constrained directly from the data. On the other hand, most uncertainties falling in the second category must be evaluated by comparing the chosen model with another available one. In such cases the systematic uncertainties cannot be included in the fit due to their discrete nature and hence the impossibility of treating their δ-parameter as continuously varying in the range set by their symmetrized templeats.

5.4.1 Systematic uncertainties affecting the muons

Scale factors

The muon reconstruction, trigger and identification scale factors described in Section 4.1.2 are applied to all simulated processes. In the nominal analysis the central values of the three scale factors are multiplied and used to weigh each MC event passing the selection in the muon channel. To obtain templates representing the upper and lower one-standard deviation of these correction factors, the MC events are weighed with the nominal weights to which the combination[2] of the upper errors is added or from which the combination of the lower errors is subtracted.

[2]Using the standard error propagation law, the relative errors of the three scale factors are added in quadrature

Momentum scale and resolution

As mentioned in Section 4.1.2, the muon momentum in MC is scaled and smeared to match the momentum scale and resolution observed in data. Since the modification is performed before the muon selection, this procedure modifies the acceptance. The upper and lower one-standard deviations of the momentum smearing and scaling factors [3] are applied one at a time for the creation of systematic templates. In particular, the muon momentum components measured from the inner detector and the muon spectrometer are smeared up and down separately. The fitter takes as input two sets of templates encoding the (up and down) variation of the muon momentum scale and four sets encoding the (up and down) variation of the smearing factors of each momentum component.

5.4.2 Systematic uncertainties affecting the electrons

Scale factors

The MC events passing the electron-channel selection are weighted with the electron reconstruction, identification and trigger scale factors (Section 4.1.3). Analogously to the muon channel, these corrections are provided with the $\pm 1\sigma$ uncertainties which are combined separately and applied to the MC to obtain up and down systematic templates.

Momentum scale and resolution

Since the MC does not reproduce the data resolution, the electron momentum smearing is necessary for MC events (Section 4.1.3). The $\pm 1\sigma$ uncertainty associated to the smearing factors are applied one at a time to obtain up and down systematic templates. Energy scale corrections for electrons are applied to the data. The up and down systematic uncertainties of the scales are propagated to MC events.

5.4.3 Systematic uncertainties affecting the jets

Jet energy scale

As described in Section 2.3.3, the jets are calibrated with the EM+JES calibration scheme which employs the GEANT4 based full detector simulation and uses data-MC comparisons to derive the calibration constants. The uncertainty of this calibration is derived by the combination of the following sources:

- uncertainty in the calorimeter response to jets which is obtained from simulation studies and test-beam results of single particle response uncertainty. This uncertainty component is parameterized as a function of jet η and p_T and it is found to vary between 1.5% and 4 % [68];
- uncertainty due to mis-modeling of the signal-to-noise ratio of calorimeter cells in MC. Discrepancies between the simulated noise and the real noise in data leads

[3] The muon momentum smearing and scaling factors as well as their uncertainties are centrally provided in ATLAS.

to differences in the cluster shape and to the presence of fake topo-clusters (Section 2.3.3). The effect of this uncertainty component on jet response was studied thoroughly by e.g. reconstructing topo-clusters and thereafter jets in MC using the noise measured from data. The maximal observed change in jet response was found to be below 3% in the whole pseudorapidity range [68];

- uncertainty in the simulated description of detector material which affects the jet energy scale because the EM+JES calibration scheme relies on MC and therefore on the detector description. In order to estimate this uncertainty component, simulated detector geometries have been studied which include systematic variations of the amount of material based on test-beam as well as collision data measurements;

- uncertainty in the modeling of the fragmentation and the underlying event as well as the uncertainty in the choice of the MC event generator of the simulated samples used to derive the calibration constants. This is obtained by comparing the baseline PYTHIA samples to ALPGEN+HERWIG+JIMMY samples and to other PYTHIA samples generated with increased final state radiation [152];

- uncertainty due to the relative calibration of the jet energy scale in the end-cap and forward regions. The need of this calibration originates from the η-dependence of the jet calorimeter response due to the different technology used and the varying amount of dead material in front of the calorimeters. The relative calibration and its uncertainty are obtained by studying the transverse momentum balance of central and forward jets in di-jet events[4];

- uncertainty due to the presence of close-by jets. The systematic uncertainties outlined so far are obtained studying isolated jets. However, the realistic scenario for $t\bar{t}$ is characterized by a busy environment of multi-jet events. An additional uncertainty for non-isolated jets is derived from comparison of data and MC events and parameterized as a function of jet p_T and angular distance ΔR with the closest jet. It is found to be below 3% [66];

- uncertainty due to different calorimeter response to gluon-initiated and light-quark-iniatiated jets. The systematic uncertainties outlined so far are obtained studying inclusive jets. This uncertainty component takes into account the fact that jet fragmentation and showering properties are correlated with the flavor of the parton initiating the jet and can influence the calorimeter response. An additional term in the jet energy scale uncertainty is derived as described in [69] for event samples that have a different flavor content than the nominal MC simulation sample;

- uncertainty due to different calorimeter response to heavy-quark initiated jets. This uncertainty component is applied to all MC jets initiated by a b-quark. It was obtained studying systematic variations of the MC simulation. This uncertainty

[4]Exploiting the fact that, in di-jet events, the two jets are expected to have opposite transverse momentum due to transverse-momentum conservation

p_T [GeV]	Uncertainty (%)
20-40	2.50
40-80	2.00
80-210	1.70
210-600	1.10
>600	0.76

Table 5.3: Contribution to the jet energy scale uncertainty due to different calorimeter response to b-quark initiated jets. These numbers are centrally provided in ATLAS.

p_T [GeV]	$0 < \|\eta\| < 2.1$	$2.1 < \|\eta\| < 4.5$
20-50	5%	7%
50-100	2%	3%
>100	0%	0%

Table 5.4: Contribution to the jet energy scale uncertainty due to additional soft interactions in the same bunch crossing. These numbers are centrally provided in ATLAS.

is parameterized as a function of b-jet p_T and the values used in the analysis are listed in Table 5.3;

- uncertainty due to multiple soft interactions in the same bunch crossing (in-time pile-up) which produce additional energy deposits that are reconstructed within the jets. In the calibration of the jet energy scale, an average offset correction is calculated as described in Ref. [67] and applied to account for the average increase of jet energy due to pile-up. The uncertainty of this offset correction is parameterized as a function of jet η and p_T. The values used in the presented analysis are listed in Table 5.4.

The total jet energy scale uncertainty is derived (by a dedicated group of experts) by considering all the sources described above and it was evaluated on data collected in 2010, except for the contributions due to pile-up which was derived from studies of the 2011 data set and the b-jet scale uncertainty which was derived from MC in 2011. The final fractional jet energy scale systematic uncertainty for the sources evaluated in 2010 is shown in Figure 5.24, together with the individual contributions. The additional contributions due to the presence of pile-up and b-quark initiated jets are added in quadrature to it.
The up and down systematic templates for the jet energy scale uncertainty are created by adding and subtracting the total JES calibration uncertainty from the energy and momentum of all the jets before event selection. Since the individual components are considered together, the JES calibration uncertainty is assigned one δ-parameter in the fit.

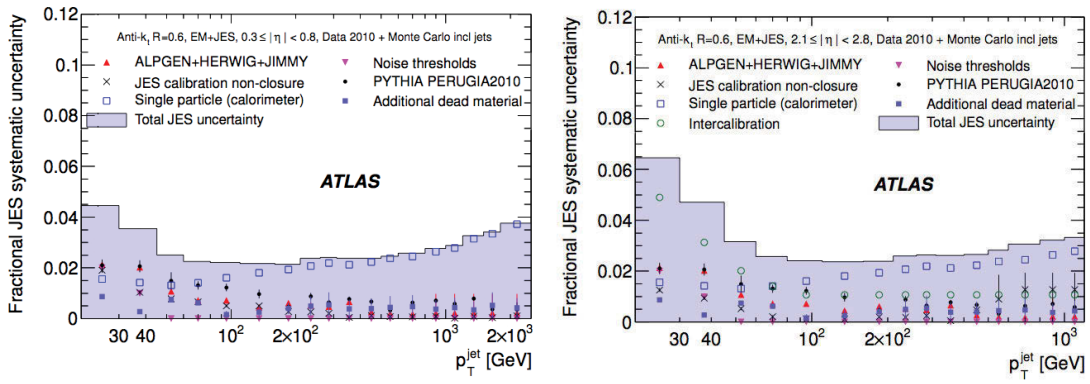

Figure 5.24: Fractional jet energy scale systematic uncertainty as a function of jet transverse momentum in the calorimeter barrel (left) and end-cap (right) [68].

Jet energy resolution

To study the systematic effect of the jet energy resolution on the $t\bar{t}$ cross section, the jet transverse momentum and energy in MC simulated events are smeared up and down before the event selection and systematic templates are created accordingly. The smearing factors are provided centrally in ATLAS [147].

Jet reconstruction efficiency

A systematic uncertainty is assigned to the jet reconstruction efficiency of the calorimeters. This was calculated by a dedicated group of experts with the Tag and Probe method applied to QCD di-jets events by matching jets reconstructed with the anti-k$_t$ algorithm seeded by selected tracks in the inner detector with jets reconstructed with the anti-k$_t$ algorithm seeded by topological clusters at the electromagnetic scale in the calorimeters [45]. The Tag and Probe efficiency was defined as the number of probe jets reconstructed by tracks and matched to calorimeter jets divided by the number of all probe track jets, given a tag jet reconstructed from tracks and matched to a calorimeter jet. In the analysis, jets are randomly discarded according to their reconstruction efficiency which is parameterized as a function of the transverse momentum and the pseudorapidity of their topological clusters. This uncertainty is by construction one-sided and therefore the "down" variation is created before the fit by symmetrizing the set of templates relative to it with the respect to the nominal templates.

5.4.4 Systematic uncertainties affecting the missing transverse energy

Soft-jet and cell-out uncertainty

As described in Section 2.3.5, the missing transverse energy is a function of the measured energy of all the physics objects produced in the event plus the energy of clusters that, after event reconstruction, are associated to none of the physics objects ($E^{CellOut}$ in

Equation 2.11). Each of these objects has an uncertainty related to its energy scale and resolution. Every time the energy of muons, electrons and jets is scaled or smeared for systematic studies, the missing transverse energy is corrected accordingly (Section 4.1.5). Therefore the uncertainty of the missing transverse energy stems explicitly only from the energy scale uncertainty of the topological clusters associated to soft jets ($E^{SoftJets}$ in Equation 2.11) and those not associated to any physics object. Clearly, these two sources of uncertainty are 100% anticorrelated (if the energy of the soft jets is scaled up, the remaining energy in the calorimeter has to be scaled down to ensure energy conservation and vice versa) and therefore they are both included in the same set of systematic templates. These uncertainties are provided centrally in ATLAS [73].

Pile-up uncertainty

The uncertainty related to additional energy deposits left in the calorimeters by events coming from secondary soft interactions occurring in the same or in neighboring bunch-crossings has to be treated 100% correlated with the soft-jet and cell-out uncertainties. The pile-up uncertainty is taken into account by adding to their up and down variations a flat 10% uncertainty, as agreed upon within the ATLAS collaboration. Given the technical complexity of implementing these three systematic uncertainties, the centrally-distributed tool which recalculates the missing transverse energy mentioned in Section 4.1.5 is also provided with functions that can handle their correct treatment.

LAr Hole

As described at the end of Section 3.3, a dead region in the liquid-argon electromagnetic calorimeter (LAr Hole) had to be simulated in the analysis to reproduce a hardware failure occurred during the data taking period in early 2011. The systematic uncertainty related to the presence of the LAr Hole is accounted for thanks to a dedicated software package distributed by the ATLAS collaboration and it is included in this analysis by means of an additional nuisance parameter in the fit.

5.4.5 Systematic uncertainties affecting the modeling of $t\bar{t}$ events

Signal generator

The uncertainty due to the choice of MC@NLO as nominal generator of $t\bar{t}$ events is studied by considering a second NLO generator: POWHEG. As discussed in Section 3.2.1, POWHEG is interfaced, like MC@NLO, with HERWIG/JIMMY thus isolating the effect of using an independent simulation of the hard partonic process. The systematic templates created using POWHEG can not be symmetrized because of the non-continuous nature of this source of uncertainty. Its effect is addressed by obtaining the shift in the $t\bar{t}$ cross section by means of running pseudo-experiments as described in Section 5.3.1.

Hadronization

An uncertainty is assigned to the usage of the hadronization model provided by HERWIG/JIMMY (Section 3.2.1) in the nominal $t\bar{t}$ samples. Since the nominal generator of the hard process MC@NLO can only be interfaced with HERWIG/JIMMY, POWHEG samples interfaced with PYTHIA are employed to generate systematic templates which have to be scaled to the difference between MC@NLO and POWHEG when both interfaced with HERWIG/JIMMY. After running pseudo-experiments, the relative shift in the cross section with respect to the nominal value is quoted as systematic uncertainty.

Initial and final state radiation

In Section 3.2.1 it was described how $t\bar{t}$ samples with increased and decreased initial and final state radiation are generated with AcerMC and PYTHIA to allow systematic studies. The templates obtained with these samples are normalized to the bin-by-bin ratio between templates obtained with an AcerMC sample with nominal amount of initial and final state radiation and the default MC@NLO templates. These systematic sources arise from the variation of model parameters that are continuous as they represent or multiply the energy scales controlling the physics process. Therefore the initial and final state variation templates are included in the fit with individual parameters.

5.4.6 Systematic uncertainties affecting the background processes

W+Jets shape

The impact of the variation of the most relevant ALPGEN parameters on W+Jets events is studied by means of weights derived by comparing kinematic distribution obtained at generator level using different settings. The most significant ALPGEN parameters have been found to be the functional form of the factorization scale (*iqopt*) and the transverse momentum threshold for parton matching (*ptjmin*). More details about these parameters can be found in [131]. The event weights are centrally provided by the ATLAS collaboration. These are discrete sources of uncertainty and therefore they are evaluated outside the fit by means of pseudo-experiments.

QCD shape

A second QCD estimate obtained with a different data-driven model can be used in both channels to estimate the uncertainty in the shape of the QCD background templates. In the electron channel, a method sometimes called *cut-reversal* or *anti-electron* method is used in which the QCD contribution is estimated in a side-band region characterized by $E_T^{Miss} < 35$ GeV and an electron selection similar to the one described in Section 4.1.3 but with some identification requirements inverted with respect to the standard ones. A template fit to data which also includes the contribution of $t\bar{t}$, W/Z+Jets, single top and di-boson production is performed to obtain the best QCD normalization which is then extrapolated into the signal region. A data sample containing the QCD estimate relative

to the data set considered for the analysis presented and obtained with this alternative method is centrally provided.

In the muon channel, the largest difference between the average estimate and either of the two matrix-method implementations described in Section 4.3.2 is used as shape systematic uncertainty as agreed upon in the ATLAS Top Working Group. The QCD shape uncertainty is evaluated outside the fit by means of pseudo-experiements.

5.4.7 Background normalization

Uncertainties in the predictions of the background processes are accounted for with the use of the β parameters that drive their normalization in the fit.
As stated before, there is a total of six β parameters for the normalization of W+Jets. As a function of jet multiplicity, they are assigned increasing Gaussian constraints: 42% in the 3-jet channel, 48% in the 4-jet channel and 54% in $>$ 4-jet channel. Their magnitudes are motivated by the theoretical uncertainty of 4% on inclusive W+Jets production combined with the uncertainty of the theoretical "Berends scaling" hypothesis that the ratio of $W + n$ jets to $W + (n + 1)$ jets is expected to be approximately constant as a function of n [30, 82]. The number of W events in the n-jet sample can thus be estimated as:

$$N_W^{n-jet} = N_W^{2-jet} \cdot \sum_{i=2}^{n} \left(\frac{N_W^{2-jet}}{N_W^{1-jet}} \right)^i \tag{5.18}$$

The scaling-assumption validity is affected by an irreducible systematic uncertainty which, based on the results in [16] for the predictions of the ratio $W + (n + 1)/W + n$ from different MC generators and generator settings at parton level, was found to be 24%. Although the same argument holds for Z+Jets, this background is rather small and its overall normalization is constrained to 30%.
For di-boson and single top production, the uncertainty on their theoretical cross sections, which is 10% and 5% respectively, added in quadrature to the uncertainty on the luminosity, is used.
Lastly the six normalization parameters employed for QCD are given Gaussian constraints which reflect the uncertainty of the data-driven technique used to estimate this background, which is 50%.

5.4.8 Luminosity calibration

The calibration of the ATLAS luminosity scale is based on *van der Meer* scans [160]. The systematic uncertainty on the luminosity calibration is measured as described in Ref. [70] and it was found to be 3.7%.

5.5 Results

A first fit which includes only the normalization parameters is performed and the cross section extracted is:

$$\sigma_{t\bar{t}} = 179.72^{+3.80}_{-3.78}\,\text{pb}. \tag{5.19}$$

Since the systematic uncertainties are not considered, the errors in Equation 5.19 are to be interpreted as the statistical uncertainty of the cross section [5]. The values of the β parameters preferred by the fit are listed in Table 5.5: they suggest that the predictions for W+Jets overestimate this background in all channels (their best value is consistently smaller than one). The errors for β_0 extracted in the fit can be compared with the expected statistical uncertainty obtained in a series of PEs as described in Section 5.3.1 which, as Figure 5.25 shows, is of the same order. The data-MC comparison after the fit is shown in Figure 5.26: this is the 120-bin histogram that the fitter creates before the fit by placing the templates of different channels side-by-side scaled by the value of the β_i evaluated in the fit. The ratio between data and normalized MC predictions is plotted at the bottom of this figure.
The fit is also performed in the electron and the muon channel separately. In the electron channel the cross section extracted is:

$$\sigma_{t\bar{t}} = 173.94^{+6.37}_{-6.33}\,\text{pb} \tag{5.20}$$

and in the muon channel:

$$\sigma_{t\bar{t}} = 182.75^{+4.65}_{-4.63}\,\text{pb}. \tag{5.21}$$

The larger statistical error reflects the fewer data available in each of the two channels compared to the combined one: the statistics available in the electron channel is particularly small due to the tighter selection criteria. Both measurements agree with the combined one within their uncertainties.

The inclusion in the likelihood function of the δ parameters assumed to be continuous yields the cross section:

$$\sigma_{t\bar{t}} = 178.91^{+6.71}_{-6.33}\,\text{pb}. \tag{5.22}$$

The uncertainty in Equation 5.22 is the statistical one combined with the uncertainty stemming from the systematic sources included in the fit. To isolate the contribution of the systematic uncertainty only, the relative statistical uncertainty is quadratically subtracted from the relative combined one. A contribution of about 3% is found, which agrees with the expected systematic uncertainty from the fit estimated in a series of PEs that included the δ parameters. This can be seen from the standard deviation of the Gaussian distribution of fitted β_0 values shown in Figure 5.27 (left) from which the expected statistical uncertainty has to be quadratically subtracted. On the right-hand side of Figure 5.27, the pull of β_0 is shown, defined as the difference between the fitted β_0 from each PE and β_0 from the nominal fit, normalized to the uncertainty of the fitted

[5] The uncertainty in the total luminosity, which is 3.7%, is never included until explicitly specified.

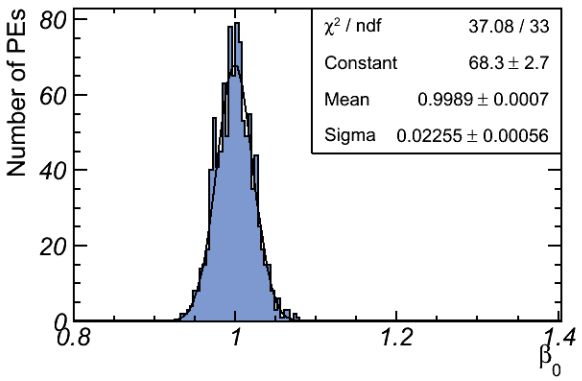

Figure 5.25: Distribution of fitted $t\bar{t}$ cross sections obtained in a series of 1000 PEs without δ parameters. The standard deviation of this distribution is taken as the a-priori statistical uncertainty.

Parameter	Value	Error	Error Up	Error Down
$\beta(t\bar{t})$	1.0921	0.0226	0.0231	-0.0230
β(W$\rightarrow \mu$ + 3 jets)	0.9513	0.0341	0.0372	-0.0374
β(W$\rightarrow \mu$ + 4 jets)	0.8476	0.0663	0.0759	-0.0760
β(W$\rightarrow \mu$ + 5 jets)	0.9405	0.1141	0.1223	-0.1219
β(W$\rightarrow$ e + 3 jets)	0.9961	0.0418	0.0464	-0.0466
β(W$\rightarrow$ e + 4 jets)	0.8328	0.0690	0.0751	-0.0754
β(W$\rightarrow$ e + 5 jets)	0.8083	0.0842	0.0891	-0.0891
β(Z+Jets)	1.0015	0.2373	0.2584	-0.2565
β(Single top)	1.0085	0.1055	0.1059	-0.1058
β(Diboson)	1.0038	0.0620	0.0620	-0.0620
β(QCD in μ + 3 jets)	1.2623	0.2021	0.2172	-0.2168
β(QCD in μ + 4 jets)	0.9170	0.3583	0.4063	-0.4067
β(QCD in μ + 5 jets)	0.8972	0.4083	0.4337	-0.4349
β(QCD in e + 3 jets)	0.5421	0.2013	0.2183	-0.2173
β(QCD in e + 4 jets)	1.1856	0.2964	0.3171	-0.3154
β(QCD in e + 5 jets)	0.5018	0.3912	0.4074	-0.4065

Table 5.5: Best values and uncertainties of the β parameters in a fit without δ parameters.

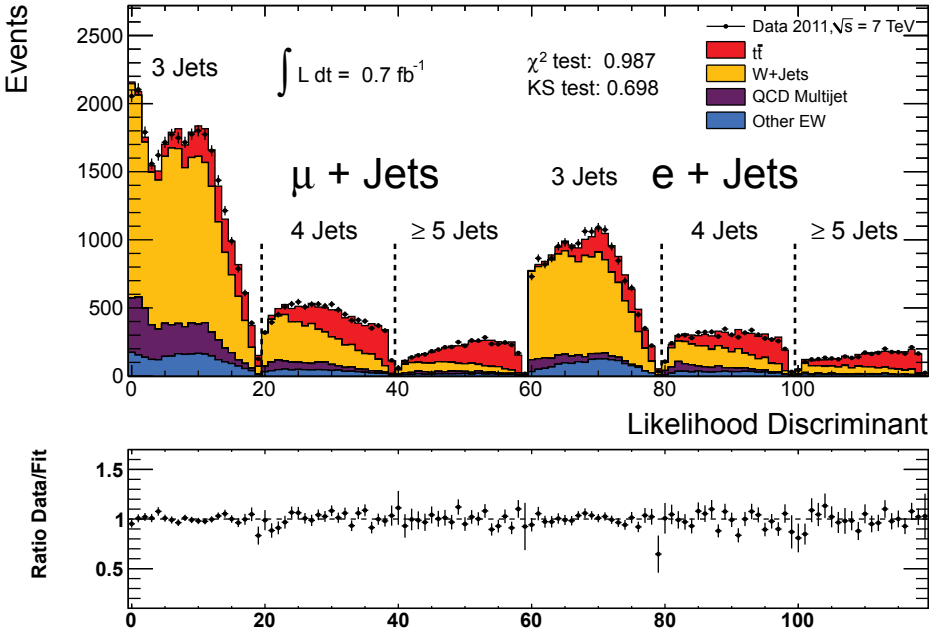

Figure 5.26: Data-MC comparison after a fit which includes only the normalization parameters β of the six physics processes.

β_0. For the uncertainty to be reliable, the pull distribution is expected to be consistent with a unit normal distribution, which is verified in Figure 5.27.
Figure 5.28 shows the data-MC comparison after the fit. From the values of the χ^2 and Kolmogorov statistical tests of compatibility printed in Figure 5.26 and Figure 5.28 we see that the presence of morphing parameters allows the fit to adjust the shape of the templates and to achieve a higher data-MC agreement. The best values of all the fit parameters included in the fit are listed in Table 5.6. The normalization of W+Jets is now closer to unity. This implies that the previous apparent overestimate of this source was a result of shape distortion that a fit without morphing parameters could not compensate. The values of the δ parameters are small, i.e. within their one standard deviation, but for some of them the uncertainty is large suggesting that the fit cannot constrain them very well. This situation arises for nuisance parameters to which the likelihood only has little sensitivity and thus the magnitude of that systematic uncertainty is dominated by the external uncertainty provided by the systematic templates [161]. If the likelihood function is sufficiently sensitive to some particular δ parameter, the fit to the data provides a stronger in-situ constraint. This reduction of uncertainty is the essential strength of parameterized likelihood fits. As an illustrative example it is worth noting that δ(JES) has a smaller uncertainty implying that the fit has sufficient sensitivity to this systematic uncertainty and can constrain it beyond the a priori uncertainty. The sensitivity of the fit to the jet energy scale comes from the relative normalization of the three different jet multiplicity bins as well as the inclusion of the leading jet p_T as discriminating variable.

The negative logarithm of the profile likelihood ratio [76] is shown in Figure 5.29: this function is smooth in a large range, with a minimum at the expected value of β_0 and no other critical points. In the same figure it is possible to see a zoom of the minimum showing the points at which the errors of β_0 are defined.
The cross section extracted in the electron channel when the systematic uncertainties are considered is:

$$\sigma_{t\bar{t}} = 172.44^{+9.20}_{-8.88}\,\text{pb}. \tag{5.23}$$

and in the muon channel:

$$\sigma_{t\bar{t}} = 185.45^{+8.88}_{-8.48}\,\text{pb}. \tag{5.24}$$

As before, the measurements in the individual channels agree with the combined one. The morphing parameters δ in the three scenarios are displayed in Figure 5.30. The values show that the fitter prefers to morph the templates of the two separate channels in a slightly different way, with the combined case often being a compromise. In particular, it seems that the degrees of freedom offered by the final state radiation and the soft jet systematic templates are used to morph the templates of the electron and the muon channel in different "directions" when they are fitted separately, probably to cover distinct shape discrepancies in the individual channels.
It is useful to study the sources of systematic uncertainty in more details by isolating their individual contributions. This is done by performing a fit in which the systematic source under study is kept fixed at the value found by the nominal fit: the uncertainty in the cross section calculated by the fit in this case is the combination of the statistical uncertainty with all the other systematic sources. Hence, the quadratic subtraction of the relative total uncertainty and the relative uncertainty without a given δ_i is an estimate of the contribution of the systematic source i to the total uncertainty. The individual contributions of all systematic sources obtained as described above are listed in Table 5.7. It is worth noting that these contributions do not add up to the total uncertainty returned by the fit. This is expected since this procedure does not take into account parameter correlations that manifest themselves in the fit.
The contribution from the sources which are not included in the fit is evaluated as described in Section 5.3.1 and listed in the lower half of Table 5.7. These are added in quadrature to the total systematic uncertainty from the fit to give a total systematic uncertainty for the cross section measurement of about 5%. Finally, the uncertainty in the total luminosity, which is 3.7%, is added in quadrature to the combined statistical and total systematic uncertainty. The final result for the total production cross section of $t\bar{t}$ pairs decaying in the single lepton channel is thus:

$$\sigma_{t\bar{t}} = 178.9^{+3.8}_{-3.8}(\text{stat.})^{+9.5}_{-9.1}(\text{syst.})^{+6.6}_{-6.6}(\text{lumi})\ \text{pb} = 178.9^{+12.2}_{-11.8}\ \text{pb}. \tag{5.25}$$

The cross section obtained agrees very well with the measurement presented in [71]. While the central values and their total uncertainty are comparable to each other, some systematic sources give a different contribution. Table 5.8 summarizes the individual contributions of systematic uncertainty to the cross section in both analyses: here the sources belonging to the same object or model have been combined to give one total

contribution. The uncertainty in the cross section stemming from uncertainties in electrons and muons are comparable with those presented in [71]. The different contribution of the systematic uncertainty coming from the jets may be attributed to the different treatment of the jet energy scale uncertainty. In this analysis the effect of this uncertainty has been parameterized with one nuisance parameter in the likelihood function: δ(JES). This treatment is usually not satisfactory for compound systematic sources like the jet energy scale which, as described in Section 5.4.3 receives contributions from multiple different sources. The reason is that in such cases opposite miscalibrations from individual sources (e.g. the miscalibration of one source tends to overestimate the jet energy scale and another one to underestimate it) may have a net null effect when the two sources are moved together up and down in a rigid way leading to an overconstrain of the global uncertainty [161]. A cure to this would be to add flexibility to the model by splitting JES into uncorrelated sources that can effectively be described by a nuisance parameter. This gives more degrees of freedom to the fit who will be free to constrain the individual contributions from the data. This is the approach adopted in [71] where JES has been split in 10 different components which accounted separately for the uncertainty in the jet calorimeter response, in the pseudorapidity dependence of the calibration, in the modeling of jets, pile-up and the underlying event and in the calorimeter response to light and heavy jet composition.
However, in October 2011 it was argued by the ATLAS physics coordination that the JES uncertainties available for the analyses in Athena release 16 using data collected in 2011 were not suited for a dissection: the fact that these corrections are evaluated on 2010 data for a rather different experimental scenario with a lower cluster threshold, a larger bunch spacing and less critical pile-up conditions render the use of the single components meaningless on 2011 data. The ATLAS physics coordination thus encouraged the use of the combined corrections supported by in-situ techniques.
To the purpose of understanding whether or not the use of a single nuisance parameter for the jet energy scale uncertainty brings realistic results, its expected systematic uncertainty is evaluated by means of PEs and found to be +1.9% and –2.4%[6], i.e. larger than the profiled results, suggesting that the uncertainty on δ(JES) is to some extent underestimated in the fit. Given the care needed for the treatment of this specific systematic source, a conservative approach is due and the nominal measurement becomes the one with the jet energy scale uncertainty evaluated outside the fit. As Table 5.7 shows, this does not provide a new central value but only an increased systematic uncertainty stemming from the use of the larger jet energy scale expected uncertainty from PEs. Therefore the central result of this chapter becomes:

$$\sigma_{t\bar{t}} = 178.9^{+3.8}_{-3.8}(\text{stat.})^{+10.1}_{-9.8}(\text{syst.})^{+6.6}_{-6.6}(\text{lumi})\ \text{pb} = 178.9^{+12.3}_{-12.4}\ \text{pb}. \tag{5.26}$$

Finally the last and perhaps more striking differences between this analysis and the one presented in [71] are in the contributions of the generator and hadronization models. In both analyses they have been evaluated outside the fit by means of PEs. However, in [71],

[6]The values are obtained after subtraction of the expected statistical uncertainty. The total relative systematic uncertainty associated to jets now becomes +2.1% and –2.5%.

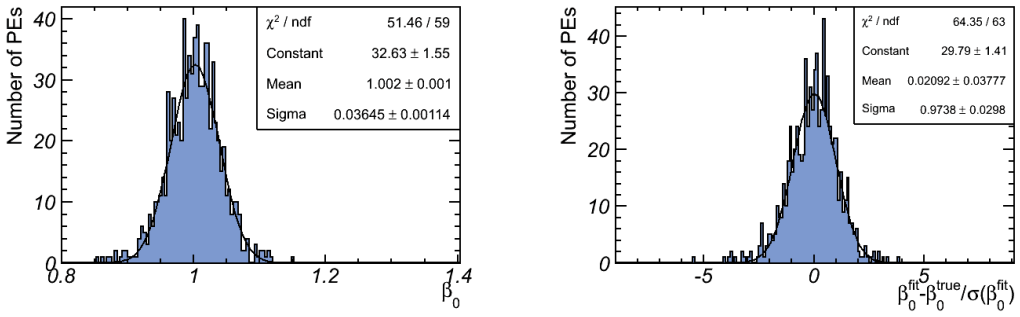

Figure 5.27: Distribution of fitted $t\bar{t}$ cross sections (left) obtained in a series of 1000 PEs with δ parameters. The standard deviation of this distribution is taken as the a-priori statistical uncertainty combined with the expected contribution of the systematic uncertainties included in the fit. On the right, the pull of β_0 is shown.

half of the difference in the cross section extracted for $\delta_i = +1$, with i being the source evaluated outside the fit, and the nominal one is quoted as symmetrized uncertainty. The measured cross section will be compared with two theoretical predictions in the next chapter.

Parameter	Value	Error	Error Up	Error Down
$\beta(t\bar{t})$	1.0871	0.0391	0.0407	-0.0384
β(W$\rightarrow \mu$ + 3 jets)	0.9810	0.0474	0.0497	-0.0496
β(W$\rightarrow \mu$ + 4 jets)	0.9189	0.0930	0.0978	-0.0973
β(W$\rightarrow \mu$ + 5 jets)	0.9735	0.1445	0.1505	-0.1460
β(W$\rightarrow$ e + 3 jets)	1.0581	0.0577	0.0616	-0.0606
β(W$\rightarrow$ e + 4 jets)	0.9155	0.0937	0.0982	-0.0960
β(W$\rightarrow$ e + 5 jets)	0.8774	0.1240	0.1284	-0.1244
β(Z+Jets)	0.9850	0.2483	0.2678	-0.2678
β(Single top)	0.9951	0.1064	0.1065	-0.1064
β(Diboson)	1.0019	0.0620	0.0620	-0.0620
β(QCD in μ + 3 jets)	1.3083	0.2532	0.2784	-0.2864
β(QCD in μ + 4 jets)	0.8431	0.3595	0.4084	-0.4077
β(QCD in μ + 5 jets)	0.9432	0.4144	0.4404	-0.4421
β(QCD in e + 3 jets)	0.5458	0.2531	0.2648	-0.2771
β(QCD in e + 4 jets)	1.1320	0.3011	0.3228	-0.3231
β(QCD in e + 5 jets)	0.5152	0.3949	0.4145	-0.4109
δ(JES)	-0.2181	0.1674	0.1614	-0.1352
δ(Jet Efficiency)	-0.1688	0.8836	0.8778	-0.8860
δ(JER)	0.1233	0.1010	0.0912	-0.0995
δ(FSR)	-0.1813	0.3432	0.3986	-0.2916
δ(ISR)	0.2291	0.2197	0.2086	-0.2301
δ(μ SFs)	0.4090	0.8274	0.8250	-0.8041
δ(μ Energy Scale)	-0.4560	1.2534	1.2391	-1.1219
δ(μ Momentum Smearing at MS)	0.0917	0.9432	0.8249	-0.9602
δ(μ Momentum Smearing at ID)	0.7590	0.5773	0.4914	-0.6616
δ(e SFs)	-0.4126	0.9155	0.8996	-0.9073
δ(e Resolution Smearing)	0.4378	0.4725	0.4478	-0.4747
δ(e Energy Scale)	-0.0663	0.3212	0.3208	-0.3137
δ(Missing E_T LAr)	-0.1923	0.5770	0.5943	-0.5798
δ(Missing E_T SoftJet)	0.5739	0.3717	0.3240	-0.4207
δ(MC Generator)	n/a	n/a	n/a	n/a
δ(Hadronization)	n/a	n/a	n/a	n/a
δ(W+Jets Shape iqopt3)	n/a	n/a	n/a	n/a
δ(W+Jets Shape ptjmin10)	n/a	n/a	n/a	n/a
δ(QCD Shape)	n/a	n/a	n/a	n/a

Table 5.6: Best values and uncertainties of the β and δ parameters calculated by the fit. The last five sources are not available because they are evaluated outside the fit.

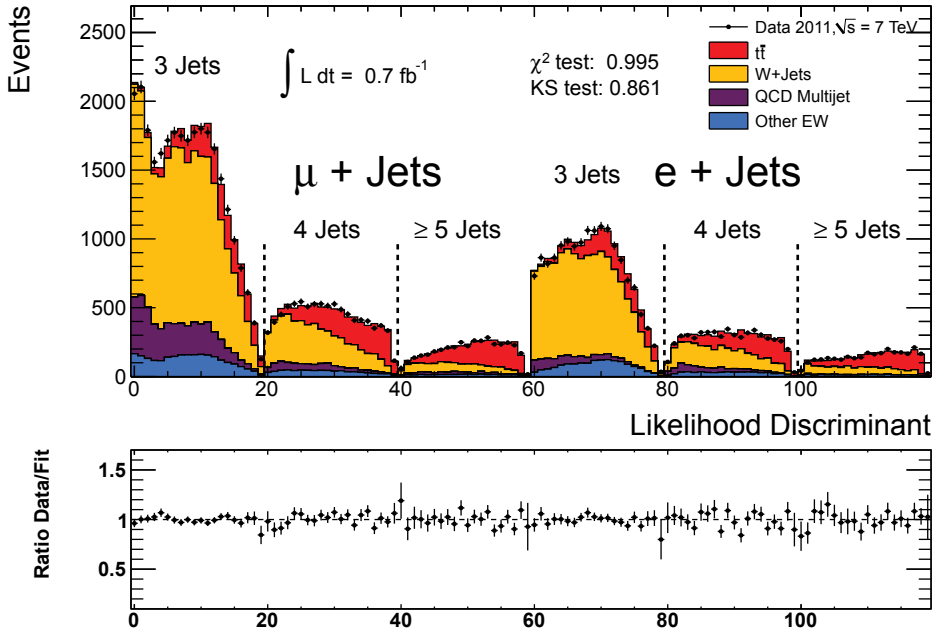

Figure 5.28: Data-MC comparison after a fit which includes the normalization parameters β of the six physics processes and the morphing parameters δ of the systematic uncertainties included in the fit.

	$\sigma_{t\bar{t}}$	**Up (pb)**	**Down (pb)**	**Up (%)**	**Down (%)**	$\sqrt{\Delta^2_{up}}$ (%)	$\sqrt{\Delta^2_{down}}$ (%)
Nominal	178.91	6.71	6.33	3.75	3.54		
No Systematics	179.72	3.80	3.78	2.11	2.10		
No JES	178.90	6.17	5.87	3.45	3.28	1.47	1.32
No JEF	178.89	6.68	6.31	3.73	3.53	0.35	0.28
No JER	178.86	6.56	6.18	3.67	3.46	0.78	0.76
No FSR	178.82	6.11	5.79	3.42	3.24	1.55	1.43
No ISR	178.85	6.64	6.27	3.71	3.51	0.53	0.48
No Muon SF	178.89	5.59	5.03	3.12	2.81	2.07	2.15
No Muon Energy Scale	178.86	6.66	6.28	3.72	3.51	0.45	0.44
No Muon MS Smearing	178.90	6.70	6.32	3.74	3.53	0.21	0.20
No Muon ID Smearing	178.86	6.65	6.26	3.72	3.50	0.49	0.52
No Electron SF	178.84	6.00	5.68	3.35	3.18	1.68	1.56
No Electron Smearing	178.90	6.65	6.31	3.72	3.53	0.50	0.28
No Electron Energy Scale	178.87	6.68	6.29	3.73	3.52	0.35	0.39
No MET Soft Jet	178.84	6.63	6.25	3.71	3.49	0.57	0.55
No MET Lar Hole	178.92	6.64	6.29	3.71	3.52	0.54	0.40
Sum from fit						3.76	3.59
MC Generator				2.66	1.99		
Hadronization				2.81	3.10		
QCD Shape				0.54	0.71		
W+Jets Shape (iqopt3)				0.33	0.57		
W+Jets Shape (ptjmin10)				0.15	0.15		
bin-by-bin				1.78	1.78		
Sum additional				4.31	4.19		
Systematic uncertainty from fit				3.10	2.85		
Total systematic uncertainty		9.49	9.07	5.31	5.07		
Luminosity		6.62	6.62	3.70	3.70		
Total		12.18	11.84	6.81	6.62		

Table 5.7: Individual contributions of the systematic uncertainties included in the fit. In the lower half, the contributions from the external sources evaluated by means of PEs and from the uncertainty in the total luminosity are listed.

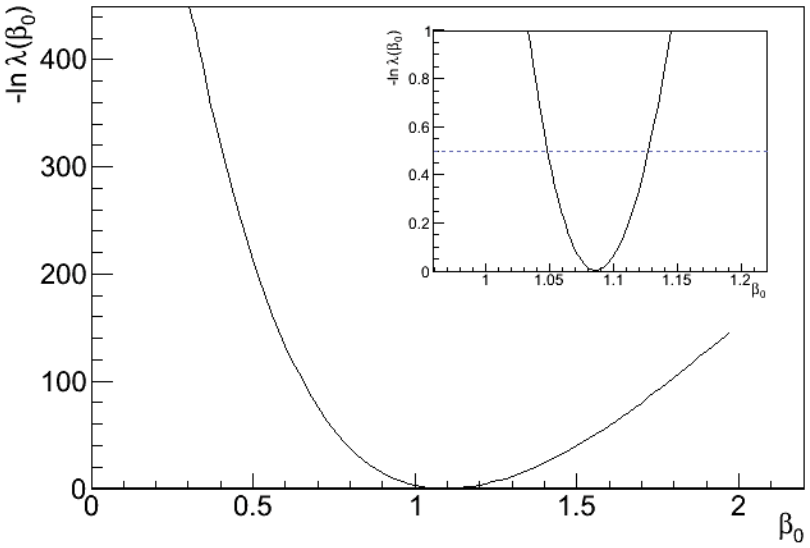

Figure 5.29: Negative logarithm of the profile likelihood ratio of the full fit as a function of the $t\bar{t}$ cross section parameter. The line in the zoomed region indicates where the errors are defined.

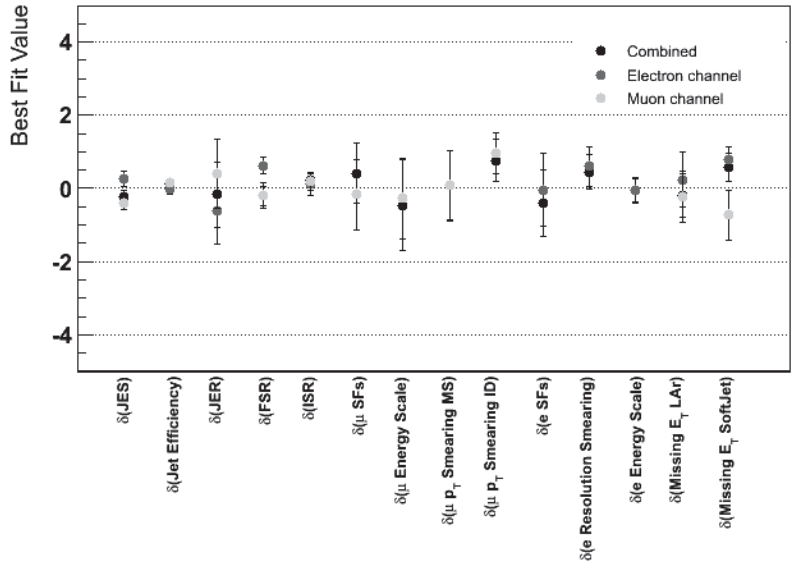

Figure 5.30: Best values of the δ parameters in the combined fit and in the electron and muon channel separately.

Source	This work		Presented in [71]	
	Up (%)	Down (%)	Up (%)	Down (%)
Jets	1.7	1.5	1.8	2.4
Muons	2.2	2.3	2.3	2.3
Electrons	1.8	1.6	1.5	1.7
E_T^{Miss}	0.8	0.7	1.1	0.9
Generator	2.7	2.0	3.0	3.0
Hadronization	2.8	3.1	0.5	0.5
ISR/FSR	1.6	1.5	1.7	1.3
QCD Shape	0.5	0.7	0.4	0.4
W Shape	0.4	0.6	0.5	0.5

Table 5.8: Comparison of relative individual contributions to the total systematic uncertainty presented in this work and in [71].

6 Extraction of the top quark mass

The six quark flavors of the SM are arranged in three generations of very different mass scales (Table 1.1). In QCD, they are also typically divided into *light* and *heavy* flavors depending on whether their mass m_{Q} is smaller or larger than Λ_{QCD}: if $m_{\mathrm{Q}} \lesssim \Lambda_{\mathrm{QCD}}$ then the flavour is light, while for $m_{\mathrm{Q}} \gg \Lambda_{\mathrm{QCD}}$ it is heavy. In applications of hadron physics, u, d and s are light and they can be treated as massless [1]; c, d and t quarks are heavy and their mass can not be neglected [2].
The mass m_Q of a heavy quark, therefore, is a key parameter in the heavy quark theory. However, since the quarks can not be observed directly, there exists no natural definition for m_Q and theoretical consistency and convenience are the only guiding principles. The first suggestion was, in analogy with quantum electrodynamics, the position of the pole in the free quark propagator. It slowly turned out that this mass concept in QCD is ill-defined as it does not allow a consistent inclusion of non-perturbative corrections. New quark mass definitions were subsequently employed to allow for a stable extraction of the quark mass parameter.
This chapter is organized as follows: in Section 6.1 the ambiguous concept of quark mass in QCD is briefly discussed. In Section 6.2 the most common approaches to measure the mass of the top quark experimentally are mentioned. Finally, Section 6.3 presents the methods used in this analysis and the extraction of two theoretical top quark mass parameters from the total $t\bar{t}$ production cross section.

6.1 The concept of quark mass

6.1.1 The problem of the pole mass in QCD

In low-energy quantum electrodynamics, there is an obvious candidate for the mass m_e of an isolated electron (or, in general, a non-colored elementary particle): this is given by the position of the pole in the electron propagator. The mass m_e is gauge-invariant and experimentally measurable. The equivalent definition of quark mass in QCD was introduced in [142] and it is called "pole mass" (m_Q^{pole}). Explicit perturbative calculations show that, like m_e, it is a gauge invariant quantity [156, 97, 42, 89]. However, quarks are confined inside hadrons by the strong interaction and do not exist as isolated particles. Unlike m_e, therefore, the quark pole mass can not be directly measured and exists only as a theoretical construction.

[1] The mass of the quark s is about 150 MeV and thus only a little smaller than Λ_{QCD} but the corrections to the light SU(3) symmetry are reasonably small and the assumption is justified.
[2] There is an error associated with the fact that $m_c \approx 1.5$ GeV may not be very close to the asymptotic limit $m_c \gg \Lambda_{\mathrm{QCD}}$. See, for example, [86] for an estimation of this error.

Despite this, the quark pole mass still represents a valid candidate in perturbative QCD: the fact that it is well defined in each finite order of perturbation theory and that it is introduced in a gauge invariant way made it, at first, a very popular choice. However, as one attempts to determine m_Q^{pole} to arbitrary high accuracy, divergent terms appear in the perturbative series: infrared contributions lead to an intrinsic uncertainty in the pole mass of order Λ_{QCD}. The source of this uncertainty is discussed in [39] (see also [38]) and summarized below.
The free quark propagator in perturbation theory is:

$$G(p) = \frac{1}{m_Q(\mu) - \not{p}}, \tag{6.1}$$

where μ is the energy scale at which we are calculating the observable quantities and the running mass $m_Q(\mu)$ is the parameter entering the effective QCD Lagrangian $\mathcal{L}(\mu)$. $G(p)$ has a pole at $p^2 = m_Q^2(\mu)$ and therefore it describes a particle with mass $m_Q(\mu)$. The first order in α_s accounts for the exchange of a gluon (represented by the diagram in Figure 6.1 without internal "bubbles") and the pole moves to $p^2 \simeq (m_Q(\mu) + \mu \cdot 4\alpha_s/3\pi)^2$ describing now a particle with mass $m_Q^{(1)} = m_Q(\mu) + \mu \cdot 4\alpha_s/3\pi$, which differs from the mass in the Lagrangian $m_Q(\mu)$. In any given order of perturbation theory, the pole position shifts and so does the mass of the corresponding particle. The relation between the pole mass and the running mass can be written in the following form:

$$m_Q^{(k)} = m_Q(\mu) \sum_{n=0}^{k} C_n \left(\frac{\mu}{m}\right) \left(\frac{\alpha_s(\mu)}{\pi}\right)^n, \quad C_0 = 1 \tag{6.2}$$

and it clearly depends on the order k of perturbation theory one considers. The problem lies in the fact that the sum in Equation 6.2 does not converge to a reasonable number. As described in [39], there may be more than one reason for the divergence to exist but it is easy to identify a particular source in the so-called infrared renormalon singularity in the perturbative expansion of the pole mass. As shown there, the mass shift is formulated formally in perturbation theory (in the limit of large m_Q compared to the gluon virtual momentum k) by:

$$\delta m_Q = m_Q^{pole} - m_Q(\mu) = \frac{8\pi}{3}\alpha_s \int \frac{d^3k}{(2\pi)^3} \frac{1}{\vec{k}^2}. \tag{6.3}$$

with an ultraviolet cut-off in the k integration implied at μ.
Summing over all the bubbles in Figure 6.1, is equivalent to replacing α_s by the running coupling $\alpha_s(\vec{k}^2)$:

$$\delta m_Q = \frac{8\pi}{3} \int_{|\vec{k}|<\mu} \frac{d^3k}{(2\pi)^3} \frac{\alpha_s(\vec{k}^2)}{\vec{k}^2}. \tag{6.4}$$

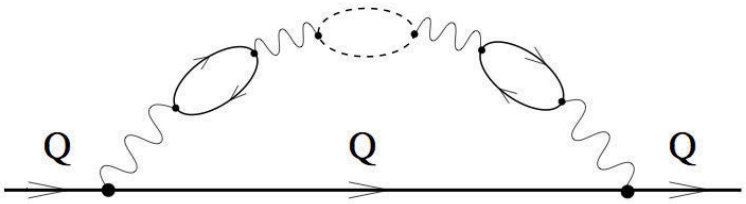

Figure 6.1: Perturbative diagrams leading to the renormalization of the heavy quark mass. The number of bubble insertions into the gluon propagator can arbitrarily generate corrections in all orders of α_s.

By expanding $\alpha_s(\vec{k}^2)$ in a power series in $\alpha(\mu^2)$:

$$\alpha_s(\vec{k}^2) = \frac{\alpha_s(\mu^2)}{1 - (b\alpha_s(\mu^2)/4\pi)\ln(\mu^2/\vec{k}^2)} = \alpha_s(\mu^2)\sum_{n=0}^{\infty}\left(\frac{b\alpha_s(\mu^2)}{4\pi}\ln\frac{\mu^2}{\vec{k}^2}\right)^n \tag{6.5}$$

where $b = 11/3\,N_c - 2/3\,n_f$, Nc is the number of colors and n_f is the active number of quark flavors at the scale μ, the following series is obtained:

$$\delta m_Q = \frac{4\alpha_s(\mu)}{3\pi}\mu\sum C_n\left(\frac{b\alpha_s(\mu)}{4\pi}\right)^n \tag{6.6}$$

where the coefficients C_n are given by:

$$C_n = \int_0^1 dx\left(\ln\frac{1}{x^2}\right)^n. \tag{6.7}$$

At large n these coefficients grow factorially

$$C_n = 2^n n! \tag{6.8}$$

and since they contribute with the same sign, one cannot define the sum of their contributions. Therefore the best one can do is to define the pole position with an intrinsic uncertainty: an optimal truncation of the series leaves us with an irreducible uncertainty of order $\sim \Lambda_{QCD}$ [39, 29]. The above perturbative corrections are an example of the so-called infrared renormalons [129, 143, 137]. The fact that, beyond perturbation theory, the on-shell quark propagator does not have a pole is a correspondence with the fact that quarks are confined inside hadrons and can not be observed directly.

6.1.2 Short distance masses

The renormalon ambiguity associated with the large higher-order corrections to the pole mass, which is the mass parameter in the on-shell renormalization scheme, is also associated to any observable calculated in the same renormalization scheme. If one wants

to achieve a higher degree of accuracy for the prediction of observable quantities that depend on the mass of a quark, the use of mass parameters that can be defined to the desired accuracy becomes compulsory.
A class of mass definitions which are free from non-perturbative (long-distance) ambiguities, called short-distance masses in the literature, has been investigated in the last decades. Among these, $\overline{m}(\mu)$ is the most popular choice. This is the mass defined in the $\overline{MS}$ renormalization scheme [154, 22] which is related to the use of dimensional regularization [155]. It is not a parameter of the effective Lagrangian; it is instead an *ad hoc* combination of the parameters that is extremely convenient in perturbative calculations, particularly in the multi-loop calculations of mass-dependent inclusive physical observables dominated by short-distances (for a review see [62]).
For many purposes, the relation between the $\overline{m}(\mu)$ and the pole mass is required. It is currently known to three loops [63, 135] and, for a given pole mass M, it reads:

$$\begin{aligned}
\frac{\overline{m}(\mu)}{M} &= 1+\frac{\alpha^{(n_f)}(\mu)}{\pi}\left[-\frac{4}{3}-l_{\mu M}\right]+\left(\frac{\alpha^{(n_f)}(\mu)}{\pi}\right)^2\left[-\frac{3019}{288}-2\zeta_2-\frac{2}{3}\zeta_2\ln 2+\frac{1}{6}\zeta_3\right.\\
&- \left.\frac{445}{72}l_{\mu M}-\frac{19}{24}l_{\mu M}^2+\left(\frac{71}{144}+\frac{1}{3}\zeta_2+\frac{13}{36}l_{\mu M}+\frac{1}{12}l_{\mu M}^2\right)n_l-\frac{4}{3}\sum_{1\le i\le n_l}\Delta\left(\frac{M_i}{M}\right)\right]\\
&+ \left(\frac{\alpha^{(n_f)}(\mu)}{\pi}\right)^3\left[z_m^{(}3)(M)+\left(-\frac{165635}{2592}-\frac{25}{3}\zeta_2-\frac{25}{9}\zeta_2\ln 2+\frac{55}{36}\zeta_3\right)l_{\mu M}\right.\\
&- \frac{11779}{864}l_{\mu M}^2-\frac{475}{432}l_{\mu M}^3+n_l\left(\left(\frac{10051}{1296}+\frac{37}{18}\zeta_2+\frac{2}{9}\zeta_2\ln 2+\frac{7}{9}\zeta_3\right)l_{\mu M}+\frac{911}{432}l_{\mu M}^2\right.\\
&+ \left.\left.\frac{11}{54}l_{\mu M}^3\right)+n_l^2\left(\left(-\frac{89}{648}-\frac{1}{9}\zeta_2\right)l_{\mu M}^2-\frac{13}{216}l_{\mu M}^2-\frac{1}{108}l_{\mu M}^3\right)\right] \qquad (6.9)
\end{aligned}$$

where ζ is Riemann's zeta function with values $\zeta_2=\pi^2/6$ and $\zeta_3\approx 1.202\,057$, $l_{\mu M}=\ln\mu^2/M^2$ and n_l is the number of light quark flavors. The function $\Delta(x)$, where x is the ratio of the on-shell mass of the light quarks M_i and M, arises from the two-loop diagram with a second fermion loop [97]. Numerically, the result obtained in Ref. [135] reads:

$$\frac{\overline{m}(M)}{M}=1-\frac{4}{3}\left(\frac{\alpha_s}{\pi}\right)+\left(\frac{\alpha_s}{\pi}\right)^2(1.04\,n_l-14.33)+\left(\frac{\alpha_s}{\pi}\right)^3(-0.65\,n_l^2+26.92\,n_l-198.70)$$

and it agrees very well with the results obtained in Ref. [63].
Until last year (2011), the top quark was the only quark whose mass was given in the particle data listing in the on-shell renormalization scheme while the masses of the other quark flavors were already specified in the $\overline{MS}$ scheme [139]. From 2012, all quark masses are specified in the $\overline{MS}$ scheme.
Since $\overline{m}(\mu)$ logarithmically diverges when $\mu\to 0$, it often happens, however, that the $\overline{MS}$ mass is not the best choice to parameterize the low-energy processes. Recently alternative mass definitions, known as threshold masses, have shown to lead to a better behaved perturbation series than for the $\overline{MS}$ mass: these include the mass in the 1S

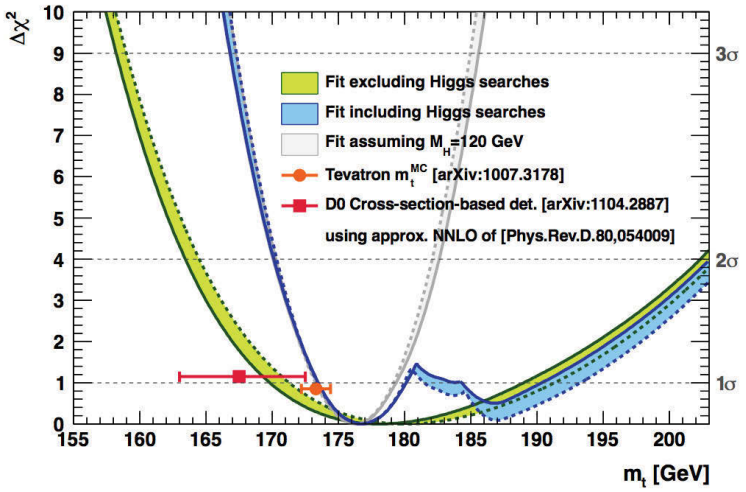

Figure 6.2: Indirect determination of the top quark pole mass with (blue band) and without (green band) the information from the direct Higgs searches al LEP, Tevatron and the LHC [19].

scheme [104, 105], in the PS scheme [28] and in the kinetic scheme [93]. The particle data listing also gives the value of the b-quark mass obtained in the 1S-scheme.

6.2 Experimental methods to extract the top quark mass

There are three fundamental approaches to measuring the top quark mass:

- indirect constraints from electroweak measurements;
- reconstruction of top quark decay products;
- extraction of the top quark mass from the production cross section.

The latest indirect determination of the top quark mass is presented in Ref. [19]. Figure 6.2, taken from this reference, shows the $\Delta\chi^2$ profile versus the top quark pole mass m_t with (blue band) and without (green band) the information from the direct Higgs searches at LEP, Tevatron and the LHC. In both fits, the extraction of m_t from the production cross section performed by the D0 collaboration [8], indicated by the red square, is not included. In the fit which includes the direct Higgs searches, the following two 1σ regions are found:

$$m_t = [173.5, 181.1]\,\text{GeV} \quad \text{and} \quad [184.3, 190.3]\,\text{GeV} \tag{6.10}$$

of which the first one agrees within 1.1σ with the world average of top masses measured from the reconstruction of the decay products, indicated by the red dot in Figure 6.2 [127]. The measurements of m_t based on the reconstruction of the top quark decay

products exploit the conservation of the invariant mass:

$$m_t(i)^2 = P_t(i)^2 = \left(\sum_j P_j(i) \right)^2 \tag{6.11}$$

where P denotes the four-momentum of a particle and the sum is over all decay products j of the top quark t in the event i. A measurement based on the momenta of the decay products might be expected to correspond more closely to a measurement of the pole mass since the squared sum of four-momenta enters the denominator of the propagator. However this statement seems to be not yet supported by a comprehensive theoretical investigation. In general, the individual measurements which adopted this approach differ in how an observable that is related with the top quark mass is constructed from the measured decay products. As an example, the technique most widely used first at the Tevatron and then at the LHC is called "Template Method". It relies on the comparison of the data distribution of an *estimator*, which is correlated with the top quark mass, with expected distributions from different simulated values of the top quark mass.
The rest of this chapter focuses on the extraction of the top quark mass from the production cross section.

6.3 Mass Extraction from total production cross section

The method of mass extraction from total production cross section is based on the comparison between the theoretical and the experimental mass dependence of the total production cross section. In contrast to the mass extraction methods that rely on the reconstruction of an estimator correlated with the mass, this technique allows us to determine a mass parameter expressed in a well-defined renormalization scheme. Therefore the advantage lies in the freedom of choosing a more convenient theoretical framework in which the predictions are more precise. It will be shown in the next section that the total production cross section of $t\bar{t}$ pairs has an overall total uncertainty when expressed in the terms of $\overline{m}_t(\mu)$ which is smaller than that expressed in the on-shell renormalization scheme for the reasons discussed in Section 6.1.1 and 6.1.2. This is translated into a smaller uncertainty in the extracted value of $\overline{m}_t(\mu)$ which can be eventually converted to the pole mass definition. This approach has been adopted with slightly different implementations by the DØ[8], ATLAS [79] and CMS [74] collaborations to extract both the top quark pole and running mass. Similar analyses had already been performed with LEP data to extract the b-quark mass [146, 41].

Theoretical predictions

Two independent theoretical predictions are considered. Figure 6.3 shows the NLO and approximate NNLO total $t\bar{t}$ production cross section obtained using the results of Ref. [128] for a proton-proton collider operating at a center-of-mass energy of 7 TeV. The predictions are shown as a function of the top quark pole (left) and running (right) mass.

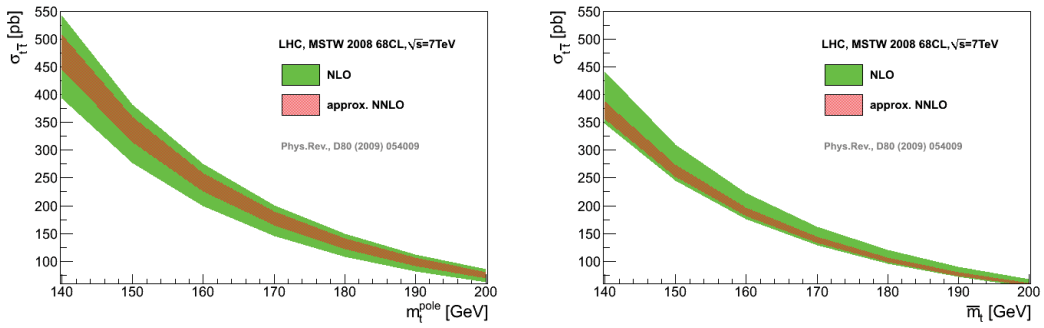

Figure 6.3: The mass dependence of the total cross section as a function of the pole (left) and the $\overline{MS}$ mass at NLO (green) and approximate NNLO (red) obtained using the calculations in Ref. [128].

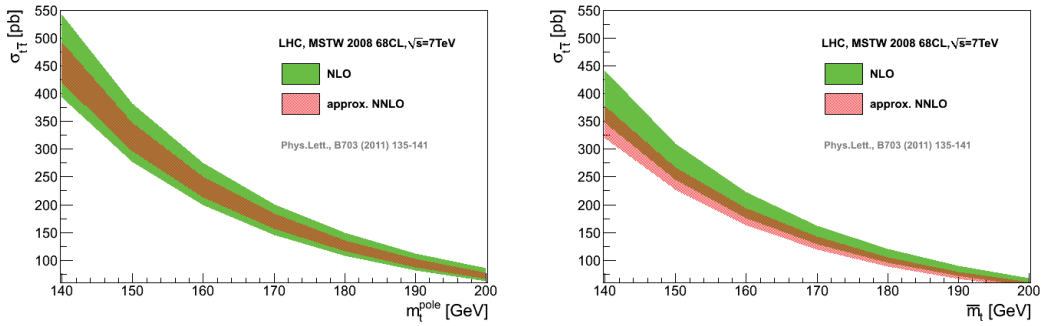

Figure 6.4: The mass dependence of the total cross section for the pole (left) and the $\overline{MS}$ mass at NLO (green) and approximate NNLO (red) obtained using the calculations in [14].

$\overline{m}_t(\mu)$ is always evaluated at the scale $\mu = \overline{m}_t$; therefore, for simplicity, the abbreviation $\overline{m}_t = \overline{m}_t(\overline{m}_t)$ is adopted. The numerical values of the cross section are obtained with *HATHOR* 1.2 [15]: the central values are those corresponding to the default settings $\mu_R = \mu_F = m_t^{\text{pole}}$ and $\mu_R = \mu_F = \overline{m}_t$.
As mentioned in Section 1.2.1 the theory uncertainty arising from the independent variation of the renormalization and factorization scale, μ_R and μ_F, is defined by Equation 1.3 in the standard range $\mu_R, \mu_F \in [m_t/2, 2m_t]$, where m_t stands for either of the mass definitions, with the additional constraint $0.5 < \mu_F/\mu_R < 2$. The PDF set MSTW 2008 at 68% CL is used with an accuracy which matches the order of the perturbative calculations. To quantify the PDF uncertainty, the standard definition is applied:

$$\Delta\sigma = \frac{1}{2}\sqrt{\sum_{k=1,n_{\text{PDF}}} (\sigma_{k+} - \sigma_{k-})^2} \tag{6.12}$$

where $\sigma_{k\pm}$ represent the variations of the cross section with respect to the eigenvectors in the space of the PDF fit parameters. The uncertainty bands in Figure 6.3 denote the linear combination of the scale uncertainty and the PDF uncertainty. The approximate NNLO corrections at $\overline{m}_t = 172.5$ GeV amount to about half of the size of the corrections in the pole mass scheme. This is due to the faster convergence of the perturbative expansion when using the $\overline{MS}$ mass observed by the authors of Ref. [128].
Figure 6.4 shows the approximate NNLO predictions of the total $t\bar{t}$ production cross section obtained as described in Ref. [14]. Also in this case, the numerical values are produced with a software tool, called *RunTop*, provided by the authors [3]. For the estimation of the uncertainty associated to scale variations, they consider two different methods: correlated variations with $\mu_R = \mu_F$ varied up and down by a factor of two from the default value set equal to the top quark mass, and independent variations of μ_F and μ_R by factors of two, with the uncertainties added in quadrature. The tool returns the larger uncertainty from these two methods. For the PDF uncertainty, the same convention as before is used.
From a comparison of Figure 6.3 and 6.4, we see that the perturbative uncertainty in the approximate NNLO results is always reduced compared to that in the NLO calculation. However, in contrast to Ref. [128], the authors of Ref. [14] do not find a strong improvement of the perturbative series in the $\overline{MS}$ scheme compared to the pole mass scheme. Finally, the authors of Ref. [14] consider an additional source of uncertainty related to the experimental value of $\alpha_s(M_Z)$, which is an input parameter for the running of the strong coupling constant. The authors estimate this uncertainty in combination with the PDF one by employing the method proposed in [133, 125]. They conclude that the uncertainty on $\alpha_s(M_Z)$ adds an error to the cross section which, depending on the PDF set used, can reach up to 4% and therefore should not be neglected.

Experimental input

The cross section measurement presented in Chapter 5 implicitly refers to the production of pairs of top quarks with a mass of 172.5 GeV as the simulated $t\bar{t}$ signal sample used in the analysis is generated for a MC top quark mass parameter set to this value. In order to obtain the experimental mass dependence of the cross section, the multivariate analysis is repeated using $t\bar{t}$ samples simulated at seven different values of the top quark mass (see Section 3.2.1). The new cross sections are extracted in maximum likelihood fits which include only the normalization β-parameters [4]. Among the five sources of background considered, single top is the only process which is affected by a change in the value of the top quark mass. Therefore, whenever a different mass for the $t\bar{t}$ signal is used, the single top MC samples relative to the same mass value are used consistently.
As the top quark mass decreases, its decay products are expected to have lower momenta and energies. Similarly, the decay products of heavier top quarks must necessarily show

[3] The software implementation is included in the electronic submission of Ref. [14]
[4] As it will be explained later in this section, a change in the value of the MC top-quark mass parameter leads to a change in acceptance which introduces additional shape distortions that go beyond the effect of the systematic sources. In this case a profile likelihood fit may give unrealistic results.

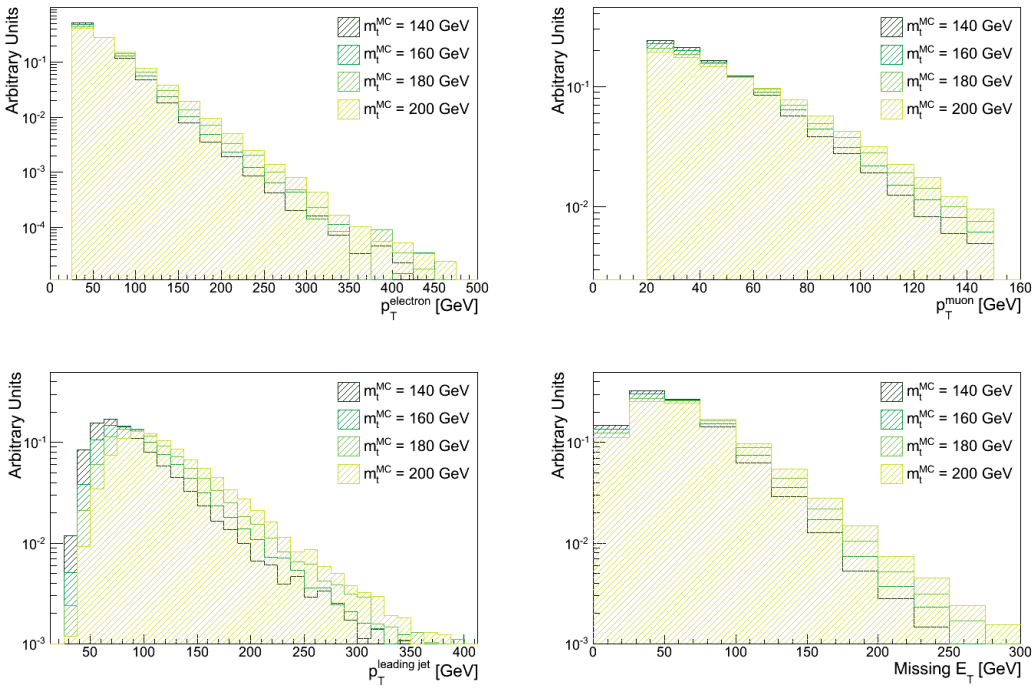

Figure 6.5: Normalized p_T distributions of electrons, muons and leading jets and normalized distribution of missing transverse energy for selected $t\bar{t}$ events with at least three jets simulated at different value of the top quark mass.

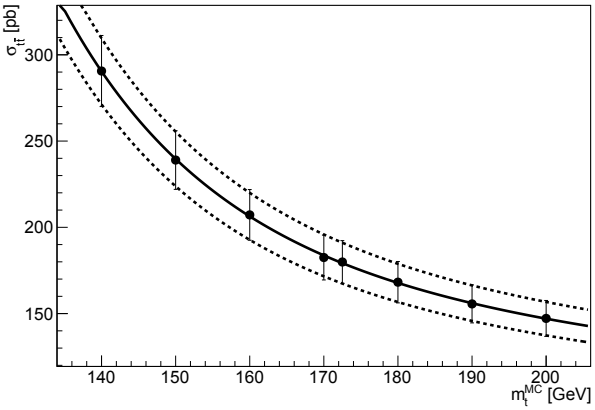

Figure 6.6: The experimental mass dependence of the total $t\bar{t}$ cross section.

higher momenta. This is readily verified in Figure 6.5 which shows the transverse momentum of electrons, muons and leading jets and the transverse missing energy, which is a measure of the neutrino transverse momentum, in selected events with at least three jets for different values of the top quark mass. The thresholds in the selection

cuts of leptons and jets applied at each mass point are unchanged with respect to those applied at the nominal MC mass parameter value $m_t = 172.5$ GeV and described in Chapter 4. The resulting change in the signal acceptance for masses differing from the nominal one is expected to manifest itself in an decreasing cross section as a function of increasing top quark mass. This expectation is confirmed in Figure 6.6, where the obtained cross sections are shown. The dependence is found to be much weaker than the dependence of the theoretical calculations. The central values are also listed in Table 6.1 together with their statistical uncertainties. The decreasing statistical uncertainty as a function of increasing mass is the direct consequence of the increased acceptance. The relative systematic uncertainty is expected to be independent of the value of the top quark mass and fully correlated among the various mass values. Therefore a total relative systematic uncertainty of 6.7% (which includes the 3.7% uncertainty on the total luminosity) is added in quadrature to the statistical uncertainties and the resulting total uncertainty is shown in the last column of Table 6.1. The same approach is also adopted in Ref. [8] and [79]. The expectation is verified by generating a reduced set of systematic templates at two other mass points. The systematic sources stemming from the choice of MC generator, hadronization model, initial and final state radiation have to be neglected because MC samples simulated for different values of the top quark mass are not available. In the nominal analysis, these sources make up about 60% of the total uncertainty. As in Ref. [79], the accuracy of the assumption is checked at the extreme mass points: $m_t = 140$ GeV and $m_t = 200$ GeV. The cross sections obtained are $\sigma_{t\bar{t}}(m_t = 140\,\text{GeV}) = 291^{+25.3}_{-24.6}$ pb and $\sigma_{t\bar{t}}(m_t = 200\,\text{GeV}) = 147.0^{+11.4}_{-12.1}$ pb, where the quoted uncertainty is the result of the quadratic combination of the statistical uncertainty, the expected systematic uncertainty, evaluated by means of pseudo-experiments (PEs), scaled to include the neglected systematic sources and the luminosity uncertainty. These values suggest that the assumption made is legitimate. They also show that, at least at these two mass points, it leads to a small underestimation of the total systematic uncertainty of up to 1.7%, which is not considered in the final result.
Both the theoretical and the experimental mass dependence of the cross section is parameterized with the following fit formula:

$$\sigma_{t\bar{t}}(m_t) = \left(\frac{1}{m_t}\right)^4 \left(a + b(m_t - 172.5) + c(m_t - 172.5)^2 + d(m_t - 172.5)^3\right) \qquad (6.13)$$

where m_t can be interpreted as the pole as well as the running $\overline{m}_t$ mass measured in GeV. The accuracy of the fits, measured as deviation of the fitted functions from the experimental and theoretical points, is better than 1%, as can be seen in Figure 6.6 for the experimental case. The parameters derived from the fit can be found in Table 6.2.
As a final remark, it is important to point out that the mass measured with this and any other technique that relies on MC simulations of the $t\bar{t}$ signal corresponds to a measurement of the top quark mass relative to the scheme used in the MC simulations m_t^{MC}. As pointed out in Ref. [8], it is in principle not possible to establish a direct connection between m_t^{MC} and any theoretical mass parameter, like m_t^{pole} or $\overline{m}_t$. There are studies that argue that the MC mass should be close to the pole mass [90] but

m_t^{MC} [GeV]	$\sigma_{t\bar{t}}$ [pb]	stat. uncert. [pb]	tot. uncert. [pb]
140	291.9	±6.1	±25.0
150	240.1	±5.1	±17.0
160	208.1	±4.4	±14.7
170	183.3	±3.9	±13.0
172.5	179.7	±3.8	±12.3
180	169.0	±3.6	±12.0
190	156.3	±3.4	±11.1
200	147.0	±3.1	±12.0

Table 6.1: Total $t\bar{t}$ cross sections and their uncertainties obtained for different values of the simulated top quark mass. The last column shows the total uncertainty. For $m_t^{MC} =$ 140 GeV and 200 GeV, the systematic uncertainty is evaluated with a reduced set of systematic templates by performing PEs and it is subsequently scaled to include the neglected systematic sources. At the other mass points, it is derived under the assumption that the relative systematic uncertainty is independent of the value of the top quark mass and fully correlated among the various mass values.

	a	b	c	d
Experimental curve (m_t^{MC})	$1.59 \cdot 10^{11}$	$2.15 \cdot 10^{9}$	$2.23 \cdot 10^{7}$	$2.16 \cdot 10^{4}$
approx. NNLO (m_t^{pole}) [128]	$1.47 \cdot 10^{11}$	$-1.02 \cdot 10^{9}$	$4.17 \cdot 10^{6}$	$9.88 \cdot 10^{3}$
approx. NNLO (m_t^{pole}) [14]	$1.39 \cdot 10^{11}$	$-9.57 \cdot 10^{8}$	$3.83 \cdot 10^{6}$	$-7.69 \cdot 10^{3}$
approx. NNLO ($\overline{m}_t$) [128]	$1.15 \cdot 10^{11}$	$-8.05 \cdot 10^{8}$	$3.29 \cdot 10^{6}$	$-7.7 \cdot 10^{3}$
approx. NNLO ($\overline{m}_t$) [14]	$1.07 \cdot 10^{11}$	$-7.37 \cdot 10^{8}$	$2.86 \cdot 10^{6}$	$-9.71 \cdot 10^{3}$

Table 6.2: Coefficients of the fit function in Equation 6.13.

there are still ongoing theoretical investigations. In some cases, like in Ref. [85], m_t^{MC} is assumed to be equal to m_t^{pole} and in others, e.g. Ref. [8], it is stated that the top quark pole mass could be about 1 GeV higher than the values extracted in direct Tevatron measurements. In order to be consistent with Ref. [79], m_t^{MC} is shifted by ±1 GeV and the difference in the value of the extracted mass with the nominal value, which is about 0.5 GeV for both methods presented below, is added linearly as an additional uncertainty.

6.3.1 Extraction of m_t^{pole}

First, the top quark mass is extracted with the method used by the DØ collaboration. It is based on the construction of a joint probability density function built from the product of the experimental and theoretical probability density functions:

$$f(m_t) \propto \int f_{th}(\sigma|m_t) f_{exp}(\sigma|m_t) d\sigma. \tag{6.14}$$

Theoretical predictions	m_t^{pole} [GeV]
Ref. [128]	169.4 ± 5.4
Ref. [14]	166.6 ± 5.5

Table 6.3: Extracted values of the top quark pole mass for the two theoretical predictions considered. The uncertainty includes the linear addition of the 0.5 GeV uncertainty stemming from the assumption that the MC mass parameter is equal to the the pole mass.

Equation 6.14 is clearly valid under the assumption that the theoretical and experimental uncertainties are independent of each other which is reasonable as none of the systematic sources taken into account in the experimental measurement is directly related to either the PDF or the scale variation uncertainty. $f_{th}(\sigma|m_t)$ represents the theoretical probability density function defined, for each value of the mass, as a Gaussian probability density function centered on the approximate NNLO theoretical predictions of the cross section in the pole mass scheme. Since the uncertainty resulting from the linear addition of the scale variation and the PDF uncertainties is asymmetric, it is for simplicity symmetrized to the largest deviation from the nominal value at each value of the mass. In this way the standard deviation of the Gaussian functions constructed on the theory uncertainty band can be set to half of the band width. This procedure introduces an overestimate of the total uncertainty of about 20% when using the calculations of Ref. [128] and 1% when using those of Ref. [14]. Likewise, $f_{exp}(\sigma|m_t)$ is the experimental probability density function constructed using Gaussian probability density functions centered on the measured cross section and having as width the total experimental uncertainty. $f_{th}(\sigma|m_t)$ and $f_{exp}(\sigma|m_t)$ are given explicitly by:

$$f_{th}(\sigma|m_t) = \frac{1}{\sqrt{2\pi}(\Delta_{\text{PDF}}(m_t) + \Delta_{\text{scale}}(m_t))} \exp\left(-\frac{(\sigma - \sigma_{th}(m_t))^2}{2(\Delta_{\text{PDF}}(m_t) + \Delta_{\text{scale}}(m_t))^2}\right) \tag{6.15}$$

and

$$f_{exp}(\sigma|m_t) = \frac{1}{\sqrt{2\pi}\Delta_{exp}(m_t)} \exp\left(-\frac{(\sigma - \sigma_{th}(m_t))^2}{2\Delta_{exp}^2(m_t)^2}\right) \tag{6.16}$$

The mass value that maximizes $f(m_t)$ in Equation 6.14 is the extracted top mass. The mass values that contain 68% of the integral of $f(m_t)$ around its peak are quoted as the $\pm 1\sigma$ uncertainty in the central value.
The mass is extracted using the two theoretical predictions described above: the probability density functions $f(m_t)$ obtained are shown in Figure 6.7 and the resulting values are summarized in Table 6.3.

6.3.2 Extraction of $\overline{m}$

For the extraction of $\overline{m}_t$, the predictions used are those defined in the $\overline{MS}$ scheme at approximate NNLO accuracy. The experimental input is unaltered and, as before, it is

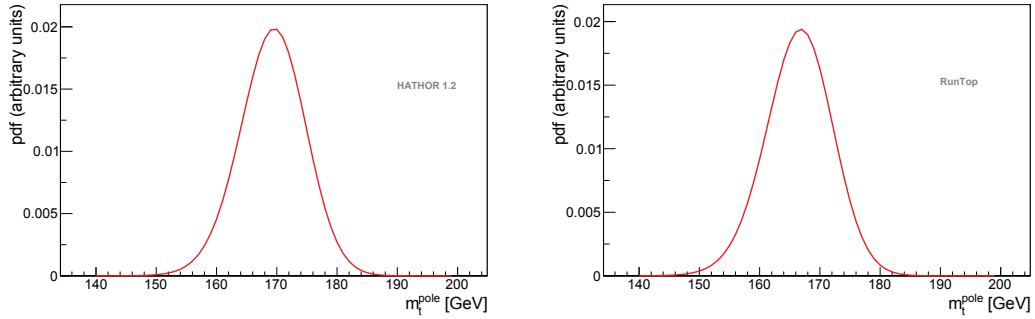

Figure 6.7: Joint probability density function in Equation 6.14 obtained using the theoretical predictions in Ref. [128] (left) and Ref. [14] (right). The peak position represents the extracted value. The area around the peak containing 68.3% of the pdf integral defines its uncertainty.

assumed to be a function of the pole mass. The method, which was proposed by Sven-Olaf Moch, one of the authors of Ref. [128], and also used by the CMS collaboration in Ref. [74], is based on the concept that the cross section is an observable and, therefore, it must be independent of the renormalization scheme used. It makes use of an iterative procedure that can be summarized in four steps:

1. the cross section measured at $m_t^{MC} = m_t^{\text{pole}} = 172.5$ GeV is the starting point: $\sigma_{t\bar{t}}(m_t^{\text{pole}}) = 178.9$ pb;
2. using the theoretical predictions, find which value of $\overline{m}_t$ gives the same cross section: $\sigma_{t\bar{t}}(\overline{m}_t) = 178.9$ pb;
3. convert this value of $\overline{m}_t$ into $m_t'^{\text{pole}}$;
4. find the experimental cross section which corresponds to $m_t'^{\text{pole}}$ and start again from the first step.

The conversion between $\overline{m}_t$ and m_t^{pole} is performed with the CRunDec package [150] which implements the conversion formula in Equation 6.9. This iterative procedure converges quickly to a mass value: this is the extracted mass.
Because of the presence of the theoretical uncertainty band, there is an interval of $\overline{m}_t$ values which correspond to the same cross section $\sigma_{t\bar{t}}$ at step 2. At the same time, because of the uncertainty band of the experimental curve, there is an interval of cross section values relative to the same value of m_t^{pole} at step 4. For the extraction of the nominal $\overline{m}_t$, the central values of the theoretical and experimental inputs are used. For the estimation of the uncertainty in the extracted mass value, a set of 10000 PEs is carried out which take into account the two uncertainty bands.
For each PE i a random number $r^i_{(2)}$ is drawn from a unit Gaussian. Each time step 2 is executed in the iterative procedure, $r^i_{(2)}$ is scaled to the standard deviation of a Gaussian probability density function centered on the nominal value of the theoretical

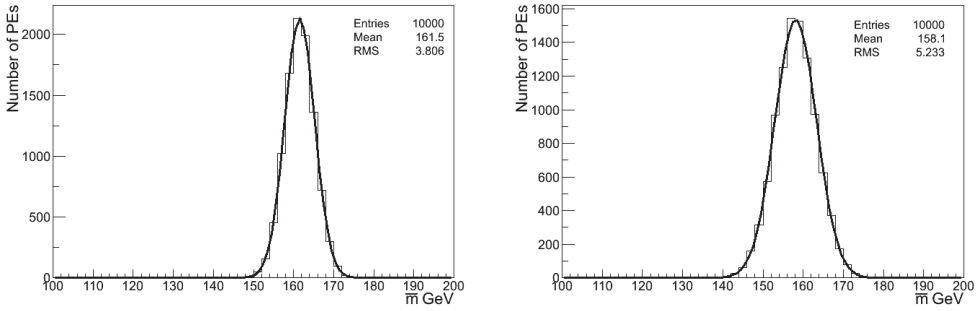

Figure 6.8: Distribution of extracted masses in 10000 PEs which take into account the theoretical (Ref. [128] on the left and Ref. [14] on the right) and experimental uncertainty bands as described in the text. The standard deviation of the fitted Gaussian is taken as uncertainty of the extracted central value of the top quark mass.

predictions and having a width equal to the width of the theoretical uncertainty band at the fixed value $\sigma_{t\bar{t}}$ found at step 1. Note that a bifurcated Gaussian constructed in this way is asymmetric and therefore $r^i_{(2)}$ is scaled to the upper one-standard deviation if $r^i_{(2)} > 0$ and vice versa. A second random number $r^i_{(4)}$ is drawn from a unit Gaussian and the same procedure described for step 2 is carried out each time step 4 is executed in the iterative procedure: this time the bifurcated Gaussian is constructed from the experimental uncertainty band along the line of constant m_t^{pole} found in step 3. Note that, at each PE, two new random numbers are drawn.
The mass values extracted in the PEs are stored in a histogram. A Gaussian function is fitted to the distribution of extracted masses: it is expected to peak at the nominal mass extracted using the central values of the theoretical and experimental inputs and to have a width proportional to their width. The one-standard deviation of this Gaussian, shown in Figure 6.8, is the quoted uncertainty. The $\overline{m}_t$ values corresponding to the two theoretical predictions are listed in Table 6.4. This table also shows the contribution to the uncertainty of the different sources: they are obtained by repeating the extraction considering the individual sources one at a time. One can see how the PDF and the scale variation uncertainties in the extracted mass value combine linearly to give the total theoretical uncertainty. Note also that the uncertainty obtained when considering both the theory and the experimental uncertainty is smaller than the linear sum of the two components (and it is close to their quadratic sum). This effect stems from the fact that in the PEs for which the two extracted Gaussian random numbers have opposite sign the uncertainties cancel out.

6.4 Top++

A new tool called Top++ [77] for the calculation of the total inclusive top-pair production cross section at hadron colliders has recently become available. This program uses all the most recent theoretical results including the exact NNLO calculations for $q\bar{q} \to t\bar{t} + X$,

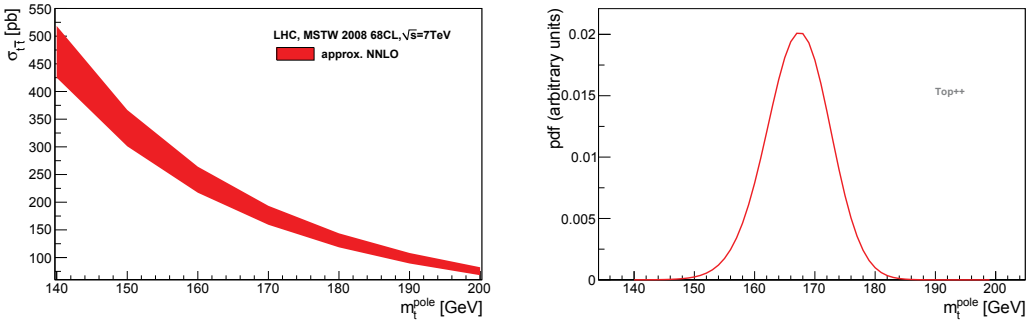

Figure 6.9: Left: approximate NNLO predictions obtained with Top++ as a function of the top-quark pole mass. Right: joint pdf of Equation 6.14 obtained using the Top++ approximate NNLO predictions and the experimental measurements.

$qq \to t\bar{t} + X$, $q\bar{q}' \to t\bar{t} + X$, $qq' \to t\bar{t} + X$ and approximate NNLO for $gg \to t\bar{t} + X$ [78, 20, 49]. The improved theoretical predictions are reflected in a smaller scale-variation uncertainty which, at a proton-proton collider at 7 TeV center-of-mass energy, is reduced by 2%. However the program does not allow the calculations to be performed in the $\overline{MS}$ scheme. As noted on the Top++ manual, it is not possible to compare directly Top++ results with the approximate NNLO results from *HATHOR* in the on-shell scheme as the programs contain different implementations of the approximation.
For the sake of completeness, the extraction of m_t^{pole} is repeated using Top++ theoretical predictions at full available accuracy. On the left-hand side of Figure 6.9 these are shown as a function of the top-quark pole mass: as before the scale-variation and PDF uncertainties are added linearly. On the right-hand side, the probability density function $f(m_t^{\text{pole}})$ defined in Equation 6.14 is shown. As before, the peak of this distribution

	Ref. [128]	Ref. [14]
$\overline{m}_t$	161.5	158.1
theory+exp. uncert.	3.8	5.2
exp. uncert. only	3.3	3.3
theory uncert. only	1.7	4.0
PDF uncert. only	1.2	1.3
scale uncert. only	0.5	2.7
PDF+α_s uncert.	–	(1.9)
m_t^{MC} uncert.	0.5	0.5
tot.uncert.	4.3	5.7

Table 6.4: Extracted $\overline{m}_t$ masses and their uncertainties. All numbers are in GeV. The theoretical calculations used are indicated in the top row. The PDF+α_s uncertainty is not included in the total uncertainty.

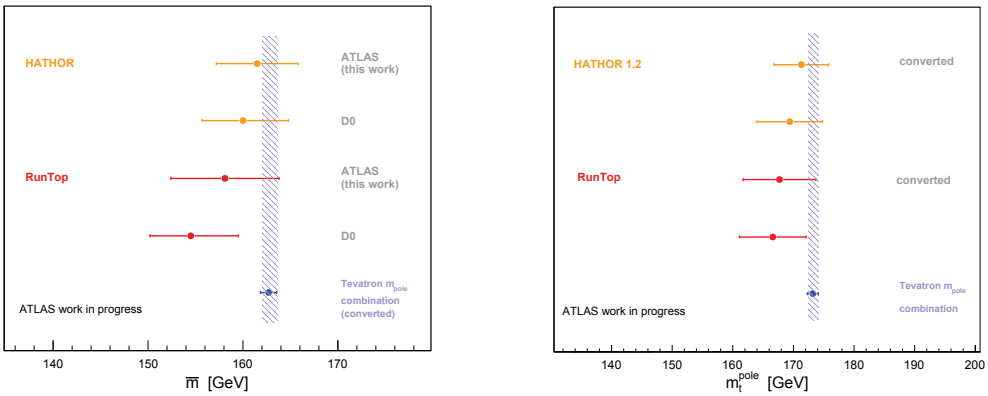

Figure 6.10: Extracted values of the top quark mass. On the left-hand side, the two $\overline{m}_t$ values obtained are compared with those extracted by the DØ collaboration. On the right-hand side, they are instead converted to pole masses and compared to the two m_t^{pole} values extracted directly from the production cross section expressed in the pole mass scheme. The latest Tevatron combination of m_t^{pole} measurements from the reconstruction of the decay products is shown on both graphs.

represents the most probable value of the mass from the combination of the theoretical and experimental distributions. The uncertainty in the extracted mass is obtained by integrating 68% of $f(m_t^{\text{pole}})$ symmetrically around its peak. The mass obtained is 167.3± 5.3 GeV and it agrees with the measurements described in the previous sections.

6.5 Summary and outlook

The top quark pole and $\overline{MS}$ masses are extracted with two methods based on the comparison between the theoretical and the experimental mass dependence of the total $t\bar{t}$ production cross section. The values obtained are displayed in Figure 6.10. In the plot on the left-hand side, the two extracted $\overline{m}_t$ masses are compared to the two DØ measurements which extract $\overline{m}_t$ from the total production cross section using the same theoretical predictions. The method adopted by the DØ collaboration to extract $\overline{m}_t$ is different from the one used here and more similar to the method used to extract m_t^{pole}. Other relevant differences lie in the treatment of the theoretical uncertainties: they evaluate the scale dependence of the cross section in the same standard range but always considering $\mu_R = \mu_F = \mu$ [5] and symmetrize the total uncertainty. Lastly, they evaluate the impact of the assumption $m_t^{MC} = m_t^{\text{pole}}$ by performing a second extraction in which m_t^{MC} is interpreted as $\overline{m}_t$ and they include half of the difference in the extracted value symmetrically in the systematic uncertainty.
On the right-hand side of Figure 6.10, the two $\overline{m}_t$ measurements are converted to their corresponding pole mass values and shown together with the two measurements of m_t^{pole}

[5] Remember that, as already stated in the first chapter of this thesis, this approach has been proved to approximate the total scale dependence of the cross section rather well.

extracted directly from the predictions expressed in the pole mass scheme [6]. None of the measurements displayed in Figure 6.10 includes the additional uncertainty on the theoretical cross section originating from the experimental uncertainty of $\alpha_s(M_Z)$, which is an input parameter for the running of α_s. This source of uncertainty is only considered by the authors of Ref. [14]. In both plots of Figure 6.10, the Tevatron combination of the best CDF and DØ measurements using up to 5.8 fb^{-1} is shown. Within 1.1 standard deviations, all values obtained agree with the Tevatron combination.
The precision of the mass values obtained is limited by the theoretical and experimental uncertainty bands. The measurement which has the overall smallest uncertainty is the mass extracted in the $\overline{MS}$ scheme when using the calculations in Ref. [128]. The only reason behind this improvement lies in the more stable prediction with respect to scale variation observed by the authors of Ref. [128] when employing the $\overline{MS}$ mass definition and when including high-order perturbative corrections, as the plot on the right-hand side of Figure 6.3 shows. In the future, the inclusion of higher order calculations may lead to a further reduction of the scale variation uncertainty. On the other hand, the authors of Ref. [14] observe a weaker improvement of the convergence of the perturbative series in the $\overline{MS}$ scheme (see Figure 6.4) with respect to the pole mass scheme, which is reflected in a larger uncertainty in the extracted mass value.
The uncertainty of the experimental cross section measurement is dominated by the systematic uncertainties associated to the luminosity, the physics objects and, in particular, to the choice of specific models for the description of the $t\bar{t}$ signal, like the hard partonic process, the hadronization phase and the final state radiation. Besides reducing the impact of these systematic sources, the precision of the extracted mass value could be improved by a reduction of the mass dependence of the total experimental cross section which in turn depends, as explained above, on the mass dependence of the signal acceptance. For each value of the top quark MC mass, the kinematical thresholds of the event selection may be tuned to obtain a constant signal acceptance and hence a smaller overlap region between the experimental and theoretical curves. This additional study has not been carried out due to the lack of two important experimental inputs which strongly rely on the official selection cuts of the $t\bar{t}$ signal: the W+Jets data-driven normalization scale factors from charge asymmetry studies and an implementation of the matrix method for the QCD estimate. With these inputs the presented measurements could be improved.
As a final remark it is important to point out that, even though the use of the $\overline{MS}$ scheme leads to more precise results, the renormalon ambiguity of order Λ_{QCD} in the position of the pole of the on-shell free quark propagator is still far from being a practical problem. This is true even when considering the most precise Tevatron combination $m_t^{\text{pole}} = 173.3 \pm 0.9$ GeV. It is worth noting that simulation studies have already proven that at a future linear e^+e^- collider the top quark 1S mass can be be determined with a theoretical uncertainty of about 100 MeV in threshold scans of the total $t\bar{t}$ cross section

[6] The central value and the upper and lower edge of the measurements are converted individually. The effect of a different overlap with the Tevatron average comes from the fact the conversion of the upper and lower edges uses different values of the strong coupling constant as this is always evaluated at the scale set by the mass value considered.

[103].

7 Conclusions

There are several theoretical reasons to study the mass of the top quark. For instance, it checks the consistency of the EW theory through the higher-order corrections to the W boson mass. It is also close enough to the EW symmetry breaking scale to raise suspicions of an hypothetical role played by the top quark itself in the breaking. The mass of the top quark is a free parameter that cannot be neglected in the theory which studies the heavy quarks. However, the impossibility to observe isolated quarks renders any possible definition of quark mass a purely theoretical construction. The quark pole mass, which is the QCD equivalent of the mass definition in the QED theory, shows a rather poor convergence of the perturbative series already at low orders in perturbation theory: the series must be truncated leaving an uncertainty of order Λ_{QCD} in the value of the quark pole mass. Many other mass parameters have been proposed since this problem with the quark pole mass was realized. Depending on the characteristic scale of the physics process one is interested in, the theoretical predictions can be expressed in the most advantageous one. The most popular choice has been, lately, the renormalized quark mass in the modified minimal subtraction scheme. This is motivated by the better convergence of the perturbative series which leads to more precise predictions. The experimental methods to extract the top quark mass which rely on the reconstruction of the invariant mass peak of the top quark decay products are most likely to extract a mass which is closely related to the top quark pole mass. A way to extract the top quark mass in a well-defined renormalization scheme is to extract it from the production cross section.

The top quark is a unique particle also in experimental terms: this large mass is reflected in a large decay width of about 2 GeV which, translated into decay time, implies that top quarks, unlike any other quark flavor, decay before forming bound states of hadrons. In the standard model, the channel $t \to Wb$ has a branching ratio of almost 100%. At the Large Hadron Collider, top quarks are produced predominantly in pairs of particle and antiparticle. Among the three possible decay channels of $t\bar{t}$ pairs, dictated by the two possible decay channels of the two emitted W bosons, the semi-leptonic channel offers the best compromise between production rate and discrimination power. The total $t\bar{t}$ production cross section is measured in the semi-leptonic channel using an integrated luminosity of 700 pb^{-1} collected by the ATLAS detector in the first half of 2011. It is based on a multi-variate analysis which combines information from four selected discriminating variables. These mainly exploit the direction of the lepton coming from the W and the global energy flow of the event. Five sources of background characterized by a signature similar to the signal generated by $t\bar{t}$ pairs are considered. Among these, the simultaneous production of a W boson and QCD jets is the dominant source. For each process, the four input variables are combined into a one-dimensional template with the

	Ref. [128]	Ref. [14]
First Method	169.4 ± 5.9 GeV	166.6 ± 6.0 GeV
Second Method (converted)	171.2 ± 4.5 GeV	167.8 ± 5.7 GeV

Table 7.1: Extracted pole masses for the top quark. The first method extracts m_t^{pole} directly from the predictions in the pole mass scheme. The second method uses the predictions in the $\overline{m}_t$ scheme: the values shown in the last row have been converted to the on-shell scheme.

aid of a likelihood classifier. The total cross section is extracted in a profile likelihood fit of the Monte Carlo templates to the data templates. In order to enforce its constraining power, the fit is performed simultaneously in three different channels differing in the number of jets in the final state. Most of the systematic uncertainties affecting the $t\bar{t}$ cross section are included directly in the fit: the distorted systematic templates give morphing degrees of freedom to the nominal templates which change shape to increase the data-Monte Carlo agreement. The extracted value $\sigma_{t\bar{t}} = 178.9 \pm 12$ pb agrees within 1σ with the two theoretical predictions considered at approximate NNLO accuracy: $\sigma_{t\bar{t}} = 166.7^{+9.2}_{-13.8}$ pb [128] and $\sigma_{t\bar{t}} = 157.9^{+12.2}_{-13.2}$ pb [14].
The analysis is repeated for different values of the Monte Carlo mass: the mass dependence of the experimental cross section is found, as expected, weaker than the theoretical one. The Monte Carlo mass is always interpreted as the pole mass and a systematic uncertainty is assigned to this assumption. First the top quark pole mass is extracted directly using the theoretical predictions in the pole mass scheme: the central value of the measurement corresponds to the mass which maximizes the joint probability density function of the Gaussian probability density functions constructed on the theoretical and experimental curves. Secondly, the running mass $\overline{m}_t$ at the scale $\overline{m}_t$ is extracted considering the theoretical predictions in the $\overline{MS}$ scheme and using a method which iteratively finds the value of the mass for which the cross section is the same in both renormalization schemes.
The masses extracted with these two methods are summarized in Table 7.1. The most precise value obtained in this work is $m_t^{\text{pole}} = 171.2 \pm 4.5$ GeV and it comes from the scenario with the smallest theoretical uncertainty, namely the approximate NNLO calculations of Ref. [128] in the $\overline{MS}$ scheme. The uncertainty in the extracted mass value is, however, very large compared to the intrinsic uncertainty of order Λ_{QCD} which disfavors the quark pole mass definition. As the plot on the right-hand side of Figure 6.10 shows, the four measurements presented are compatible with the latest Tevatron combination [127] whose input measurements are based on the direct reconstruction of the top quark decay products. In addition, the two measurements that use the theoretical prediction in Ref. [128] overlap within 1σ with the indirect determination of the top quark pole mass which includes Higgs searches at LEP, Tevatron and the LHC.

Bibliography

[1] G. Aad et al. The ATLAS Experiment at the CERN Large Hadron Collider. *JINST*, 3:S08003, 2008.

[2] Georges Aad et al. Electron performance measurements with the ATLAS detector using the 2010 LHC proton-proton collision data. *Eur.Phys.J.*, C72:1909, 2012.

[3] Georges Aad et al. Measurement of the top quark pair production cross-section with ATLAS in the single lepton channel. *Phys. Lett.*, B711:244–263, 2012.

[4] T. Aaltonen et al. First Observation of Electroweak Single Top Quark Production. *Phys.Rev.Lett.*, 103:092002, 2009.

[5] T. Aaltonen et al. Precise measurement of the W-boson mass with the CDF II detector. *Phys.Rev.Lett.*, 108:151803, 2012.

[6] S. Abachi et al. Observation of the top quark. *Phys.Rev.Lett.*, 74:2632–2637, 1995.

[7] V. Abazov et al. An Improved determination of the width of the top quark. *arXiv:1201.4156*, 2012.

[8] Victor Mukhamedovich Abazov et al. Determination of the pole and $\overline{MS}$ masses of the top quark from the $t\bar{t}$ cross section. *Phys.Lett.*, B703:422–427, 2011.

[9] V.M. Abazov et al. Observation of Single Top Quark Production. *Phys.Rev.Lett.*, 103:092001, 2009.

[10] F. Abe et al. Observation of top quark production in $\bar{p}p$ collisions. *Phys.Rev.Lett.*, 74:2626–2631, 1995.

[11] B. Acharya et al. Object selection and calibration, background estimations and MC samples for the summer 2012 top quark analyses with 2011 data. Technical Report ATL-COM-PHYS-2012-499, CERN, Geneva, May 2012. Internal document.

[12] S. Agostinelli et al. GEANT4: A Simulation toolkit. *Nucl.Instrum.Meth.*, A506:250–303, 2003.

[13] M. Agustoni et al. Electromagnetic energy scale in-situ calibration and performance: Supporting document for the egamma performance paper. Technical Report ATL-COM-PHYS-2011-263, CERN, Geneva, Mar 2011. Internal document.

[14] Valentin Ahrens, Andrea Ferroglia, Matthias Neubert, Ben D. Pecjak, and Li Lin Yang. Precision predictions for the $t\bar{t}$ production cross section at hadron colliders. *Phys.Lett.*, B703:135–141, 2011.

[15] M. Aliev, H. Lacker, U. Langenfeld, S. Moch, P. Uwer, et al. HATHOR: HAdronic Top and Heavy quarks crOss section calculatoR. *Comput.Phys.Commun.*, 182:1034–1046, 2011.

[16] Johan Alwall, Stefan Höche, F. Krauss, N. Lavesson, L. Lönnblad, et al. Comparative study of various algorithms for the merging of parton showers and matrix elements in hadronic collisions. *Eur.Phys.J.*, C53:473–500, 2008.

[17] Ugo Amaldi. Fluctuations in Calorimetry Measurements. *Phys.Scripta*, 23:409, 1981.

[18] ATLAS Collaboration. `https://twiki.cern.ch/twiki/bin/view/AtlasPublic/LuminosityPublicResults`, 2011.

[19] M. Baak, M. Göbel, J. Haller, A. Höcker, D. Ludwig, et al. Updated Status of the Global Electroweak Fit and Constraints on New Physics. *Eur.Phys.J.*, C72:2003, 2012.

[20] Peter Baernreuther, Michal Czakon, and Alexander Mitov. Percent level precision physics at the Tevatron: first genuine NNLO QCD corrections to $q\bar{q} \to t\bar{t} + X$. *arXiv:1204.5201*, 2012.

[21] Andrea Banfi and Eric Laenen. Joint resummation for heavy quark production. *Phys.Rev.*, D71:034003, 2005.

[22] William A. Bardeen, A.J. Buras, D.W. Duke, and T. Muta. Deep Inelastic Scattering Beyond the Leading Order in Asymptotically Free Gauge Theories. *Phys.Rev.*, D18:3998, 1978.

[23] Roger J. Barlow and Christine Beeston. Fitting using finite Monte Carlo samples. *Comput.Phys.Commun.*, 77:219–228, 1993.

[24] K Becker et al. Mis-identified lepton backgrounds in top quark pair production studies for EPS 2011 analyses. Technical Report ATL-COM-PHYS-2011-768, CERN, Geneva, Jun 2011. Internal document.

[25] W. Beenakker, Frits A. Berends, and A.P. Chapovsky. One loop QCD interconnection effects in pair production of top quarks. *Phys.Lett.*, B454:129–136, 1999.

[26] W. Beenakker, H. Kuijf, W.L. van Neerven, and J. Smith. QCD Corrections to Heavy Quark Production in $p\bar{p}$ Collisions. *Phys.Rev.*, D40:54–82, 1989.

[27] W. Beenakker, W.L. van Neerven, R. Meng, G.A. Schuler, and J. Smith. QCD corrections to heavy quark production in hadron collisions. *Nucl.Phys.*, B351:507–560, 1991.

[28] M. Beneke. A Quark mass definition adequate for threshold problems. *Phys.Lett.*, B434:115–125, 1998.

[29] M. Beneke and Vladimir M. Braun. Heavy quark effective theory beyond perturbation theory: Renormalons, the pole mass and the residual mass term. *Nucl.Phys.*, B426:301–343, 1994.

[30] Frits A. Berends, W.T. Giele, H. Kuijf, R. Kleiss, and W. James Stirling. Multi-jet production in W, Z events at $p\bar{p}$ colliders. *Phys.Lett.*, B224:237, 1989.

[31] Edmond L. Berger and Harry Contopanagos. Perturbative gluon resummation of the top quark production cross-section. *Phys.Lett.*, B361:115–120, 1995.

[32] Edmond L. Berger and Harry Contopanagos. The Perturbative resummed series for top quark production in hadron reactions. *Phys.Rev.*, D54:3085–3113, 1996.

[33] Edmond L. Berger and Harry Contopanagos. Threshold resummation of the total cross-section for heavy quark production in hadronic collisions. *Phys.Rev.*, D57:253–264, 1998.

[34] J. Beringer et al. Review of particle physics. *Phys.Rev.*, D86:010001, 2012.

[35] W. Bernreuther, A. Brandenburg, Z.G. Si, and P. Uwer. Top quark spin correlations at hadron colliders: Predictions at next-to-leading order QCD. *Phys.Rev.Lett.*, 87:242002, 2001.

[36] W. Bernreuther, A. Brandenburg, Z.G. Si, and P. Uwer. Top quark pair production and decay at hadron colliders. *Nucl.Phys.*, B690:81–137, 2004.

[37] Werner Bernreuther, Michael Fuecker, and Zong-Guo Si. Weak interaction corrections to hadronic top quark pair production. *Phys.Rev.*, D74:113005, 2006.

[38] Ikaros I.Y. Bigi, Mikhail A. Shifman, and N. Uraltsev. Aspects of heavy quark theory. *Ann.Rev.Nucl.Part.Sci.*, 47:591–661, 1997.

[39] Ikaros I.Y. Bigi, Mikhail A. Shifman, N.G. Uraltsev, and A.I. Vainshtein. The Pole mass of the heavy quark. Perturbation theory and beyond. *Phys.Rev.*, D50:2234–2246, 1994.

[40] Roberto Bonciani, Stefano Catani, Michelangelo L. Mangano, and Paolo Nason. NLL resummation of the heavy quark hadroproduction cross-section. *Nucl.Phys.*, B529:424–450, 1998.

[41] A. Brandenburg, P.N. Burrows, D. Muller, N. Oishi, and P. Uwer. Measurement of the running b quark mass using $e^+e^- \to b\bar{b}$ events. *Phys.Lett.*, B468:168–177, 1999.

[42] David J. Broadhurst, N. Gray, and K. Schilcher. Gauge invariant on-shell Z(2) in QED, QCD and the effective field theory of a static quark. *Z.Phys.*, C52:111–122, 1991.

[43] Christopher Brust, Andrey Katz, Scott Lawrence, and Raman Sundrum. SUSY, the Third Generation and the LHC. *JHEP*, 1203:103, 2012.

[44] Andy Buckley, Jonathan Butterworth, Stefan Gieseke, David Grellscheid, Stefan Höche, et al. General-purpose event generators for LHC physics. *Phys.Rept.*, 504:145–233, 2011.

[45] B Butler and A Schwartzman. Track-jet reconstruction and performance. Technical Report ATL-PHYS-INT-2010-040, CERN, Geneva, Apr 2010. Internal document.

[46] J Butterworth, E Dobson, U Klein, B Mellado Garcia, T Nunnemann, J Qian, D Rebuzzi, and R Tanaka. Single boson and diboson production cross sections in pp collisions at $\sqrt{s} = 7$ TeV. Technical Report ATL-COM-PHYS-2010-695, CERN, Geneva, Aug 2010. Internal document.

[47] J.M. Butterworth, Jeffrey R. Forshaw, and M.H. Seymour. Multiparton interactions in photoproduction at HERA. *Z.Phys.*, C72:637–646, 1996.

[48] M. Cacciari, S. Frixione, M.L. Mangano, P. Nason, and G. Ridolfi. The $t\bar{t}$ cross-section at 1.8 TeV and 1.96 TeV: A Study of the systematics due to parton densities and scale dependence. *JHEP*, 0404:068, 2004.

[49] Matteo Cacciari, Michal Czakon, Michelangelo L. Mangano, Alexander Mitov, and Paolo Nason. Top-pair production at hadron colliders with next-to-next-to-leading logarithmic soft-gluon resummation. *Phys.Lett.*, B710:612–622, 2012.

[50] Matteo Cacciari, Stefano Frixione, Michelangelo L. Mangano, Paolo Nason, and Giovanni Ridolfi. Updated predictions for the total production cross sections of top and of heavier quark pairs at the Tevatron and at the LHC. *JHEP*, 0809:127, 2008.

[51] Matteo Cacciari and Gavin P. Salam. Dispelling the N^3 myth for the k_t jet-finder. *Phys.Lett.*, B641:57–61, 2006.

[52] Matteo Cacciari, Gavin P. Salam, and Gregory Soyez. The Anti-k(t) jet clustering algorithm. *JHEP*, 0804:063, 2008.

[53] Matteo Cacciari, Gavin P. Salam, and Gregory Soyez. FastJet user manual. *arXiv:1111.6097*, 2011.

[54] M Capeans, G Darbo, K Einsweiller, M Elsing, T Flick, M Garcia-Sciveres, C Gemme, H Pernegger, O Rohne, and R Vuillermet. ATLAS insertable B-layer technical design report. Technical Report CERN-LHCC-2010-013. ATLAS-TDR-019, CERN, Geneva, Sep 2010.

[55] S. Catani and L. Trentadue. Resummation of the QCD Perturbative Series for Hard Processes. *Nucl.Phys.*, B327:323, 1989.

[56] S. Catani and L. Trentadue. Comment on QCD exponentiation at large x. *Nucl.Phys.*, B353:183–186, 1991.

[57] Stefano Catani, Michelangelo L. Mangano, Paolo Nason, and Luca Trentadue. The Resummation of soft gluons in hadronic collisions. *Nucl.Phys.*, B478:273–310, 1996.

[58] Stefano Catani, Michelangelo L. Mangano, Paolo Nason, and Luca Trentadue. The Top cross-section in hadronic collisions. *Phys.Lett.*, B378:329–336, 1996.

[59] CERN. `http://homepage.mac.com/fishbonelpc/CERN/public.web.cern.ch/Public/Content/Chapters/AskAnExpert/LHC-en.html`, 2011.

[60] CERN. *oai:cds.cern.ch:1341525. Chamonix 2011 Workshop on LHC Performance*, Geneva, 2011. CERN. Organiser: Steve Myers.

[61] L Cerrito, B Cooper, A J Poll, V Boisvert, T Fonseca, R Goncalo, and M Rose. Study of electron isolation in Z $\rightarrow$ *ee* and $t\bar{t}$ decays. Technical Report ATL-PHYS-INT-2009-113, CERN, Geneva, Dec 2009.

[62] K.G. Chetyrkin, Johann H. Kühn, and A. Kwiatkowski. QCD corrections to the e^+e^- cross-section and the Z boson decay rate: Concepts and results. *Phys.Rept.*, 277:189–281, 1996.

[63] K.G. Chetyrkin and M. Steinhauser. The Relation between the $\overline{MS}$ and the on-shell quark mass at order α_s^3. *Nucl.Phys.*, B573:617–651, 2000.

[64] V. Cindro, D. Dobos, I. Dolenc, H. Frais-Koelbl, et al. The ATLAS beam conditions monitor. *JINST*, 3:P02004, 2008.

[65] The ATLAS Collaboration. First tuning of HERWIG/JIMMY to ATLAS data. Technical Report ATL-PHYS-PUB-2010-014, CERN, Geneva, Oct 2010.

[66] The ATLAS Collaboration. Close-by jet effects on jet energy scale calibration in pp collisions at $\sqrt{s} = 7$ TeV with the ATLAS detector. Technical Report ATLAS-CONF-2011-062, CERN, Geneva, Apr 2011.

[67] The ATLAS Collaboration. In-situ jet energy scale and jet shape corrections for multiple interactions in the first ATLAS data at the LHC. Technical Report ATLAS-CONF-2011-030, CERN, Geneva, Mar 2011.

[68] The ATLAS Collaboration. Jet energy scale and its systematic uncertainty in proton-proton collisions at $\sqrt{s} = 7$ TeV in ATLAS 2010 data. Technical Report ATLAS-CONF-2011-032, CERN, Geneva, Mar 2011.

[69] The ATLAS Collaboration. Light-quark and gluon jets in ATLAS. Technical Report ATLAS-CONF-2011-053, CERN, Geneva, Apr 2011.

[70] The ATLAS Collaboration. Luminosity determination in pp collisions at $\sqrt{s} =$ 7 TeV using the ATLAS detector in 2011. Technical Report ATLAS-CONF-2011-116, CERN, Geneva, Aug 2011.

[71] The ATLAS Collaboration. Measurement of the $t\bar{t}$ production cross-section in pp collisions at $\sqrt{s} = 7$ TeV using kinematic information of lepton+jets events. Technical Report ATLAS-CONF-2011-121, CERN, Geneva, Aug 2011.

[72] The ATLAS Collaboration. Muon momentum resolution in first pass reconstruction of pp collision data recorded by ATLAS in 2010. Technical Report ATLAS-CONF-2011-046, CERN, Geneva, Mar 2011.

[73] The ATLAS Collaboration. Reconstruction and calibration of missing transverse energy and performance in Z and W events in ATLAS proton-proton collisions at 7 TeV. Technical Report ATLAS-CONF-2011-080, CERN, Geneva, Jun 2011.

[74] The CMS collaboration. Determination of the top quark mass from the ttbar cross section at $\sqrt{s} = 7$ TeV. *CMS-PAS-TOP-11-008*, 2011.

[75] G. Corcella, I.G. Knowles, G. Marchesini, S. Moretti, K. Odagiri, et al. HERWIG 6: An Event generator for hadron emission reactions with interfering gluons (including supersymmetric processes). *JHEP*, 0101:010, 2001.

[76] Glen Cowan, Kyle Cranmer, Eilam Gross, and Ofer Vitells. Asymptotic formulae for likelihood-based tests of new physics. *Eur.Phys.J.*, C71:1554, 2011.

[77] Michal Czakon and Alexander Mitov. Top++: a program for the calculation of the top-pair cross-section at hadron colliders. *arXiv:1112.5675*, 2011.

[78] Michal Czakon and Alexander Mitov. NNLO corrections to top-pair production at hadron colliders: the all-fermionic scattering channels. *arXiv1207.0236*, 2012.

[79] F Deliot, V Ferrara, A Henrichs, U Husemann, M Keil, C Lange, A Roe, E Shabalina, and H Zhu. Determination of the top-quark mass from the ttbar cross section measurement in pp collisions at $\sqrt{s} = 7$ TeV with the ATLAS detector. Technical Report ATLAS-COM-CONF-2011-054, CERN, Geneva, Mar 2011.

[80] Ansgar Denner and Thomas Sack. The Top width. *Nucl.Phys.*, B358:46–58, 1991.

[81] Abdelhak Djouadi, Gregory Moreau, and Ritesh K. Singh. Kaluza-Klein excitations of gauge bosons at the LHC. *Nucl.Phys.*, B797:1–26, 2008.

[82] S.D. Ellis, R. Kleiss, and W. James Stirling. W's, Z's and Jets. *Phys.Lett.*, B154:435, 1985.

[83] F. Englert and R. Brout. Broken Symmetry and the Mass of Gauge Vector Mesons. *Phys.Rev.Lett.*, 13:321–323, 1964.

[84] Lyndon Evans and Philip Bryant. LHC Machine. *JINST*, 3:S08001, 2008.

[85] LEP EWWG. Precision Electroweak Measurements and Constraints on the Standard Model. *arXiv:1012.2367*, 2010.

[86] Adam F. Falk. The Heavy quark expansion of QCD. *ArXiv:9610363*, 1996.

[87] Valentina Ferrara et al. Lepton trigger and identification for the winter 2011 top quark analyses. Technical Report ATL-COM-PHYS-2011-123, CERN, Geneva, Feb 2011. Supporting document for Winter 2011 top physics measurements. Internal document.

[88] A.Liam Fitzpatrick, Jared Kaplan, Lisa Randall, and Lian-Tao Wang. Searching for the Kaluza-Klein Graviton in Bulk RS Models. *JHEP*, 0709:013, 2007.

[89] J. Fleischer, F. Jegerlehner, O.V. Tarasov, and O.L. Veretin. Two loop QCD corrections of the massive fermion propagator. *Nucl.Phys.*, B539:671–690, 1999.

[90] Sean Fleming, Andre H. Hoang, Sonny Mantry, and Iain W. Stewart. Jets from massive unstable particles: Top-mass determination. *Phys.Rev.*, D77:074010, 2008.

[91] Stefano Frixione, Paolo Nason, and Carlo Oleari. Matching NLO QCD computations with Parton Shower simulations: the POWHEG method. *JHEP*, 0711:070, 2007.

[92] Stefano Frixione and Bryan R. Webber. The MC@NLO event generator. *arXiv:0207182*, 2002.

[93] Paolo Gambino and Nikolai Uraltsev. Moments of semileptonic B decay distributions in the 1/m(b) expansion. *Eur.Phys.J.*, C34:181–189, 2004.

[94] Murray Gell-Mann. The Eightfold Way: A Theory of strong interaction symmetry. *CTSL-20, TID-12608*, 1961.

[95] Murray Gell-Mann. A Schematic Model of Baryons and Mesons. *Phys.Lett.*, 8:214–215, 1964.

[96] S.L. Glashow. Partial Symmetries of Weak Interactions. *Nucl.Phys.*, 22:579–588, 1961.

[97] N. Gray, David J. Broadhurst, W. Grafe, and K. Schilcher. Three loop relation of quark (modified) MS and pole masses. *Z.Phys.*, C48:673–680, 1990.

[98] D.J. Gross and Frank Wilczek. Ultraviolet Behavior of Nonabelian Gauge Theories. *Phys.Rev.Lett.*, 30:1343–1346, 1973.

[99] G.S. Guralnik, C.R. Hagen, and T.W.B. Kibble. Global Conservation Laws and Massless Particles. *Phys.Rev.Lett.*, 13:585–587, 1964.

[100] S.W. Herb et al. Observation of a Dimuon Resonance at 9.5-GeV in 400-GeV Proton-Nucleus Collisions. *Phys.Rev.Lett.*, 39:252–255, 1977.

[101] Peter W. Higgs. Broken Symmetries and the Masses of Gauge Bosons. *Phys.Rev.Lett.*, 13:508–509, 1964.

[102] Christopher T. Hill. Topcolor: Top quark condensation in a gauge extension of the standard model. *Phys.Lett.*, B266:419–424, 1991.

[103] Andre H. Hoang. Top threshold physics. *PoS*, TOP2006:032, 2006.

[104] Andre H. Hoang, Zoltan Ligeti, and Aneesh V. Manohar. B decay and the Upsilon mass. *Phys.Rev.Lett.*, 82:277–280, 1999.

[105] Andre H. Hoang, Zoltan Ligeti, and Aneesh V. Manohar. B decays in the upsilon expansion. *Phys.Rev.*, D59:074017, 1999.

[106] Andreas Hoecker, Peter Speckmayer, Joerg Stelzer, Jan Therhaag, Eckhard von Toerne, and Helge Voss. TMVA: Toolkit for Multivariate Data Analysis. *PoS*, ACAT:040, 2007.

[107] F. James and M. Roos. Minuit: A System for Function Minimization and Analysis of the Parameter Errors and Correlations. *Comput.Phys.Commun.*, 10:343–367, 1975.

[108] Peter Jenni, Marzio Nessi, Markus Nordberg, and Kenway Smith. ATLAS *high-level trigger, data-acquisition and controls: Technical Design Report*. Technical Design Report ATLAS. CERN, Geneva, 2003.

[109] M. Jezabek and Johann H. Kühn. QCD Corrections to Semileptonic Decays of Heavy Quarks. *Nucl.Phys.*, B314:1, 1989.

[110] William Casey Johnson. Search for Pair Production of Supersymmetric Top Quarks in Dilepton Events at the Tevatron. *FERMILAB-THESIS-2010-16*, 2010.

[111] Borut Paul Kersevan and Elzbieta Richter-Was. The Monte Carlo event generator AcerMC version 2.0 with interfaces to PYTHIA 6.2 and HERWIG 6.5. *arXiv:0405247*, 2004.

[112] Nikolaos Kidonakis. Single top production at the Tevatron: Threshold resummation and finite-order soft gluon corrections. *Phys.Rev.*, D74:114012, 2006.

[113] Nikolaos Kidonakis. NNLL resummation for s-channel single top quark production. *Phys.Rev.*, D81:054028, 2010.

[114] Nikolaos Kidonakis. Two-loop soft anomalous dimensions for single top quark associated production with a W- or H-. *Phys.Rev.*, D82:054018, 2010.

[115] Nikolaos Kidonakis. Next-to-next-to-leading-order collinear and soft gluon corrections for t-channel single top quark production. *Phys.Rev.*, D83:091503, 2011.

[116] Nikolaos Kidonakis, Eric Laenen, Sven Moch, and Ramona Vogt. Sudakov resummation and finite order expansions of heavy quark hadroproduction cross-sections. *Phys.Rev.*, D64:114001, 2001.

[117] Nikolaos Kidonakis and George F. Sterman. Resummation for QCD hard scattering. *Nucl.Phys.*, B505:321–348, 1997.

[118] Nikolaos Kidonakis and Ramona Vogt. Next-to-next-to-leading order soft gluon corrections in top quark hadroproduction. *Phys.Rev.*, D68:114014, 2003.

[119] Nikolaos Kidonakis and Ramona Vogt. The Theoretical top quark cross section at the Tevatron and the LHC. *Phys.Rev.*, D78:074005, 2008.

[120] Makoto Kobayashi and Toshihide Maskawa. CP Violation in the Renormalizable Theory of Weak Interaction. *Prog.Theor.Phys.*, 49:652–657, 1973.

[121] Chun-Hay Kom and W. James Stirling. Charge asymmetry in W + jets production at the LHC. *Eur.Phys.J.*, C69:67–73, 2010.

[122] Johann H. Kühn, A. Scharf, and P. Uwer. Electroweak effects in top-quark pair production at hadron colliders. *Eur.Phys.J.*, C51:37–53, 2007.

[123] Eric Laenen, J. Smith, and W.L. van Neerven. All order resummation of soft gluon contributions to heavy quark production in hadron hadron collisions. *Nucl.Phys.*, B369:543–599, 1992.

[124] Eric Laenen, J. Smith, and W.L. van Neerven. Top quark production cross-section. *Phys.Lett.*, B321:254–258, 1994.

[125] Hung-Liang Lai, Joey Huston, Zhao Li, Pavel Nadolsky, Jon Pumplin, et al. Uncertainty induced by QCD coupling in the CTEQ global analysis of parton distributions. *Phys.Rev.*, D82:054021, 2010.

[126] W. Lampl et al. Calorimeter clustering algorithms: Description and performance. Technical Report ATL-LARG-PUB-2008-002. ATL-COM-LARG-2008-003, CERN, Geneva, Apr 2008.

[127] Mark Lancaster. Combination of CDF and D0 results on the mass of the top quark using up to 5.8 fb-1 of data. *arXiv:1107.5255*, 2011.

[128] U. Langenfeld, S. Moch, and P. Uwer. Measuring the running top-quark mass. *Phys.Rev.*, D80:054009, 2009.

[129] B.E. Lautrup. On High Order Estimates in QED. *Phys.Lett.*, B69:109–111, 1977.

[130] Ben Lillie, Jing Shu, and Timothy M.P. Tait. Kaluza-Klein Gluons as a Diagnostic of Warped Models. *Phys.Rev.*, D76:115016, 2007.

[131] Michelangelo L. Mangano, Mauro Moretti, Fulvio Piccinini, Roberto Pittau, and Antonio D. Polosa. ALPGEN, a generator for hard multiparton processes in hadronic collisions. *JHEP*, 0307:001, 2003.

[132] A.D. Martin et al. Parton distributions for the LHC. *Eur. Phys. J.*, C63:189–285, 2009.

[133] A.D. Martin, W.J. Stirling, R.S. Thorne, and G. Watt. Uncertainties on alpha(S) in global PDF analyses and implications for predicted hadronic cross sections. *Eur.Phys.J.*, C64:653–680, 2009.

[134] C.D. McMullen and S. Nandi. Collider implications of Kaluza-Klein excitations of the electroweak gauge bosons. *arXiv:0110275*, 2001.

[135] Kirill Melnikov and Timo van Ritbergen. The Three loop relation between the $\overline{MS}$ and the pole quark masses. *Phys.Lett.*, B482:99–108, 2000.

[136] Sven Moch and Peter Uwer. Theoretical status and prospects for top-quark pair production at hadron colliders. *Phys.Rev.*, D78:034003, 2008.

[137] Alfred H. Mueller. On the Structure of Infrared Renormalons in Physical Processes at High-Energies. *Nucl.Phys.*, B250:327, 1985.

[138] Pavel M. Nadolsky, Hung-Liang Lai, Qing-Hong Cao, Joey Huston, Jon Pumplin, et al. Implications of CTEQ global analysis for collider observables. *Phys.Rev.*, D78:013004, 2008.

[139] K Nakamura and others (Particle Data Group). Review of particle physics, 2010-2011. review of particle properties. *J. Phys. G*, 37(7A):075021, 2010.

[140] P. Nason, S. Dawson, and R.Keith Ellis. The Total Cross-Section for the Production of Heavy Quarks in Hadronic Collisions. *Nucl.Phys.*, B303:607, 1988.

[141] Yuval Ne'eman. Derivation of strong interactions from a gauge invariance. *Nucl.Phys.*, 26:222–229, 1961.

[142] V.A. Novikov, L.B. Okun, M.A. Shifman, A.I. Vainshtein, M.B. Voloshin, et al. Charmonium and Gluons: Basic Experimental Facts and Theoretical Introduction. *Phys.Rept.*, 41:1–133, 1978.

[143] G. Parisi. Singularities of the Borel Transform in Renormalizable Theories. *Phys.Lett.*, B76:65–66, 1978.

[144] M. Perl et al. Evidence for Anomalous Lepton Production in e^+e^- Annihilation. *Phys.Rev.Lett.*, 35:1489–1492, 1975.

[145] H. David Politzer. Reliable Perturbative Results for Strong Interactions? *Phys.Rev.Lett.*, 30:1346–1349, 1973.

[146] German Rodrigo, Arcadi Santamaria, and Mikhail S. Bilenky. Do the quark masses run? Extracting $\overline{m}(b)$ (m(Z)) from LEP data. *Phys.Rev.Lett.*, 79:193–196, 1997.

[147] G Romeo, A Schwartzman, R Piegaia, T Carli, and R Teuscher. Jet energy resolution from in-situ techniques with the ATLAS detector using proton-proton collisions at a center of mass energy $\sqrt{s} = 7$ TeV. Technical Report ATL-COM-PHYS-2011-240, CERN, Geneva, Mar 2011. Internal document.

[148] ROOT. `http://root.cern.ch/root/html528/TH1.html`.

[149] Abdus Salam and John Clive Ward. Electromagnetic and weak interactions. *Phys.Lett.*, 13:168–171, 1964.

[150] Barbara Schmidt and Matthias Steinhauser. CRunDec: a C++ package for running and decoupling of the strong coupling and quark masses. *Comput.Phys.Commun.*, 183:1845–1848, 2012.

[151] Torbjörn Sjöstrand, Stephen Mrenna, and Peter Z. Skands. PYTHIA 6.4 Physics and Manual. *JHEP*, 0605:026, 2006.

[152] Peter Zeiler Skands. Tuning Monte Carlo Generators: The Perugia Tunes. *Phys.Rev.*, D82:074018, 2010.

[153] George F. Sterman. Summation of Large Corrections to Short Distance Hadronic Cross-Sections. *Nucl.Phys.*, B281:310, 1987.

[154] Gerard 't Hooft. Dimensional regularization and the renormalization group. *Nucl.Phys.*, B61:455–468, 1973.

[155] Gerard 't Hooft and M.J.G. Veltman. Regularization and Renormalization of Gauge Fields. *Nucl.Phys.*, B44:189–213, 1972.

[156] R. Tarrach. The Pole Mass in Perturbative QCD. *Nucl.Phys.*, B183:384, 1981.

[157] The ATLAS Collaboration. `https://twiki.cern.ch/twiki/bin/viewauth/AtlasProtected/WplusJetsBackgroundsforTopAnalyses`, 2011.

[158] The ATLAS Collaboration. Combined search for the standard model Higgs boson using up to 4.9 fb^{-1} of pp collision data at $\sqrt{s} = 7$ TeV with the ATLAS detector at the LHC. oai:cds.cern.ch:1421964. *Phys. Lett. B*, 710(arXiv:1202.1408. CERN-PH-EP-2012-019):49–66. 22 p, Feb 2012.

[159] The CMS Collaboration. Combined results of searches for the standard model higgs boson in pp collisions at $\sqrt{s} = 7\ mathrmTeV$. *oai:cds.cern.ch:1422614*, Feb 2012.

[160] S van der Meer. Calibration of the effective beam height in the isr. oai:cds.cern.ch:296752. Technical Report CERN-ISR-PO-68-31. ISR-PO-68-31, CERN, Geneva, 1968.

[161] Wouter Verkerke. Guide to parameterized likelihood analyses. *Unpublished*, 2012.

[162] Steven Weinberg. A Model of Leptons. *Phys.Rev.Lett.*, 19:1264–1266, 1967.

[163] J. Wess and B. Zumino. A Lagrangian Model Invariant Under Supergauge Transformations. *Phys.Lett.*, B49:52, 1974.

[164] R. Wigmans. Calorimetry: Energy measurement in particle physics. *Int.Ser.Monogr.Phys.*, 107:1–726, 2000.

[165] G Zweig. An SU_3 model for strong interaction symmetry and its breaking. *CERN-TH-412, oai:cds.cern.ch:570209; Part II*, page 80 p, Feb 1964.

List of Figures

List of Tables

Selbständigkeitserklärung

Ich erkläre, dass ich die vorliegende Arbeit selbständig und nur unter Verwendung der angegebenen Literatur und Hilfsmittel angefertigt habe.

Berlin, den 6.8.2012 Valentina Ferrara